NOVA SCHOOL OF SCIENCE & TECHNOLOGY

DEPARTMENT OF PHYSICS

MATILDE MARQUES AMARO

BSc in Biomedical Engineering

SURFACE FUNCTIONALIZATION OF ADDITIVELY MANUFACTURED MG-BASED MEDICAL IMPLANTS

MASTER IN BIOMEDICAL ENGINEERING

NOVA University Lisbon
September, 2024

NOVA SCHOOL OF SCIENCE & TECHNOLOGY

DEPARTMENT OF PHYSICS

SURFACE FUNCTIONALIZATION OF ADDITIVELY MANUFACTURED MG-BASED MEDICAL IMPLANTS

MATILDE MARQUES AMARO

BSc in Biomedical Engineering

Adviser: João Pedro de Sousa Oliveira
Full Professor, NOVA University Lisbon

Co-adviser: Ana Catarina Bernardino Baptista
Assistant Professor, NOVA University Lisbon

Examination Committee

Chair: Célia Maria Reis Henriques
Associate Professor, NOVA University Lisbon

Rapporteur: Catarina Ferreira dos Santos
Coordinating Professor, ESTSetúbal/IPS

Adviser: João Pedro de Sousa Oliveira
Full Professor, NOVA University Lisbon

MASTER IN BIOMEDICAL ENGINEERING

NOVA University Lisbon
September, 2024

Surface Functionalization of Additively Manufactured Mg-based Medical Implants

This document was created with the (pdf/Xe/Lua)LaTeX processor and the NOVAthesis template (v7.1.27) [1].

Para a minha mãe, que me deu as suas próprias asas para
que eu pudessse voar mais alto.

Acknowledgements

I would like to begin by expressing my deepest gratitude to my supervisors, Professor João Pedro Oliveira and Professor Ana Baptista, for their trust and for giving me the opportunity to undertake this research. Their constant support, accessibility, and insightful guidance throughout the duration of this project have made this challenging journey both enlightening and rewarding.

I am also deeply grateful to the researchers in the laboratory who provided invaluable assistance throughout the process, particularly Luís Almeida, Jiajia Shen, and Davi Marques. Your guidance, expertise, and support were instrumental at various stages of this work, and I am fortunate to have had the opportunity to learn from and collaborate with such knowledgeable and dedicated individuals. I would also like to express my appreciation to Tânia Vieira for her invaluable assistance in performing the cytotoxicity assays, which were crucial to the success of this work.

Moreover, I wish to extend my gratitude to all the professors and staff at this institution who have played an important role in my academic growth. Your dedication and support have been pivotal to my development, and I am sincerely grateful for your guidance.

A special mention goes to my lab partners, Rafael, Sofia, and Tiago. The long, challenging hours spent in the lab were made enjoyable thanks to the moments of joy and laughter we shared.

To my coursemates turned lifelong friends — Ana, Alexandra, Caetano, Catarina, Emanuel, Jéssica, Marcella and Matilde — thank you for being my constant pillars of support over the past five years. From late-night study sessions and last-minute revisions to simply being there during life's ups and downs, you made this journey infinitely more fulfilling. I couldn't have done it without you.

I owe an immense debt of gratitude to my family. To my mum, thank you for always pushing me to aim higher and for being my greatest source of motivation. To my sister, who somehow manages to either make me laugh until I cry or annoy me beyond words, thank you. To my grandmother, uncles, aunts, and cousins, your support during this time was invaluable.

To all of you, a heartfelt thank you.

Abstract

To eliminate the need for additional surgery to remove short-term metal implants, bioresorbable materials like magnesium (Mg) are being explored due to their inherent ability to gradually degrade *in vivo*. However, Mg's rapid corrosion has limited its practical use. Surface coatings, such as hydroxyapatite (HA), are often applied to slow degradation and promote bone regeneration. Despite these benefits, such coatings can diminish Mg's intrinsic antibacterial properties.

This study aimed to develop a dual-coating system that balances corrosion resistance and antibacterial properties by combining HA with antibacterial agents, specifically titanium dioxide (TiO_2) and silver (Ag). Mg alloy AZ61 samples were produced via wire arc additive manufacturing (WAAM) and functionalized through electrochemical deposition. Initial tests optimized the base HA coating and the best protocol was selected. The double coatings were subsequently studied, with the HA base coating remaining consistent. Optimal conditions for the second layer were identified as 1 V for 45 minutes for TiO_2 and a low-concentration electrolyte for 30 minutes for Ag.

Electrochemical tests demonstrated that the composite coatings significantly enhanced the corrosion resistance, particularly in neutral environments. The corrosion current density (I_{corr}) of uncoated Mg, initially 139.541 $\mu A/cm^2$, was reduced by 99.83% to just 0.238 $\mu A/cm^2$ with the HA-TiO_2 coating, while the HA-Ag coating achieved a reduction of 99.71%, bringing the I_{corr} down to 0.404 $\mu A/cm^2$. Additionally, cytotoxicity tests revealed that cell viability remained high (over 90%) for most coatings across all tested concentrations, with the exception of certain Ag-containing samples, which exhibited a viability drop in higher concentrations. These findings suggest that these combined coatings could be a promising strategy for developing bioresorbable implants with improved properties.

Keywords: Bioresorbable implants, Magnesium, Corrosion resistance, Hydroxyapatite coating, Antibacterial coatings, Wire and Arc Additive Manufacturing

Resumo

Para eliminar a necessidade de uma cirurgia adicional para remover implantes metálicos de curta duração, materiais bioabsorvíveis, como o magnésio (Mg), estão a ser explorados pela sua capacidade de se degradar gradualmente *in vivo*. No entanto, a rápida corrosão do Mg limita o seu uso prático. Revestimentos de superfície, como a hidroxiapatite (HA), são aplicados para retardar a degradação e promover a regeneração óssea, no entanto diminuem as propriedades antibacterianas do Mg.

Este estudo visou desenvolver um revestimento duplo que equilibre resistência à corrosão e propriedades antibacterianas, combinando a HA com agentes antibacterianos, especificamente o dióxido de titânio (TiO_2) e a prata (Ag). Amostras da liga de Mg AZ61 foram produzidas por fabrico aditivo por fio e arco (WAAM), e a sua superfície foi funcionalizada através de deposição eletroquímica. Testes iniciais otimizaram o revestimento base de HA, selecionando o melhor protocolo. Os revestimentos duplos foram depois estudados, mantendo o mesmo revestimento base de HA. As condições para a segunda camada ideal foram 1 V durante 45 minutos para o TiO_2 e uma solução eletrolítica de baixa concentração durante 30 minutos para a Ag.

Os ensaios eletroquímicos demonstraram que os revestimentos duplos aumentaram a resistência à corrosão, especialmente em meio neutro. A densidade de corrente de corrosão (I_{corr}) do Mg, inicialmente 139,541 $\mu A/cm^2$, foi reduzida em 99,83% para 0,238 $\mu A/cm^2$ com o revestimento HA-TiO_2, já a dupla camada HA-Ag obteve uma redução de 99,71%, com I_{corr} de 0,404 $\mu A/cm^2$. Os ensaios de citotoxicidade mostraram viabilidade acima de 90% para a maioria dos revestimentos, exceto algumas amostras com Ag, que apresentaram uma redução significativa em concentrações mais elevadas. Estes resultados sugerem que estes revestimentos combinados são uma estratégia promissora para implantes bioabsorvíveis com propriedades melhoradas.

Palavras-chave: Implantes bioabsorvíveis, Magnésio, Resistência à corrosão, Revestimento com hidroxiapatite, Revestimentos antibacterianos, Fabrico Aditivo por Fio e Arco

Contents

List of Figures

List of Tables

Abbreviations

β-TCP	β-Tricalcium Phosphate
|Z|	Impedance Modulus
AM	Additive Manufacturing
CMT	Cold Metal Transfer
CR	Corrosion Rate
DCPD	Dicalcium Phosphate Dehydrate
DED	Direct Energy Deposition
E_{corr}	Corrosion Potential
EDS	Energy Dispersive Spectroscopy
EIS	Electrochemical Impedance Spectroscopy
FTIR	Fourier Transform Infrared Spectroscopy
GMAW	Gas Metal Arc Welding
HA	Hydroxyapatite
I_{corr}	Corrosion Current Density
ML	Mass Loss
OCP	Open Circuit Potential
PBS	Phosphate Buffered Saline
PR	Polarisation Resistance Test

R_p Polarisation Resistance
ROS Reactive Oxygen Species

SBF Simulated Body Fluid
SEM Scanning Electron Microscopy

TiO_2 Titanium Dioxide

WAAM Wire Arc Additive Manufacturing

XRD X-ray Diffraction

1 Introduction

This chapter is divided into three sections. The first provides an overview of the context and motivation for this dissertation. The following section sets out the objectives that were sought to be achieved. Finally, the document structure is explained.

1.1 Context and Motivation

Bone fractures are a universal health concern, in 2019 alone, there were 178 million new fractures, up 33.4% from 1990 [2]. These can result in disability and a poor quality of life, in addition to causing a significant financial burden on both individuals and medical services. While most fractures are often treated with immobilization using casts, orthopaedic surgery is necessary in cases where the healing process relies on implants like bone plates and screws to stabilize and rejoin the bone fragments.

Meanwhile, cardiovascular diseases are another pressing health issue, coronary heart disease, for example, affects approximately 200 million people globally [3]. When dealing with illnesses that arise from narrowed arteries due to plaque accumulation, a prevalent approach involves the implantation of stents that expand the narrowed space.

Traditionally, cobalt-chromium-molybdenum alloys, stainless steel, and commercially pure titanium and its alloys have been widely used for medical implants. These materials have the necessary qualities — superior mechanical performance, biocompatibility, and great resistance to corrosion — to ensure that the implant preserves its structural stability inside the body [4]. Nevertheless, since those materials are not bioresorbable once the healing process is complete, a subsequent procedure is required to remove the no longer needed implant. This second surgery has a detrimental effect on the patient's physical and psychological recovery, increases the risk of infection, and burdens the healthcare system as it demands more resources [5]. To avoid this additional procedure which only purpose is to remove the short-term application implant, the possibility of bioresorbable devices that gradually corrode *in vivo* until complete dissolution, while the bone and tissue regenerates, has been explored.

While many metals possess excellent mechanical qualities, most of them are toxic or

non-absorbable. However, this is not the case for Magnesium (Mg), with exceptional biocompatibility and natural biodegradation under physiological conditions, it emerges as a promising material for temporary metal implants [5]. But, the bioresorbable quality of Mg and its alloys is also their greatest drawback due to their rapid corrosion. Implants must withstand various mechanical actions of the human body, requiring them to have appropriate strength and wear resistance, and Mg quick deterioration at physiological pH results in inadequate mechanical properties before the bone and tissue have sufficiently healed [6].

While there are numerous strategies for enhancing the corrosion resistance of Mg alloys, surface coatings have gained significant attention due to their ability to not only control the degradation behaviour but also enhance other characteristics, such as antibacterial activity [5]. Of the numerous techniques available for developing surface coatings, electrodeposition is regarded as an accessible and reliable method that offers the potential for coating properties to be tailored to specific needs.

A prominent approach to control degradation rates involves coating Mg with Hydroxyapatite (HA). This material has been extensively studied and utilized in various biomedical applications due to its bioactive and biocompatible nature [7, 8]. However, Mg's inherent antibacterial properties are directly related to its rapid corrosion and infection is a significant risk associated with biomaterials, that leads to inflammation and material loosening, even surgery in extreme cases [9]. Efforts to improve the antibacterial properties of coated Mg have been made, and the antibacterial impact of metal ions such as Silver (Ag) and Titanium (Ti) are promising. Therefore, doping these elements into coatings could be a viable approach to enhance Mg's corrosion resistance and antibacterial properties [10, 11].

To maximize the efficiency of these coatings, it is essential to ensure that the Mg surface has the right characteristics for optimal adhesion and performance. One effective method that has been gaining recognition for preparing such substrates is Wire Arc Additive Manufacturing (WAAM). The exponential growth of the Additive Manufacturing (AM) industry has allowed for this production method to jump into the medical world. It facilitates the creation of complex components, a great advantage to consider when discussing implants [12]. So, the WAAM method was chosen for this project.

1.2 Dissertation Goals

To overcome the obstacles characteristic of the biodegradation of Mg implants, the following steps were taken:

- **Produce defect-free Mg metal parts** with WAAM, using optimised process parameters;
- **Coat the Mg substrate** with HA only and with HA and the antibacterial agent (Ag and Ti) using electrodeposition and optimise the coating protocols to achieve surface

protection, biocompatibility, bioactivity and antibacterial properties;

- **Characterise the coatings morphologically, structurally and chemically** using Scanning Electron Microscopy (SEM) with Energy Dispersive Spectroscopy (EDS), X-ray Diffraction (XRD) and Fourier Transform Infrared Spectroscopy (FTIR), respectively;
- **Electrochemical analysis** under simulated physiological conditions with Open Circuit Potential (OCP), Polarisation Resistance Test (PR) and Electrochemical Impedance Spectroscopy (EIS), to assess the corrosion resistance and degradation behaviour of the samples;
- ***In vitro* degradation tests** to assess the samples' degradation behaviour via immersion testing, focusing on how the coatings influence the degradation rate;
- **Cytotoxicity analysis** to evaluate the biocompatibility of the coated and uncoated Mg substrates to ensure they are safe for biomedical applications.

1.3 Document Structure

This document is structured into six chapters, which are outlined as follows:

- Chapter 1: **Introduction** - overview of the motivation and objectives of this dissertation;
- Chapter 2: **Summary of Theoretical Concepts** - key theoretical concepts that underline this research;
- Chapter 3: **State of the Art** - literature review on the dissertation topic, highlighting the gaps in it;
- Chapter 4: **Materials and Methods** - description of the materials used and the methodologies employed to accomplish each task;
- Chapter 5: **Results and Discussion** - presents the research findings, its analysis and discusses its relevance to the central problem;
- Chapter 6: **Conclusions and Future Work** - summary of the research conducted, highlighting its contributions, and suggested directions for future research.

The research work described in this dissertation was carried out in accordance with the norms established in the ethics code of Universidade Nova de Lisboa. The work described and the material presented in this dissertation, with the exceptions clearly indicated, constitute original work carried out by the author.

2

Summary of Theoretical concepts

This chapter provides an overview of the key theoretical concepts that underpin this research. It begins with WAAM, the manufacturing method used to produce the Mg samples, followed by a closer look at Mg itself. Next, the electrodeposition method, used to coat the samples, is briefly introduced. Finally, the materials used as coatings — HA and antibacterial agents (Titanium Dioxide (TiO_2) and Ag nanoparticles) — are explored.

2.1 Wire Arc Additive Manufacturing

In recent years, AM has attracted considerable research interest, particularly in the engineering world. As a result, there is growing interest in using the design capabilities of AM to push the boundaries of medical progress. Given the individuality of each patient, this technique holds great promise for the development of personalised medical applications [13]. Compared to conventional manufacturing processes, AM can produce large and complex geometries, with layer-by-layer deposition and a computer-aided design, that would otherwise be difficult or impossible to achieve. In addition, it uses material more efficiently, reduces post-processing costs and manufacturing time, and improves mechanical properties [13, 14].

Direct Energy Deposition (DED) is one of the four primary AM technologies used to produce metal parts [15]. DED systems fuse materials by melting them as they are deposited using focused thermal energy [16]. WAAM is one of the three main techniques used in this AM category. It is defined as the combination of an electric arc as the heat source and a wire as the feedstock [17]. A schematic diagram is shown in Figure 2.1. The advantages of WAAM over other DED processes include lower cost, more efficient use of materials and higher deposition rate [16]. The predominant arc welding process currently used in WAAM is Gas Metal Arc Welding (GMAW), a fusion-based arc welding technique in which an inert or active shielding gas, that simultaneously shields the surrounding material and the weld pool, creates an arc between the tip of a consumable wire and the workpiece [17]. Owing to its deposition rates, versatility, and ease of use, GMAW was chosen for this project.

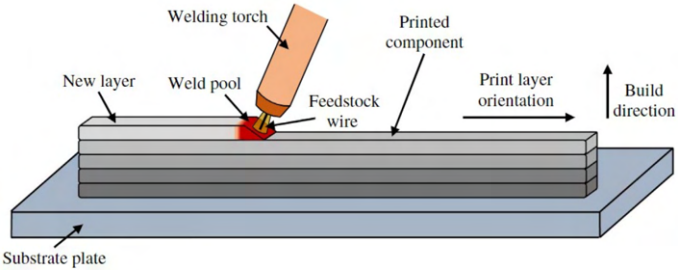

Figure 2.1: Schematic representation of the WAAM process [18].

2.2 Magnesium

Research into Mg and its alloys as biomaterials, particularly for short-term implants, is expanding. Mg is an alkaline earth metal with a hexagonal crystal structure. As the fourth most abundant cation, it is indispensable for cellular processes, functioning as a cofactor in over 300 enzymatic reactions. Such functions include the metabolism of ATP, the contraction and relaxation of muscles, and the maintenance of normal neurological function [19].

Mg is predominantly distributed in bone tissue, where it is known to support osteoinductivity, thereby promoting bone formation and healing [6]. Furthermore, in instances where its levels exceed the optimal range, the excess is excreted in the urine without any adverse effects [20]. Mg is therefore inherently biocompatible, non-toxic and non-irritating, and does not interfere with normal metabolic function.

While many metals possess excellent mechanical qualities, the majority are toxic or non-absorbable. Conventional surgical alloys produce corrosion products that are harmful to the human body [6]. In contrast, Mg exhibits superior biodegradability and bioabsorbability, coupled with remarkable mechanical properties that are well-suited to human bone. Being the lightest engineering metal due to its high strength-to-weight ratio, results in the creation of a lighter implant, which facilitates superior integration. The proximity of Mg's density (1.74 to 2.0 g/cm^3) to that of bone (1.8 to 2.1 g/cm^3) distinguishes it from other potential materials [5, 11].

Additionally, an implant that is excessively rigid can cause stress shielding, which disrupts the natural healing process and, in severe cases, may result in bone loss and fractures. Reducing the discrepancy in elastic modulus between the implant and the bone can help prevent stress shielding. Mg, with an elastic modulus of 40–45 GPa, exhibits a stiffness that is considerably closer to that of natural bone (3–20 GPa) than that of standard metallic materials, making it a more suitable option [5, 6].

Despite the significant advantages offered by Mg, rapid corrosion, particularly when the material is exposed to water solutions, represents a significant barrier to its wider development and exploitation. Mg corrosion in aqueous environments is an electrochemical phenomenon, the reaction with water produces magnesium hydroxide, $Mg(OH)_2$, and hydrogen gas, H_2, occurring in accordance with Equation 2.1 [21]. In this reaction,

a protective film, $Mg(OH)_2$, is produced, which has the effect of slowing down the deterioration process. However, the physiological environment is characterised by a high chloride concentration, which results in the dissolution of the film through a reaction with magnesium chloride ($MgCl_2$) in accordance with Equation 2.2 [21]. The soluble salt is no longer capable of providing protection from further corrosion.

$$Mg + 2H_2O \rightarrow Mg(OH)_2 + H_2 \tag{2.1}$$

$$Mg(OH)_2 + 2Cl^- \rightarrow MgCl_2 + 2OH^- \tag{2.2}$$

Mg rapid corrosion has several consequences, including the production of H_2. The formation of gas bubbles may result in the separation of tissues and tissue layers, leading to the necrosis of surrounding tissues [6]. The hasty breakdown also causes alkalization, whereby hydroxide ions produced in Equation 2.2 raise the pH level in the vicinity of the implant. Notwithstanding the body's attempts to counteract this phenomenon, the resulting increase in pH is inevitable and can potentially result in alkaline poisoning when the regional pH exceeds 7.8 [5]. The hasty deterioration of Mg represents a significant limitation that must be addressed.

2.3 Electrochemical Deposition

The electrochemical deposition technique, illustrated in Figure 2.2, was employed to coat the substrates with HA and the antibacterial agents — Ag and TiO_2. This technique is distinguished by its simplicity and cost-effectiveness, enabling the production of controlled and uniform coatings on various surfaces [22].

An electrochemical cell comprises two electrodes submerged in an electrolyte solution. These electrodes are designated as the counter-electrode, or anode, and the working electrode, or cathode, which is the intended electrodeposition target. The anode and the electrolyte solution, an aqueous medium containing ions from dissolved metal salts, are selected based on the material undergoing electroplating [22].

The introduction of an external voltage to the electrochemical cell initiates the passage of an electric current, which prompts the migration of charged species within the electrolyte towards the surfaces of the polarized electrodes. At the electrode surfaces, the reduction or oxidation of ionic species occurs. The reduction reactions that occur at the cathode are responsible for the formation of a homogeneous coating on its surface [22, 23].

2.4 Hydroxyapatite

HA, a vital natural component of bones, is a calcium apatite with outstanding biocompatibility, bioactivity, and biodegradability, rendering it a valuable material in the biomedical field. The fundamental apatite structure formula is $Ca_{10}(PO_4)_6X_2$, where X denotes the specific apatite form, namely hydroxyl (OH) for HA [8]. The hexagonal structure of the

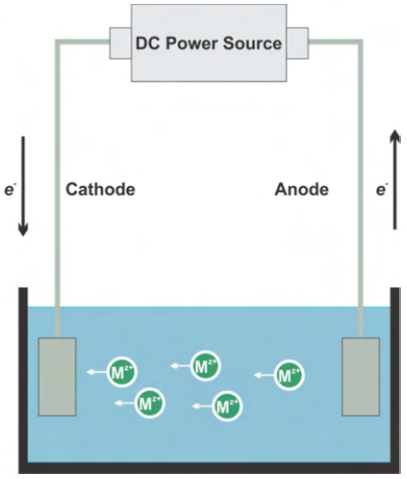

Figure 2.2: Schematic illustration of the electrodeposition process [23].

HA unit cell is illustrated in Figure 2.3. HA, which constitutes approximately 50% of bone by weight and has a Calcium (Ca)/Phosphorus (P) ratio equal to 1.67, imparts remarkable osteointegrative and osteoconductive properties [8]. These properties enable HA to stimulate the formation of new tissue without triggering local or systemic toxicity [24]. The chemical and structural similarity of HA to the mineral phase of bone enables it to form chemical bonds directly with its tissue, promoting bone proliferation and regeneration [7, 8]. The stability of calcium phosphates is contingent upon the presence of water. At body temperature, only two phases are stable in contact with body fluids. Of these, only HA is stable at a pH higher than 4.2 [24].

HA has a wide variety of uses in the biomedical industry, including as a coating material. An optimal implant must exhibit a balance between biocompatibility, corrosion resistance, and mechanical strength. By applying HA coatings, the mechanical properties of Mg can be combined with the biological ones of HA [25, 26]. The coating creates a protective barrier between the corrosive medium and the metal substrate, which mitigates degradation and enhances the biological activity of Mg alloys.

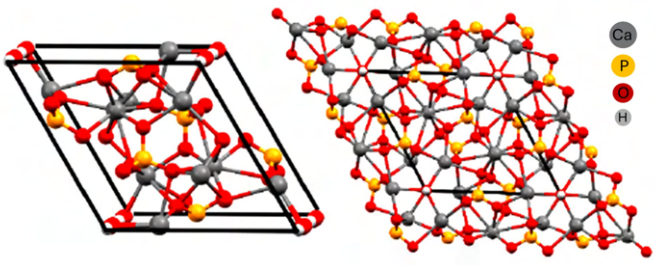

Figure 2.3: Crystalline structure of HA (left) and the projection of HA structure in plane 001 (right) [24].

2.5 Antibacterial Agents

Despite the historical success of antibiotics, their overuse has resulted in the emergence of drug-resistant strains of bacteria, which now poses a significant threat to the efficacy of existing treatments [27, 28]. The adaptive countermeasures employed by bacteria against antibiotics are evidenced by the alarming number of deaths attributed to infections caused by antibiotic-resistant bacteria [28].

A significant challenge arises with the formation of biofilms on the implants surface once integrated in the body. This marks the initial stages of bacterial colonization, which can eventually lead to bone infections [29]. The degradation of Mg is an interesting way to address biofilm-related concerns. As Mg corrodes, the alkalinity of the surrounding solution increases, raising the pH to a 9 - 10 range. However, most bacteria thrives within a pH range of 6 - 8. This elevated alkalinity emerges as a key factor in the observed antibacterial activity [9, 10]. Also, the degradation of Mg produces hydroxyl ions, OH^-, while the attached bacteria release H^+. The resulting neutralisation consumes H^+, disrupting the bacteria intermembrane space and impeding the synthesis of ATP, which ultimately leads to bacterial death [10]. Nevertheless, attempts to enhance the corrosion resistance of Mg, such as surface coatings, inevitably results in a compromise of its antibacterial capabilities.

The introduction of metallic nanoparticles into these coatings represents a promising approach to simultaneously improve antibacterial activity and corrosion resistance. Nanomaterials are a category of non-traditional biocide that possess distinctive physicochemical characteristics, including surface properties, dimensions (typically 100 nm or less), and structural configuration. Due to their comparable dimensions to biomolecules and bacteria, nanoparticles can be employed as an innovative prevention method [30].

Metal-based nanoparticles can be pure metals (such as Ag) or metal compounds (such as oxides) [30]. It has been proven that they are effective in combating a multitude of bacterial infections due to their high reactivity and ability to target a range of biological molecules. The primary toxicological mechanism of these nanoparticles is the impairment of the membrane function and the generation of Reactive Oxygen Species (ROS). The impact of these mechanisms is typically observed in the genetic material and proteins of the bacterial organisms [28, 30].

Combining HA and metallic nanoparticles on the surface of a medical implant may prove to be an effective method of controlling both corrosion and the risk of bacterial infection. In this study, the selected metallic nanoparticles were Ag and TiO_2.

2.5.1 Silver

The use of Ag in the context of wound healing has been revitalized due to its effectiveness in combating antibiotic-resistant bacteria. But, the importance of Ag nanoparticles size in surface coating cannot be overstated, as smaller nanoparticles have been proven to exhibit

higher toxicity [31]. The antibacterial effect of Ag results from the destruction of bacterial membranes through the formation of Ag^+ ions, which ultimately results in bacterial death. The mechanism involves the binding of Ag^+ ions to thiol groups in bacterial enzymes, that causes a rapid loss of enzyme activity. The release of Ag^+ ions can initiate a new antibacterial process, thereby contributing to long-lasting antibacterial properties. An alternative mechanism suggests the generation of ROS at the cell membrane, which can cause irreversible damage to the DNA replication process [11].

2.5.2 Titanium Dioxide

The potential antibacterial properties of TiO_2 have been the subject of considerable investigation, with the photocatalytic properties of the compound being identified as the primary mechanism responsible for its antimicrobial activity [32]. TiO_2 nanoparticles have demonstrated to be highly effective antimicrobial agents, due to their elevated surface area and augmented reactivity. They have the capacity to eradicate a diverse array of bacterial strains [32, 33].

When TiO_2 nanoparticles are exposed to UV light, they absorb the energy of the photons and enter an excited state, transferring an electron to an oxygen molecule, thereby forming an oxygen radical. The radical then reacts with water molecules to form hydroxyl radicals, which are highly reactive and can damage bacterial cells by breaking down the lipids that make up the membrane or by damaging the bacterial DNA, causing strand breaks and mutations [32, 34].

3

State of the Art

This chapter reviews current progress in Mg alloys, focusing on their production via WAAM, the application of HA coatings, and the incorporation of antibacterial agents in coatings.

3.1 Wire Arc Additive Manufacturing of Magnesium alloys

WAAM is an emerging technology that employs arc welding processes to construct components layer-by-layer. In recent years, it has attracted considerable interest in the field of Mg alloys manufacturing, due to the exceptional properties of these lightweight structural alloys. Guo *et al.* [35] pioneered the application of WAAM to the AZ31 Mg alloy, demonstrating that the pulse frequency has a significant influence on the macrostructure, microstructure, and tensile properties of the produced specimens.

Research focused on optimizing processing parameters to enhance structural and mechanical properties is ongoing. Takagi *et al.* [36] studied the use of Metal Inert Gas (MIG) welding in the WAAM of Mg alloys. They identified optimal parameters for producing solid, low-defect structures with minimal porosity: 100 A, 10 V, and 800 mm/min. Elevated torch feed rates were found to improve elongation and promote microstructural refinement. Ying *et al.* [37] achieved excellent microstructure and mechanical properties with slightly different parameters: 130 A, 12.5 kV, and 820 mm/min. Although the voltage was significantly higher, the torch feed rate aligned closely with the previous findings.

However, a 2019 study by Guo *et al.* [38] on the AZ80M alloy revealed microstructural inhomogeneity, which led to notable anisotropy in tensile strength. This highlighted the difficulty of achieving uniform mechanical properties in materials produced via WAAM. In 2021, the same research group explored post-deposition heat treatments, finding that a solution plus an artificial ageing process significantly improved strength and reduced anisotropy. This marked a critical advancement in WAAM technology [39].

Additionally, Cold Metal Transfer (CMT) has emerged as a promising technique within WAAM for Mg alloys. Klein *et al.* [40] demonstrated the potential of CMT-WAAM with the AZ61A alloy, achieving a homogeneous, fine-grained microstructure with minimal

hardness variation and low mechanical anisotropy. Similarly, Wang *et al.* [41] confirmed CMT's effectiveness to produce AZ31 alloys, although challenges such as heat-affected zone softening and porosity were identified. Yin *et al.* [42] further validated the feasibility of CMT-WAAM with AZ91 alloys, despite observing some tensile anisotropy at pass overlaps. These findings suggest that CMT-WAAM may offer a viable alternative to traditional casting and wrought processes for Mg alloys.

WAAM shows significant potential as a manufacturing technique to produce Mg alloys, offering versatility and efficiency compared to traditional methods. It has the potential to play a pivotal role in the large-scale production of Mg components. However, the use of this method for the fabrication of Mg alloy AZ61 is still in its early stages.

3.2 Hydroxyapatite Coatings on Magnesium

The rapid corrosion of Mg in physiological environments has limited its potential as a biodegradable material. To address this issue, researchers have focused on HA coatings, which can improve both the corrosion resistance and bioactivity of Mg-based implants.

Jamesh *et al.* [26] and Song *et al.* [43] were among the first to investigate the efficacy of HA coatings prepared by electrodeposition on commercially pure Mg and AZ91D Mg alloy surfaces, respectively. Initially identified as Dicalcium Phosphate Dehydrate (DCPD), these coatings transformed into HA upon immersion in an alkaline NaOH solution. The HA coatings demonstrated increased corrosion resistance and reduced biodegradation rates in Simulated Body Fluid (SBF), highlighting their potential for biomedical applications.

Building on these findings, Rahman *et al.* [44] produced a double-layer DCPD coating on the WE43 alloy, improving microhardness and adhesion. Subsequent alkaline treatment converted the DCPD layer into a compact, crack-free HA coating, resulting in the lowest hydrogen gas evolution and highest corrosion resistance observed in their study. Similarly, Rončević *et al.* [45] modified the AZ91D alloy surface with HA coatings via electrodeposition, which demonstrated superior corrosion resistance in Hanks' solution, further confirming the coating's protective capabilities.

In addition to demonstrating the effectiveness of HA coatings, several studies have evaluated the performance of different coating methods. Salman *et al.* [46] found that an HA coating applied at -1.4 V exhibited enhanced bioactivity and corrosion resistance, improving the *in vitro* performance of Mg alloys. Uddin *et al.* [47] investigated the effect of current density on HA coatings applied to an AZ31B Mg substrate and concluded that the best corrosion protection was achieved with a compact, dense, and homogeneous coating obtained at lower current densities.

These studies demonstrate the potential of HA coatings to improve the corrosion resistance and bioactivity of Mg alloys, paving the way for their use in biomedical implants.

3.3 Antibacterial Agents Coatings on Magnesium

In recent years, extensive research has focused on exploring the antibacterial properties of metal ions, such as TiO_2 and Ag, particularly when combined with HA.

Starting with composite HA-TiO_2 coatings, Amaravathy *et al.* [48] employed a sol-gel method and dip-coating process to develop HA and HA-TiO_2 coatings on Mg alloys, aiming to enhance biocompatibility and reduce corrosion rates. The HA-TiO_2-coated alloy demonstrated improved hydrophilicity, osteoinduction, corrosion resistance, mechanical strength, and cell attachment compared to the HA-coated alloy. Similarly, Guo *et al.* [49] developed a TiO_2 coating on HA-coated Mg alloys using the same method, with the goal of enhancing corrosion resistance and bioactivity for orthopaedic applications. The TiO_2 coating showed enhanced corrosion resistance, along with superior cell adhesion and growth, compared to both HA-coated and uncoated Mg alloys. Additionally, the composite coating exhibited strong antibacterial properties, with a 99.5% and 99.8% reduction in *E. coli* and *S. aureus*, respectively, indicating its potential for broader biomedical applications. Furthermore, Amirnejad *et al.* [50] fabricated HA-TiO_2 composite coatings on 316 stainless steel using electrophoretic deposition, with 5, 10, and 20 wt.% of TiO_2. These coatings displayed excellent adhesion, continuity, and crack-free characteristics. As TiO_2 content increased, bond strength improved, and the corrosion current density in SBF decreased from 18.92 $\mu A/cm^2$ (HA) to 6.35 $\mu A/cm^2$ (HA-20 wt.% TiO_2). These findings suggest that HA-TiO_2 coatings offer enhanced protection and performance for biomedical applications.

Focusing on antibacterial HA-Ag composite coatings, Fu *et al.* [51] coated a Ti substrate with HA and Ag following a two-step electrochemical process. They found that controlling the deposition period allowed a consistent deposition of Ag nanoparticles on the HA layer, both in size and quantity. The antibacterial efficacy against *S. aureus* was consistent, suggesting potential for use in implants to improve osseointegration and prevent post-surgical infections. Similarly, Mirzaee *et al.* [52] used electrophoretic deposition to create Ag-doped HA films, finding that maximal antimicrobial efficacy (> 99%) was achieved at a specific Ag concentration (0.05 at.%). Mokabber *et al.* [53] provided a comparative analysis of two Ag/Calcium Phosphate coating methods using electrochemical deposition. They discovered that the two-step process yielded better biocompatibility and higher antibacterial efficacy (76.1% vs. 83.7%) compared to the one-step process. In a different approach, Lu *et al.* [54] employed pulsed electrochemical deposition to coat a Ti substrate with HA and Ag simultaneously. Despite this distinct methodology, they achieved a consistent dispersion of Ag and emphasised the importance of maintaining an optimal Ag concentration to ensure the desired biocompatibility and antibacterial efficacy.

Despite recent advancements in composite coatings, relatively few studies focus on Mg alloys, and none specifically address the AZ61 alloy produced by WAAM. Additionally, electrodeposition is rarely used for co-depositing HA-TiO_2 and HA-Ag. These research gaps highlight the need for further investigation to explore how the excellent properties of Mg alloys can be combined with the simplicity of electrodeposition.

4

Materials and Methods

The present chapter sequentially details the materials and methods used to accomplish the objectives of this study. Initially, the preparation of the metallic substrates through WAAM is described. Following this, the chapter covers the electrochemical deposition processes for the different coatings, HA, TiO_2, HA-TiO_2 and HA-Ag. Next, the preparation of buffer solutions and the tests used for electrochemical characterisation are outlined. The chapter then elaborates on the morphological, structural, and chemical characterisation methods employed. Lastly, it describes the procedures for conducting *in vitro* degradation and cytotoxicity tests.

4.1 Preparation of the Metallic Substrates by WAAM

The objective of this initial phase was to obtain defect-free components, which could then undergo characterisation in the following stages. A colleague in the Mechanics Department was responsible for conducting the WAAM printing for this purpose.

The key parameters of GMAW-based WAAM include wire feed speed (WFS), travel speed (TS), contact-to-work distance (CTWD), shield gas flow (SGF), and voltage (ΔV). Each of these factors influences specific characteristics of the deposited layers. The parameters employed in a preceding thesis, as shown in Table 4.1, were replicated [55]. The Mg alloy AZ61A (Table 4.2) was selected as the material for this study, and a commercial wire of this alloy was used as the feedstock material for printing.

Table 4.1: Parameters values for the welding process

WFS (m/min)	**TS (mm/min)**	**CTWD (mm)**	**SGF (l/min)**	**ΔV**
3, 3.5, 4, 5.5	500, 550, 700	12, 14, 17, 19	19	-1, -4, -5

Table 4.2: Chemical composition of the Mg alloy AZ61

Element	Magnesium (Mg)	Aluminium (Al)	Zinc (Zn)	Manganese (Mn)	Silicon (Si)
Content (%)	92	5.80 - 7.20	0.40 - 1.50	0.15	0.10

The resulting printed substrate, as shown in Figure 4.1, was cut into smaller pieces using a precision cutting machine (BLUEHLER, IsoMet 4000) with a blade speed of 1400 rpm and a feed rate of 4.8 mm/min. Following the cutting process, the pieces, which displayed no visible imperfections, were polished with 500-grit sandpaper. These procedures ensured the production of defect-free components (Appendix A.1: Figure A.1), which were then thoroughly characterised.

Figure 4.1: Photograph of the printed wall.

4.2 Electrochemical Deposition

As previously mentioned, the coatings were applied using the electrochemical deposition method. The setup, illustrated in Figure 4.2, comprised a DC power supply (TTi, PL303), a working electrode, the Mg substrate, and a counter electrode, which was a graphite rod. Before each deposition, both the working and counter electrodes were cleaned ultrasonically in ethanol for five minutes, rinsed with Millipore water, and then air-dried. The specific conditions, such as the applied constant voltage, coating duration, electrolyte solution, and any pre- and post-treatment procedures, depend on the type of coating being applied. These details will be described in the sections below.

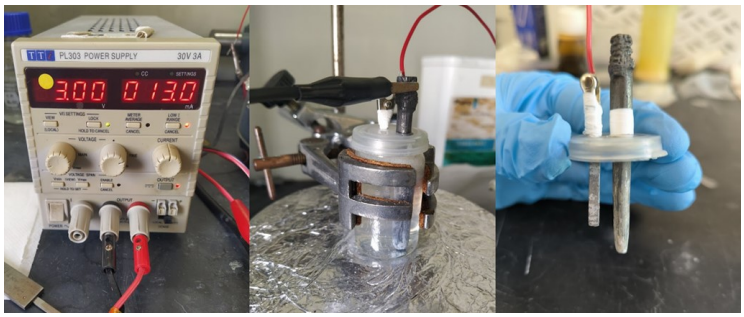

Figure 4.2: DC power supply (left), electrodes submerged in electrolyte solution (middle) and lid used to maintain the electrodes parallel and at the same distance (right).

4.2.1 Hydroxyapatite

To achieve a uniform and compact coating on the Mg sample's surface, three solutions were initially prepared. These included 0.2 M $Ca(NO_3)_2 \cdot 4H_2O$ (Calcium Nitrate Tetrahydrate,

Sigma-Aldrich, ≥ 99%), 0.12 M $NH_4H_2PO_4$ (Ammonium Di-hydrogen Phosphate, PanReac AppliChem, 99%), and 1 M NaOH (Sodium Hydroxide, Sigma-Aldrich, ≥ 97%). The first two solutions were prepared with a 30% (v/v) CH_3CH_2OH (Ethanol Absolute, Honeywell, ≥ 99.8%) as a base for dilution. The third solution was prepared with Millipore water.

Two different protocols were followed, Protocol A, which was based on a previous dissertation [55], and Protocol B, which had some slight variations in the pre- and post-treatments based on the work of other authors [45, 56]. Samples following Protocol A were post-treated by immersion in a 1 M NaOH solution heated to 80°C for two hours. In contrast, the samples coated according to Protocol B underwent a pre-treatment, involving immersion in a 1 M NaOH solution at 80°C for one hour, and a post-treatment that was identical to the pre-treatment. All post-treated specimens were rinsed with Millipore water and then air-dried for 1 hour.

The electrolyte solution, consisting of 0.1 M $Ca(NO_3)_2 \cdot 4H_2O$ and 0.06 M $NH_4H_2PO_4$, was prepared by mixing 10 ml of each of the two initial solutions. During the deposition process, the solution was stirred at 300 rpm and maintained at room temperature. Electrodeposition was conducted at a constant potential of 3 V for 60 minutes, as these conditions have been demonstrated to yield effective results [55].

4.2.2 Titanium Dioxide

As with the previous process involving the HA coating, three solutions were prepared in advance and subsequently combined to form the electrolyte solution. The prepared solutions were: 1 M $C_{19}H_{42}BrN$ (Hexadecyltrimethylammonium Bromide, CTAB, SIGMA, ≥ 98%), 1 M KNO_3 (Potassium Nitrate, SIGMA-ALDRICH, ≥ 99%), and 1 M $TiCl_4$ (Titanium (IV) Chloride, SIGMA-ALDRICH).

The process and conditions were based on a previous dissertation that conducted a comprehensive study of this specific coating, establishing the optimal parameters for achieving a uniform and compact coating on the sample [57]. The electrolyte solution was prepared by adding 0.2 ml of 1 M $C_{19}H_{42}BrN$, 0.2 ml of 1 M $TiCl_4$, and 2 ml of 1 M KNO_3. The final volume of 20 ml was achieved by topping off with Millipore water, resulting in final concentrations of 0.01 M, 0.01 M, and 0.1 M, respectively.

The prepared solution was stirred at 500 rpm for 5 minutes, after which a voltage of 1 V was applied to the circuit for 45 minutes. The coated sample was then rinsed with Millipore water and air-dried for 30 minutes. Subsequently, an annealing process was performed at 450°C for 30 minutes in an oven (Nabertherm B180), after which the sample was left to cool overnight.

4.2.3 Hydroxyapatite and Titanium Dioxide

The combined coating was achieved through a two-step process. First, an HA coating was applied to the Mg alloy surface, following Protocol B as described in Section 4.2.1, since it

achieved better results. Next, TiO_2 was added to the already coated sample, as explained in Section 4.2.2.

Due to the presence of the first coating on the Mg sample, the optimal conditions for TiO_2 deposition from previous findings could no longer be guaranteed, so some conditions were varied to assess efficacy. The potentials applied during the TiO_2 coating were 1 V and 1.5 V, each tested for 45 and 60 minutes.

4.2.4 Hydroxyapatite and Silver

As previously stated, the goal of this project was to develop a coating that can simultaneously withstand corrosion and exhibit antibacterial properties. Ag is undoubtedly an effective antibacterial agent; however, in excess, it is likely to fail cytotoxicity tests [58]. Consequently, an Ag-only coating was deemed a non-viable option.

Prior to the electrodeposition process, two stock solutions were prepared for use in the electrolyte solution: a 20 mM solution of NaCl (Sodium Chloride, SIGMA-ALDRICH, $\geq$ 99.5%), and a 20 mM solution of $AgNO_3$ (Silver Nitrate, SIGMA-ALDRICH, $\geq$ 99.0%).

After following Protocol B for the HA coating, as outlined in Section 4.2.1, the samples were subjected to a double coating with Ag, based on methods from previous studies [51–53]. To prepare the electrolyte solution, 1.25 ml of 20 mM NaCl was mixed with 17.5 ml of Millipore water and heated to 95 ± 1°C. Once the temperature was reached, the working and counter electrodes were immersed in the solution and connected to the voltage source as the anode and cathode, respectively. Subsequently, 1.25 ml of 20 mM $AgNO_3$ was added, and a voltage of 1.4 V was immediately applied.

This procedure was repeated with 5 ml of each stock solution and only 10 ml of Millipore water. As a result, two electrolyte solutions with different concentrations were tested: 1.25 mM NaCl and 1.25 mM $AgNO_3$, and 5 mM NaCl and 5 mM $AgNO_3$. The tests were conducted for varying durations: 6, 30, and 45 minutes for the first electrolyte solution, and 6, 20, and 45 minutes for the second electrolyte solution. Afterward, the samples were rinsed with Millipore water and left to air-dry for one hour.

4.3 Preparation of the Buffer Solutions

Two Phosphate Buffered Saline (PBS) solutions were prepared: one with a neutral pH of 7.4 and the other with an acidic pH of 5.5. To start, two stock solutions, A and B, were prepared. Solution A consisted of 10 mM $Na_2HPO_4 \cdot 2H_2O$ (Sodium Phosphate Dibasic Dihydrate, Fluka Analytical, $\geq$ 98.0%), 138 mM NaCl (Sodium Chloride, SIGMA-ALDRICH, $\geq$ 99.5%), and 2.7 mM KCl (Potassium Chloride, SIGMA-ALDRICH, 99.5-100.5%), in a total volume of 1 L. Solution B contained 10 mM KH_2PO_4 (Potassium Phosphate Monobasic, SIGMA-ALDRICH, 99.5-100.5%), 138 mM NaCl, and 2.7 mM KCl, dissolved into a total volume of 250 ml.

To prepare the PBS solution with a pH of 7.4, 45 ml of solution B was added to 250 ml of solution A. The pH was monitored and adjusted as needed using a pH meter (pHmeter pH1, XS Instruments) to confirm the desired value. For the PBS solution with a pH of 5.5, 12 ml of solution A was added dropwise to 205 ml of solution B, with the pH meter immersed in the solution to check the pH value between each drop, until it reached 5.5. The final concentrations of salts (NaCl and KCl) in both PBS solutions were identical to those in solutions A and B. The total phosphate ($Na_2HPO_4 \cdot 2H_2O$ and KH_2PO_4) concentration was maintained at 10 mM in both solutions.

4.4 Electrochemical characterisation

The electrochemical characterisation was conducted to evaluate the coatings' corrosion resistance. These tests were performed using the previously prepared PBS solutions, allowing for characterisation under both normal physiological pH (7.4) and acidic pH (5.5) conditions. A traditional three-electrode cell setup (Appendix A.1: Figure A.2) was employed, consisting of a graphite bar as the counter electrode, a Ag/AgCl electrode as the reference electrode, and the Mg sample as the working electrode. All electrodes were immersed in the PBS solution. The experiments were conducted using a Gamry Instruments Interface 1010E. The sequence began with measuring the OCP for one hour to allow the system to stabilise. Following that, EIS was performed over a frequency range from 0.005 Hz to 1,000,000 Hz, with 5 points per decade and an amplitude of 10 mV. Finally, PR was measured between -0.4 V and 0.4 V relative to the OCP, with a sweep rate of 1 mV/s. All data collected were analysed using the Gamry Echem Analyst software.

4.5 Morphological, structural, and chemical characterisation

The morphological characterisation was performed using optical microscopy with a Leica DMi8 and SEM with a Hitachi TM3030 Plus. Additionally, elemental analysis was conducted using EDS with a Bruker XFlash MIN SVE. For the structural characterisation of the coatings, XRD was carried out using an XRDynamic 500 by Anton Paar. The 2θ range varied depending on the coating, while the step size was set to $0.01°$ with a time per step of 45.156 seconds. Finally, the chemical characterisation was performed using FTIR with a Thermo Nicolet 6700, covering a spectral range of 400 - 4000 cm^{-1}.

4.6 *In vitro* Degradation Tests

The purpose of this test was to determine the degradation rate of the uncoated Mg alloy AZ61 under static PBS conditions and compare it with the degradation rates of substrates coated with HA and with HA combined with Ag. Eighteen samples were prepared for the immersion test, divided into three groups: six uncoated, six coated with HA, and six coated with HA and Ag. Each sample was measured and weighed prior to the experiment

to establish a baseline for subsequent weight loss measurements. The samples were then divided into two sets, each containing nine samples (three from each group). One set was immersed in PBS solution with a pH of 7.4, while the second set was immersed in PBS solution with a pH of 5.5. Each sample was placed in an individual bottle containing 4 ml of the respective solution (Appendix A.1: Figure A.3). For each measurement, the samples were removed from the PBS solution, cleaned with Millipore water and a soft brush to remove corrosion product buildup, dried, and then weighed. The first measurement was taken on 08/07/2024, and the final measurement on 09/09/2024.

Two measurements were taken from the data collected, Mass Loss (ML) and Corrosion Rate (CR). The ML was calculated using a simple subtraction: $\text{Mass}_{\text{initial}}$ - $\text{Mass}_{\text{final}}$. The CR was determined using the formula $CR = (K \times W)/(A \times T \times D)$, where K is the conversion factor (8.76×10^4), W is the weight variation (g), A is the sample surface area (cm^2), T is the immersion time (hours), and D is Mg's density (1.80 g/cm^3) [59].

4.7 Cytotoxicity Tests

A cytotoxic assay was conducted to evaluate the cytotoxic effects of Mg and the different surface modifications (coated with HA, TiO_2, HA-TiO_2, and HA-Ag) using the extract method based on ISO 10993-5. The analysis was done in the Cell and Tissue Laboratory in the Physics Department.

The samples were sterilised at 120°C for two hours, then placed in McCoy's 5A medium, supplemented with sodium bicarbonate, antibiotics and 10% fetal bovine serum, in order to create extracts (100 mg/ml). Following a 48-hour incubation period at 37°C, the extracts were filtered to remove any residual particulates.

Human osteosarcoma cells (SaOS-2) were seeded in 96-well plates at a density of 30,000 cells per cm^2 and allowed to adhere for a period of 24 hours. The cells were then treated with the pure extract and serial dilutions (50, 25, 12.5, and 6.25 mg/ml) of Mg and its coated variants. To ensure validity, a negative control (culture medium) and a positive control (10% DMSO) were included. The cells were incubated for 48 hours at 37°C in a humidified 5% CO_2 incubator.

The viability of the cells was evaluated at 24 and 48 hours using a resazurin assay. The blue dye resazurin is reduced to the fluorescent pink compound resorufin by metabolically active cells. Following a three-hour incubation period with resazurin, the absorbance was measured at 570 and 600 nm, and the corrected absorbance (X) was calculated to determine cell viability. The results were expressed as the mean of four replicates ± standard uncertainty.

5

Results and Discussion

In this chapter, the results of each coating will be discussed. The analysis will begin with an individual examination of each coating, including an uncoated sample, focusing on the processes that occur during deposition. This will be followed by a comparison of results from SEM, EDS, XRD, and FTIR under the different conditions tested for each coating. Following this, a comparative analysis will be conducted to evaluate the coatings' resistance to corrosion based on the electrochemical experiments and their degradation *in vitro*, finally the outcomes of the cytotoxicity tests will be examined.

5.1 Uncoated Magnesium alloy AZ61

The baseline substrate for this study was the Mg alloy AZ61, and a sample was characterised to serve as a reference point for the coated specimens. The microstructure is illustrated in Figure 5.1. The most notable feature is the presence of parallel lines, typically indicative of a directional mechanical process, which in this case resulted from the polishing process. Additionally, multiple dark spots are visible throughout the sample. EDS analysis (See Appendix A.2, Figure A.18) reveals that these regions are predominantly composed of Carbon (C), likely due to contamination introduced during processing and handling. Overall, the surface is relatively uniform, and the presence of grooves may enhance the adhesion of the coatings. As expected from the EDS analysis (Table 5.1), the surface composition primarily consists of Mg, Al, Zn, and Si, the typical constituents of the AZ61 alloy, with the exception of some contamination from C and Oxygen (O).

Figure 5.2 shows the XRD results of a WAAM-printed Mg alloy AZ61 sample. In this specific sample, only the α-Mg phase is present. However, in other XRD results from coated samples, the β-$Mg_{17}Al_{12}$ phase occasionally appears. Studies have demonstrated that WAAM-printed walls of Mg alloys exhibit varying phase distributions along their length. The top region typically contains higher quantities of the β-$Mg_{17}Al_{12}$ and η-Al_8Mn_5 phases, while the middle and bottom regions are usually composed solely of the α-Mg phase [60, 61]. As a result, the presence of the β-$Mg_{17}Al_{12}$ phase may vary depending on the specific region being analysed.

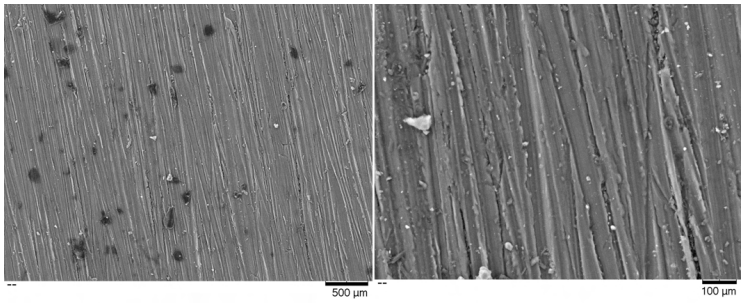

Figure 5.1: SEM of the WAAM-printed Mg alloy AZ61.

Table 5.1: Elemental Composition of Mg alloy AZ61 from EDS Analysis

Element	Mg	C	O	Al	Zn	Si
Atom-% (norm.)	52.27	29.34	14.67	3.48	0.15	0.10

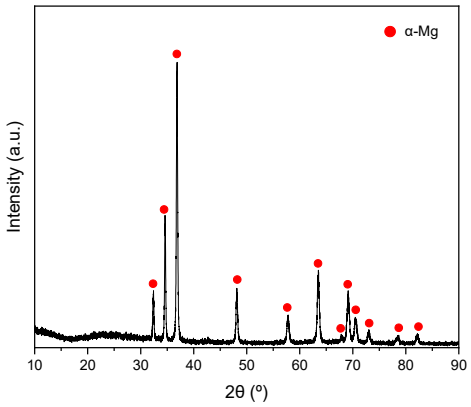

Figure 5.2: XRD of the WAAM-printed Mg alloy AZ61.

5.2 Hydroxyapatite coating

As explained in subchapter 4.2.1, two different protocols were tested. Protocol A closely replicated the protocol identified as the most promising in a preceding thesis. Protocol B, on the other hand, was based on the work of other authors who had studied this coating extensively. The most significant change in Protocol B was the addition of a pre-treatment, along with modifications to the post-treatment process.

The pre-treatment — immersion in 1 M NaOH at 80°C for 1 hour — results in the formation of a $Mg(OH)_2$ layer on the sample surface (Equation 5.1). This layer not only acts as a mild barrier against corrosion but also enhances the mechanical interlocking between the substrate and the coating [62]. The chemical reactions that occur during the electrochemical deposition of HA on the surface of Mg are well-researched. It is widely accepted that the process occurs in two phases. The first phase involves the reduction of hydrogen from $H_2PO_4^-$ and HPO_4^{2-} (Equations 5.2 and 5.3). This is followed by the reaction of Ca^{2+} ions with HPO_4^{2-} and PO_4^{3-}, leading to the formation of $CaHPO_4 \cdot 2H_2O$

and $Ca_3(PO_4)_2$ (Equations 5.4 and 5.5). These compounds are referred to as DCPD and β-Tricalcium Phosphate (β-TCP), respectively, and serve as precursors to HA. The alkaline post-treatment — immersion in 1 M NaOH at 80°C for 2 hours (Protocol A) or 1 hour (Protocol B) — is responsible for transforming the film formed on the surface into HA (Equation 5.6) [43, 45].

$$2OH^- + Mg^{2+} \rightarrow Mg(OH)_2 \tag{5.1}$$

$$2H_2PO_4^- + 2e^- \rightarrow 2HPO_4^{2-} + H_2 \tag{5.2}$$

$$2HPO_4^{2-} + 2e^- \rightarrow 2PO_4^{3-} + H_2 \tag{5.3}$$

$$Ca^{2+} + HPO_4^{2-} + 2H_2O \rightarrow CaHPO_4 \cdot 2H_2O\,(s) \tag{5.4}$$

$$3Ca^{2+} + 2PO_4^{3-} \rightarrow Ca_3(PO_4)_2\,(s) \tag{5.5}$$

$$10CaHPO_4 \cdot 2H_2O\,(s) + 12OH^- \leftrightarrow Ca_6(PO_4)_6(OH)_2\,(s) + 4PO_4^{3-} + 30H_2O \tag{5.6}$$

The goal of this coating was to build on the work previously done by Ribeiro [55], and replicate the process used to create a solid base coating for the combined coatings being developed. During the literature review, the pre-treatment described in Protocol B was frequently mentioned. Therefore, before proceeding, both methods were tested to ensure the best possible HA base coating. Below, the two approaches are compared.

5.2.1 Morphological, Structural and Chemical Analysis

In Figure 5.3, SEM images of both coatings are presented (See individual images in Appendix A.2, Figures A.5 and A.6). The Protocol A coating shows a highly cracked and rough surface with irregularly shaped features. This type of cracking can negatively impact mechanical properties, potentially leading to failure under load. However, rough surfaces also promote better cell adhesion and osseointegration, and a degree of porosity between the granules is evident, which is often desirable for bone ingrowth. In contrast, the Protocol B coating reveals a more uniform surface, with significantly fewer cracks, indicating a more cohesive coating. Although finer and more interconnected, porosity is still present, suggesting that this coating also possesses the necessary characteristics to support bone tissue regeneration. In conclusion, the Protocol B coating exhibits fewer defects and a more uniform surface, which could result in better performance in applications requiring durable and consistent coatings.

The XRD results for both coatings are presented in Figure 5.4 (See individual diffractograms in Appendix A.2, Figures A.27 and A.28). To analyse these results, the Mg alloy peaks were first identified based on a previously analysed diffractogram (as discussed in Section 5.1). The remaining peaks were attributed to HA, based on A.S.T.M. Card No. 9-432 [63]. The absence of DCPD and β-TCP phases in both graphs indicates that the post-treatment effectively transformed these phases into the apatite phase. This suggests that reducing the immersion time from 2 hours to 1 hour does not alter the final composition of the coating.

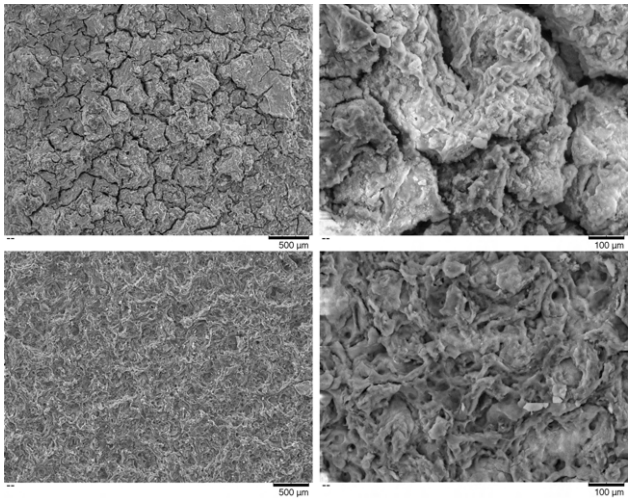

Figure 5.3: SEM of HA-coated Mg alloy AZ61 samples: Protocol A (top) and Protocol B (bottom).

The morphological and structural characterisation was sufficient to conclude that Protocol B produced more promising results. Consequently, subsequent HA coatings were prepared using the steps outlined in Protocol B. Therefore, the FTIR analysis to confirm the chemical composition of the coating and to verify the presence of specific functional groups associated with HA was conducted only on the Protocol B sample.

The FTIR spectrum (Figure 5.5) shows a broad peak around 3400 cm^{-1}, which can be attributed to absorbed water molecules [26, 62]. Additionally, the peak around 1634 cm^{-1} corresponds to the bending vibration of the H-O-H bond in water, indicating the presence of water associated with HA [26]. Peaks observed around 1404 cm^{-1} and 1455 cm^{-1} are attributed to the carbonate ion [26]. The peak at 1012 cm^{-1} is associated with the stretching mode of the P-O group, characteristic of the tetrahedral PO_4^{3-} ions [64, 65]. The peak around 873 cm^{-1} is also attributed to the carbonate ion [26]. Finally, the peaks observed at 599 cm^{-1} and 557 cm^{-1} are attributed to the PO_4^{3-} ions, representing the bending mode of the O-P-O group, confirming the presence of phosphate groups within the HA structure [64, 66]. These peaks confirm the presence of HA in the coating.

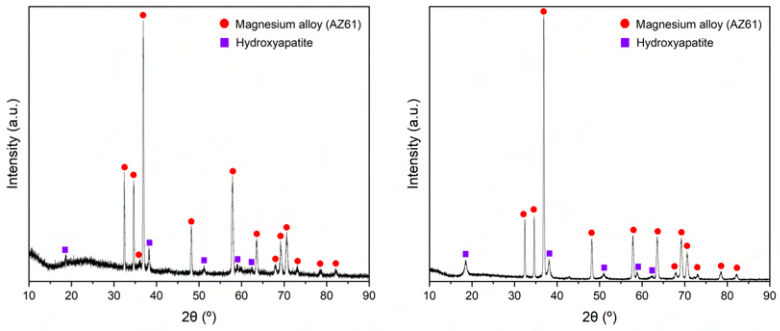

Figure 5.4: XRD of HA-coated Mg alloy AZ61: Protocol A (left) and Protocol B (right).

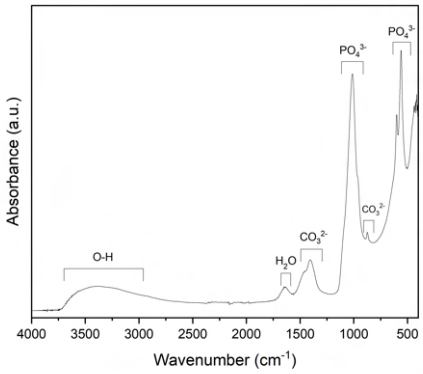

Figure 5.5: FTIR of HA-coated Mg alloy AZ61 (Protocol B).

5.3 Titanium Dioxide Coating

Similar to the HA coating, the TiO_2 coating was also based on a preceding thesis by Passarinho [57]. The electrolyte solution, electrodeposition conditions (time and voltage), and post-treatment were replicated in their entirety.

The selection of the electrolyte solution components — CTAB, KNO_3, and hydrolysed $TiCl_4$ — was based on their specific roles during the deposition process. CTAB was chosen for its ability to promote the formation of thicker and higher-quality TiO_2 films. It reduces electrostatic repulsion between the TiO_2 surface and nitrate ions (NO_3^-), facilitating a more efficient film growth, while also stabilising the film during deposition to produce smoother and more uniform coatings. KNO_3 serves as a source of NO_3^-, which are essential for the electrochemical reactions leading to TiO_2 formation, and it also enhances the conductivity of the electrolyte solution, which is crucial for an efficient deposition. Hydrolysed $TiCl_4$ provides the titanium ions (Ti^{4+}) necessary for the formation of Ti(IV) hydroxide, which subsequently converts to TiO_2 upon annealing [67]. A potential electrochemical deposition mechanism is:

$$NO_3^- + H_2O + 2e^- \rightarrow NO_2^- + 2OH^- \tag{5.7}$$

$$TiO^{2+} + 2OH^- = TiO(OH)_2 \tag{5.8}$$

$$Ti(OH)^{2+} + 2OH^- \rightarrow Ti(OH)_3 \tag{5.9}$$

After the drying and annealing processes, $Ti(OH)_3$ is ultimately transformed into TiO_2. The annealing process at 450°C promotes the formation of the anatase phase of TiO_2. However, at higher temperatures, the more stable rutile phase forms as the crystal structure transitions to this phase during annealing [68].

5.3.1 Morphological, Structural and Chemical Analysis

In Figure 5.6, the SEM analysis of the TiO_2 coating reveals a surface with noticeable cracks and a rough, fragmented texture, indicating a possible need for improvement in

the coating method. The right view further highlights intergranular cracking and uneven grain structures, which could compromise the coating's protective properties. While exhibiting some impairments, the coating demonstrates a solid foundation for further investigation.

The EDS analysis presented in Table 5.2 (See Appendix A.2, Figure A.19) indicates that O is the dominant element in the sample, as expected for oxide-based coatings such as TiO_2. The significant presence of Mg and Al is consistent with the AZ61 alloy used as the substrate. The C detected is likely due to surface contamination. Finally, the presence of Ti confirms the formation of the TiO_2 coating; however, the low percentage suggests that the coating may be thin or not uniformly distributed as desired.

The XRD results (shown in Figure 5.7) confirm the presence of crystal structures characteristic of TiO_2. However, contrary to expectations, the characteristic anatase peak around 25° was not observed in the diffractogram, nor were any other peaks associated with the anatase phase. Instead, only a single peak corresponding to TiO_2 was detected, which is characteristic of the rutile phase [69]. This suggests that the annealing process may have been excessive, as rutile, being the most thermodynamically stable phase of TiO_2, tends to form under such conditions. The peaks identified as belonging to the Mg alloy, similar to the HA coating, were identified based on the diffractogram analysed in Section 5.1.

In Figure 5.7, the FTIR analysis of the TiO_2 coating reveals its chemical structure. The broad peak observed around 3300 cm^{-1} corresponds to the stretching vibration of hydroxyl groups, indicating the presence of surface-bound hydroxyls or adsorbed water molecules [48, 70]. Another peak around 1400 cm^{-1} is characteristic of Ti-O bonding [70], although it could also indicate C-H deformation, potentially from organic residues introduced during the coating process [71]. Additionally, the peak near 850 cm^{-1} is attributed to the Ti-O bond, which typically appears within the 400 - 800 cm^{-1} range, confirming the presence of the TiO_2 phase [72].

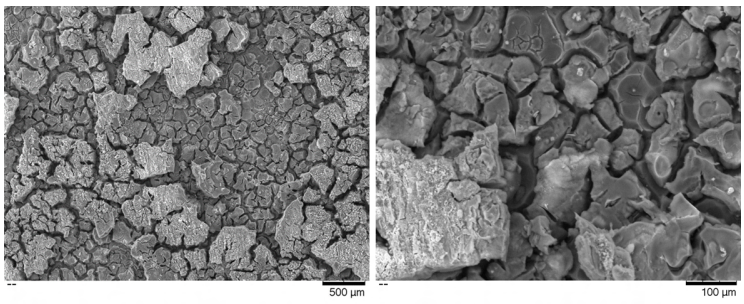

Figure 5.6: SEM of TiO_2-coated Mg alloy AZ61.

Table 5.2: Elemental Composition of TiO_2-coated Mg alloy AZ61 from EDS Analysis

Element	**O**	**Mg**	**C**	**Al**	**Ti**
Atom-% (norm.)	58.74	19.03	12.84	6.94	1.25

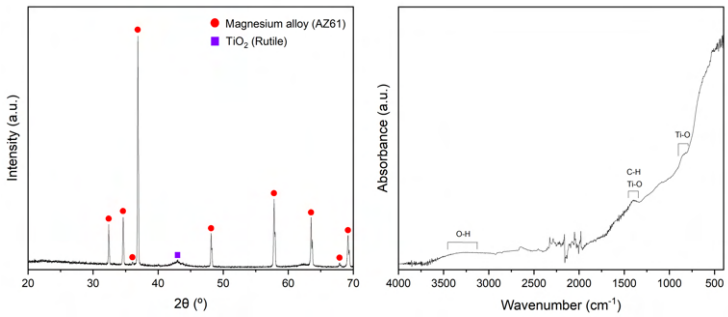

Figure 5.7: XRD (left) and FTIR (right) of TiO_2-coated Mg alloy AZ61.

5.4 Hydroxyapatite and Titanium Dioxide Coating

As detailed in Section 4.2.3, the combined coating was achieved through a double-coating process. First, the HA coating was applied following Protocol B, which was identified as the most promising approach. Next, the TiO_2 coating was applied under the conditions found to be optimal. Given that the base substrate changed from uncoated to HA-coated, it was uncertain whether the same conditions would be effective. Therefore, in addition to the standard conditions of 1 V for 45 minutes, alternative conditions — 1 V for 60 minutes and 1.5 V for both 45 and 60 minutes — were also tested.

5.4.1 Morphological, Structural and Chemical Analysis

The SEM images, presented in Figure 5.8 (See individual images in Appendix A.2, Figures A.8 through A.11), illustrate the surface morphology of the HA-TiO_2 double coatings under varying voltage and time conditions. Upon initial observation, clear similarities between the coatings are apparent, all exhibiting a porous, rough surface typical of such coatings. These qualities are significant for biomedical applications, such as implants, as they facilitate biological integration. Furthermore, all coatings display a granular morphology, indicating that the deposition process produces a consistent texture. Some cracks are also evident, likely caused by stresses from coating or drying processes.

However, upon closer inspection, it becomes evident that different conditions lead to variations in the size and distribution of the granules. In image (a) — 1 V for 45 minutes — the surface appears relatively uniform, with smaller and more densely packed granules, likely due to the shorter deposition time or lower voltage. Despite this, porosity remains present. Extending the deposition time to 60 minutes, as shown in image (b), results in larger granules and a more irregular structure. The porosity becomes more pronounced, with greater interstitial space between the granules. In image (c) — 1.5 V for 45 minutes — the granules are larger, and the surface rougher compared to the 1 V samples. The increased voltage accelerates the deposition process, leading to a more uneven coating. Finally, in image (d) — 1.5 V for 60 minutes — the coating displays the largest granules, the most irregular structure, and the highest porosity.

The XRD patterns, shown in Figure 5.9 (See individual diffractograms in Appendix A.2,

Figures A.30 through A.33), illustrate the crystalline phases present in the HA-TiO_2 double coatings under different deposition conditions. Across all samples, peaks corresponding to the Mg alloy substrate are clearly detectable and dominate the diffractograms, indicating that the coatings are relatively thin. These peaks were identified based on the diffractogram analysis in Section 5.1. The HA peaks were assigned according to A.S.T.M. Card No. 9-432 [63], while the TiO_2 peak was characterised using the diffractogram presented in Section 5.3.1. The coating formed at 1 V for 45 minutes shows low intensity for both HA and TiO_2 peaks. Extending the deposition time to 60 minutes at the same voltage slightly increases their intensity, suggesting a thicker or more crystalline coating compared to the shorter deposition time. When the voltage is increased to 1.5 V for 45 minutes, the intensity of the coating peaks further increases, even with the shorter deposition time, indicating a more pronounced coating. However, this trend does not persist at 1.5 V for 60 minutes, where the intensity of the HA and TiO_2 peaks is similar to that observed in the first deposition condition.

Although the intensity of the HA and TiO_2 peaks is somewhat lower, the 1 V for 45 minutes condition results in a more controlled and uniform coating, as evidenced by the SEM images. The surface shows greater density and cohesion, which is crucial for forming a strong protective barrier against corrosion. Despite being thinner or less crystalline, this denser structure is more advantageous when uniformity and corrosion resistance are prioritised. Therefore, the double coating following Protocol B for HA, combined with the original conditions (1 V for 45 minutes) for TiO_2, was selected.

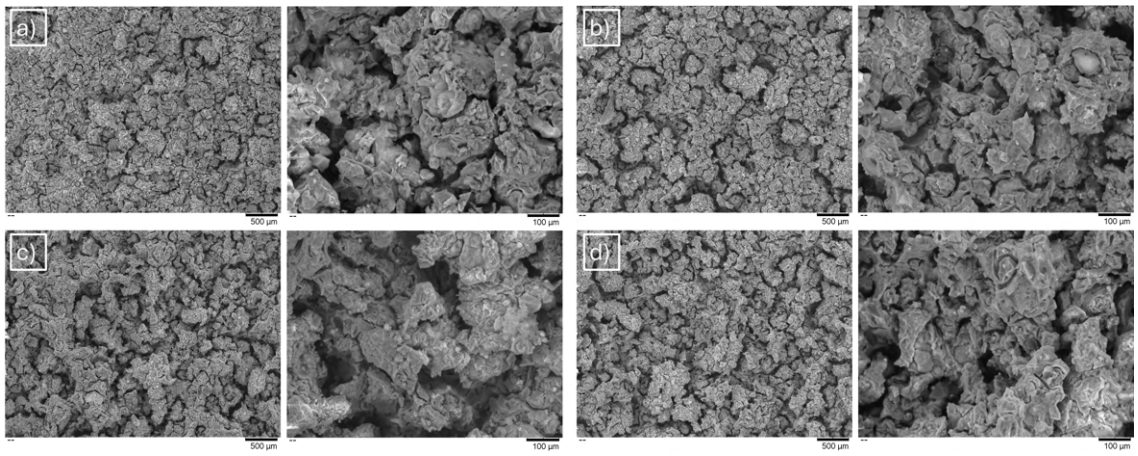

Figure 5.8: SEM of HA-TiO_2-coated Mg alloy AZ61 samples: a) 1 V for 45 minutes; b) 1 V for 60 minutes; c) 1.5 V for 45 minutes; d) 1.5 V for 60 minutes.

Following the morphological and structural analysis to determine the optimal coating conditions, chemical characterisation was performed on the 1 V for 45 minutes sample using FTIR, as presented in Figure 5.10. Three primary peaks are observed. The first significant peak appears around 3350 cm^{-1} and is attributed to the stretching vibrations of hydroxyl groups [48, 70]. This peak suggests the presence of absorbed water molecules in the coating, which is common in HA. The second peak at approximately 1400 cm^{-1}

represents the carbonate ions in the HA structure, associated with the vibrational mode (ν_3) of the carbonate group [48]. The large peak in the 1000 cm^{-1} to 400 cm^{-1} region likely arises from the overlapping vibrations of phosphate groups in the HA and Ti-O/Ti-O-Ti bonds in the TiO_2 phase [48]. This indicates that the coating retains the typical features of HA while incorporating TiO_2 into its matrix.

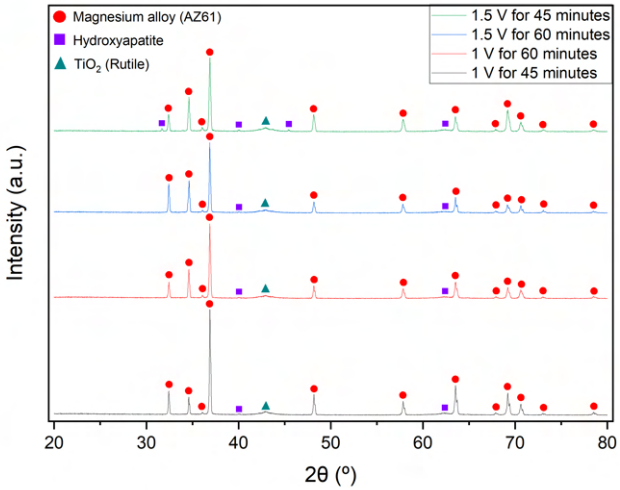

Figure 5.9: XRD of HA-TiO_2-coated Mg alloy AZ61 samples.

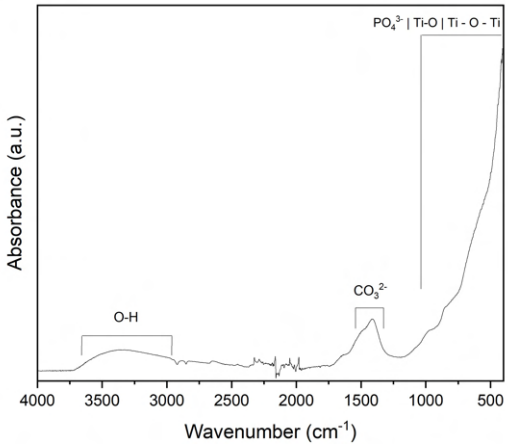

Figure 5.10: FTIR of HA-TiO_2-coated Mg alloy AZ61 sample (1 V for 45 minutes).

5.5 Hydroxyapatite and Silver Coating

As explained in Section 4.2.4, in order to determine the optimal combination of HA and Ag, two different electrolyte solutions were tested: Solution A, a low-concentration electrolyte (1.25 mM NaCl and 1.25 mM $AgNO_3$), and Solution B, a high-concentration electrolyte (5 mM NaCl and 5 mM $AgNO_3$). For Solution A, deposition times of 6, 30, and 45 minutes were used, while for Solution B, deposition times of 6, 20, and 45 minutes were tested.

Through morphological, elemental, and structural analysis, the optimal conditions for the double coating were identified. The Ag content in the coatings is a crucial factor: high Ag content reduces biocompatibility, while low Ag content compromises antibacterial efficacy. Therefore, the aim was to develop a coating that balances these two factors.

5.5.1 Morphological, Structural and Chemical Analysis

The surface morphology of the HA-Ag coatings varied depending on the electrolyte concentration and deposition time, as shown in Figure 5.11 (See individual images in Appendix A.2, Figures A.12 through A.17). The Ag deposits formed dendrite-like structures, visually identifiable as whitish areas on the surface, ranging from sparse to clustered, with the ideal outcome being a uniform and well-distributed deposition.

Starting with the low-concentration electrolyte, in condition (a) with a 6-minute deposition time, the surface exhibits minimal deposition. The Ag particles are small, sparse, and cover only limited areas. Extending the deposition time to 30 minutes in condition (b) results in more noticeable coverage, with the whitish areas becoming more prominent and evenly distributed, though still somewhat light. In condition (c), where deposition lasts for 45 minutes, the Ag coverage increases significantly, forming more continuous patterns. However, the distribution becomes less uniform, with some areas showing excessive deposition.

In the high-concentration electrolyte, condition (d) with a 6-minute deposition time shows slightly more deposition than condition (a), but it remains sparse with limited surface coverage. Condition (e), with a 20-minute deposition time, presents a more evenly distributed Ag layer, with uniform coverage and Ag dendrites that are not overly clustered. In contrast, condition (f), involving a 45-minute deposition, shows only marginally more deposition than conditions (a) and (d). This may indicate that Ag did not adhere as effectively, possibly due to over-saturation of the solution.

In conclusion, conditions (b) and (e) appear to achieve the most balanced and even Ag deposition, avoiding the sparsity seen in conditions (a), (d), and (f), as well as the excessive clustering observed in condition (c). However, further analysis is required to confirm these findings.

The elemental composition data, presented in Table 5.3 (See Appendix A.2, Figures A.20 through A.25), corroborates that sample (c) exhibits an excessively high Ag content (43.68%), while samples (a) (0.22%) and (d) (1.11%) show insufficient coverage, with sample (a) being particularly deficient. For sample (f), the EDS results reveal better Ag deposition (1.64%) than expected, similar to sample (b), although the distribution remains suboptimal. In contrast, samples (b) (1.82%) and (e) (3.39%) stand out as the most favourable conditions for achieving a balanced and well-distributed Ag coating. Notably, sample (b) maintains a better balance of Ca and P compared to sample (e) (2.72% and 1.01% vs. 1.80% and 0.99%). The presence of these HA components indicates that the underlying layer remains intact.

Regarding the other elements, Mg content is relatively stable across the samples

(ranging from 2.84% to 14.80%), while O content remains consistently high (64.72% to 74.27%). The remaining elements are either residual from the alloy (Al and Si) or contaminants (C).

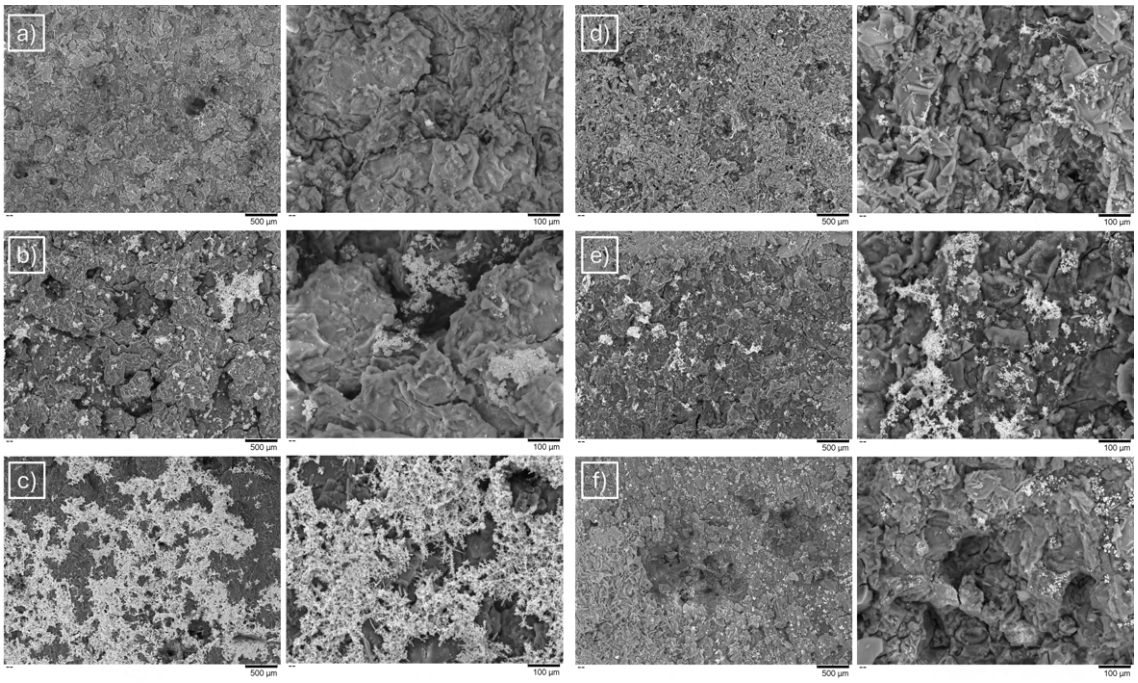

Figure 5.11: SEM of HA-Ag-coated Mg alloy AZ61 samples: a) Solution A for 6 minutes; b) Solution A for 30 minutes; c) Solution A for 45 minutes; d) Solution B for 6 minutes; e) Solution B for 20 minutes; f) Solution B for 45 minutes.

Table 5.3: Elemental Composition of HA-Ag-coated Mg alloy AZ61 samples from EDS Analysis

		Element							
		Ag	**Ca**	**P**	**Mg**	**O**	**C**	**Al**	**Si**
Atom-% (norm.)	**a) Solution A - 6 min.**	0.22	1.70	1.57	13.00	64.72	12.65	2.11	3.95
	b) Solution A - 30 min.	1.82	2.72	1.01	13.76	74.27	-	2.95	3.40
	c) Solution A - 45 min.	43.68	23.01	11.34	2.84	-	17.71	-	-
	d) Solution B - 6 min.	1.11	12.21	6.05	6.67	70.61	-	-	1.42
	e) Solution B - 20 min.	3.39	1.80	0.99	14.07	74.01	-	2.60	3.05
	f) Solution B - 45 min.	1.64	3.42	2.37	14.80	72.43	-	1.97	2.81

To further complement this characterisation and determine the optimal parameters, a structural analysis was conducted using XRD, Figure 5.12 (See individual diffractograms in Appendix A.2, Figures A.34 through A.39). The peaks were identified as Mg alloy, based on the diffractogram analysed in Section 5.1; HA, according to the diffractogram analysed in Section 5.2.1 and the A.S.T.M. Card No. 9-432 [63]; and Ag, based on Ag nanoparticle diffractograms reported in literature [73, 74]. Ag exhibits three characteristic peaks at 38°, 44°, and 64.5° in the XRD pattern. Depending on the amount deposited, the number and intensity of these peaks vary. Samples (a) and (d), which have low Ag

content, show only a weak peak at 38°. In contrast, sample (c) displays all three peaks with high intensity, owing to the high Ag content observed in the EDS analysis. Unexpectedly, the XRD results for samples (e) and (f) did not entirely match the previous SEM and EDS observations. Sample (e), thought to have achieved good Ag deposition, shows only a single peak, similar to samples (a) and (d). Meanwhile, sample (f), initially expected to have minimal Ag on its surface, surprisingly exhibits all three peaks, with notable intensity. Lastly, sample (b) presents all three peaks as well, though with lower intensity compared to samples (c) and (f), which aligns with the previous results.

Finally, FTIR analysis was performed on the sample with the highest Ag content (Solution A, 45 minutes) to extrapolate the results to the other samples. As shown in Figure 5.13, the spectrum closely resembles that analysed in Section 5.2.1, displaying only the characteristic peaks of HA. As expected, the presence of Ag does not alter the chemical bonds or functional groups [52].

In conclusion, sample (b) (Solution A, 30 minutes) demonstrates a balanced Ag deposition with a consistent elemental composition and well-distributed peaks in the XRD analysis. Although the peaks are not the most intense, they align well with the expectations from the SEM and EDS characterisations. The results indicate that this coating is stable and effective, justifying its selection for further analysis.

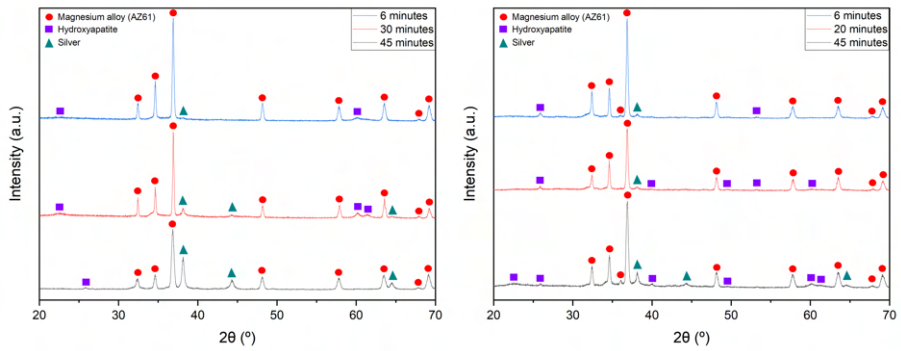

Figure 5.12: XRD of HA-Ag-coated Mg alloy AZ61 Samples: Solution A (Left) and Solution B (Right).

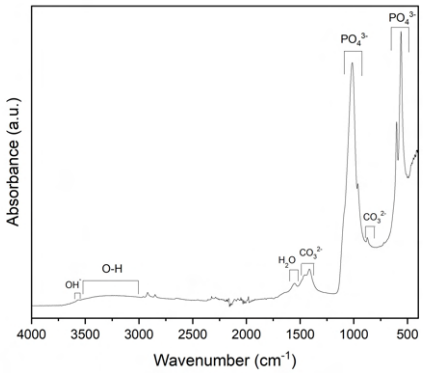

Figure 5.13: FTIR of HA-Ag-coated Mg alloy AZ61 Sample (Solution A, 45 Minutes).

5.6 Electrochemical Experiments

In this chapter, a comprehensive electrochemical analysis is carried out to evaluate the corrosion behaviour and electrochemical properties of the samples. OCP, PR, and EIS measurements were performed to assess the stability, corrosion resistance, and overall performance of both coated and uncoated samples. These tests were conducted on six samples: uncoated, coated with HA (Protocol A and B), coated with TiO_2, coated with HA and TiO_2 (1 V for 45 minutes), and coated with HA and Ag (Solution A for 30 minutes), using two PBS solutions with pH levels of 7.4 and 5.5.

5.6.1 Open Circuit Potential

The OCP provides information about the material's thermodynamic propensity to corrode in the absence of an external current. A nobler (less negative) OCP implies a lower thermodynamic tendency to corrode [75]. To investigate the free corrosion behaviour of the samples, an OCP measurement was conducted for 60 minutes. The resulting plots are presented in Figure 5.14 (See the individual plots in Appendix A.2, Figures A.40 through A.42).

In PBS at pH 7.4, the OCP behaviour of the Mg sample (Black) starts at -1.564 V, gradually rising to a stable value of -1.478 V by the 60^{th} minute. This stabilisation is linked to the formation of a protective film on the alloy surface. The HA-coated samples exhibit distinct behaviours depending on the coating protocol. The Protocol B sample (Blue) starts at -1.796 V and fully stabilises at -1.423 V. In contrast, the Protocol A specimen (Red) shows continuous oscillations throughout the measurement, ending with an OCP of -1.457 V. This aligns with the conclusions from Section 5.2, confirming that Protocol B provides a more stable and protective coating.

For the TiO_2-coated substrate (Green), the OCP begins at -1.581 V, then shifts cathodically to -1.587 V, finishing at -1.552 V without full stabilisation. However, the sample with the HA-TiO_2 double coating (Purple) starts at -1.515 V, steadily reaching -1.207 V before shifting anodically to -0.133 V, where it stabilises. This suggests that the TiO_2 coating alone does not offer adequate protection, as its OCP is more negative than that of the uncoated sample. When combined with HA, however, the OCP becomes 1.419 V nobler, indicating a highly protective layer.

Finally, the substrate coated with HA and Ag (Yellow) shows a rapid initial increase, followed by a significant jump to -0.177 V, then a drop to -0.568 V, ending with an oscillating OCP around -0.381 V. The considerable anodic shift in both double coatings suggests they provide effective protection, with the purple sample (HA-TiO_2) standing out as the most stable and noblest of all the samples.

In PBS at pH 5.5, the OCP of the Mg sample (Black) initially rises from -1.759 V to -1.688 V, reaching a relatively steady state and finishing with an OCP of -1.658 V. For the HA-coated samples, the Protocol A sample (Red) starts at -1.542 V, quickly increasing

to -1.351 V, before experiencing a cathodic shift and ending at -1.493 V after a gradual decline. The Protocol B sample (Blue) follows a similar pattern, beginning at -1.469 V, rising to -1.417 V, and then continuously declining until stabilising at -1.542 V. In the acidic medium, Protocol B achieves a more negative potential, suggesting a slightly poorer protective performance compared to Protocol A. The TiO_2-coated substrate (Green) begins with an OCP of -1.774 V, gradually increasing with minor oscillations to finish at -1.722 V. As with the pH 7.4 test, its OCP remains more negative than that of the uncoated sample.

The HA-TiO_2-coated sample (Purple) initially drops from -1.628 V to -1.701 V, oscillates for a time, then steadily rises to -1.673 V. In this acidic environment, the combined coating's protective capacity is reduced compared to its performance at pH 7.4; while it performs better than TiO_2 alone, it is less effective than pure HA. Finally, the HA-Ag-coated substrate (Yellow) shows an initial cathodic shift from -1.478 V to -1.551 V, followed by a steady rise to -1.339 V. After a second drop to -1.394 V, it oscillates before concluding the measurement at -1.395 V. Although this coating remains somewhat unstable at this pH, it ends with the least negative potential, indicating a good protective performance.

The OCP measurements reveal that the pH of the PBS solution significantly impacts the corrosion behaviour of the various coated samples. As pH increases, the corrosion rate generally decreases, as higher pH levels create conditions that improve the stability and protective effectiveness of the coatings, while acidic environments increase reactivity and accelerate corrosion rates [76]. The double coatings, in particular, demonstrate a marked ability to protect the Mg alloy under both pH conditions, even though their effectiveness is greater in neutral environments.

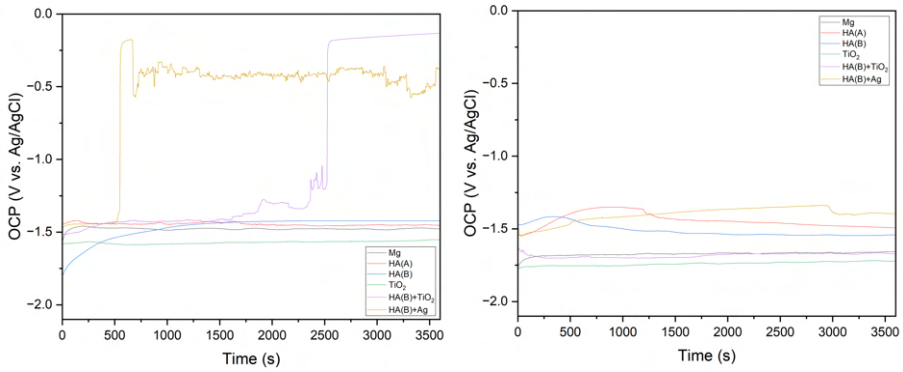

Figure 5.14: OCP (PBS pH 7.4 (left) and pH 5.5 (right)) of: Uncoated (Black); HA-coated — Protocol A (Red) and Protocol B (Blue); TiO_2-coated (Green); HA-TiO_2-coated (Purple); HA-Ag-coated (Yellow) Mg alloy AZ61.

5.6.2 Polarisation resistance

Figure 5.15 (See individual graphs in Appendix A.2, Figures A.43 and A.44) presents the polarisation curves for both uncoated and coated substrates, with the corresponding polarisation parameters summarised in Table 5.4. These results were obtained through

potentiodynamic polarisation measurements, where the electrode potential is systematically varied, and the resulting current density is recorded. Key corrosion parameters — including Corrosion Current Density (I_{corr}), Corrosion Potential (E_{corr}), Polarisation Resistance (R_p), and CR — were calculated from the curves. Generally, a lower I_{corr} and CR, a more positive E_{corr}, as well as higher R_p values, indicate improved corrosion resistance [75, 77].

In a neutral medium, the HA-TiO_2 sample demonstrates the best corrosion resistance, showing a significant reduction in I_{corr} to 0.238 $\mu A/cm^2$ — nearly three orders of magnitude lower than the uncoated sample (139.541 $\mu A/cm^2$). The HA-Ag coating also performs well, with an I_{corr} of 0.404 $\mu A/cm^2$. Both combined coatings exhibit the most positive E_{corr} values (-0.119 V for HA-TiO_2 and -0.095 V for HA-Ag) and the highest R_p values (92.41 kΩ and 48.88 kΩ, respectively).

Among the single coatings, HA(B) provides better protection compared to HA(A) and TiO_2, with TiO_2 showing the weakest performance overall. The polarisation curves highlight the presence of a passivation region — a zone where an increase in potential does not correspond to a rise in current density, indicating a stable protective behaviour. The combined coatings exhibit the widest passivation regions (~ 0.1 V), followed by the HA coatings (~ 0.08 V). In contrast, both the uncoated and TiO_2-coated samples lack a passivation region, correlating with their lower corrosion resistance.

However, changing the solution from neutral to acidic significantly affects the results. The HA-Ag coated AZ61 alloy, which was one of the top-performing coatings in a neutral environment, becomes the poorest performer in acidic conditions. Its I_{corr} (38.900 $\mu A/cm^2$) is only marginally better than that of the uncoated sample (49.538 $\mu A/cm^2$), while its R_p (0.427 kΩ) is the lowest, and its CR (0.708 mm/y) the highest. The HA-TiO_2 coating also performs poorly in acidic conditions, followed by TiO_2, which shows weak performance in both environments.

In contrast, the HA coatings are the best performers in acidic conditions, with HA (A) proving to be the most protective. The passivation regions observed in the cathodic branches further support these conclusions. Only the HA-coated samples display a passivation region, even though the steeper slopes, comparing to those in pH 7.4, indicate reduced stability.

Table 5.4: Results of potentiodynamic corrosion tests in PBS solution (pH 7.4 and 5.5)

Substrate	**I_{corr} ($\mu A/cm^2$)**		**E_{corr} (V)**		**R_p (kΩ)**		**CR (mm/y)**	
	pH 7.4	**pH 5.5**	**pH 7.4**	**pH 5.5**	**pH 7.4**	**pH 5.5**	**pH 7.4**	**pH 5.5**
Uncoated AZ61 alloy	139.541	49.538	-1.347	-1.525	0.287	0.715	1.052	0.423
HA(A)-coated AZ61 alloy	3.761	5.793	-1.518	-1.476	10.62	8.802	0.029	0.034
HA(B)-coated AZ61 alloy	2.565	18.295	-1.456	-1.547	15.93	2.010	0.019	0.150
TiO_2-coated AZ61 alloy	6.079	12.900	-1.478	-1.417	4.64	1.662	0.065	0.182
HA(B)-TiO_2-coated AZ61 alloy	0.238	12.205	-0.119	-1.419	92.41	1.473	0.003	0.205
HA(B)-Ag-coated AZ61	0.404	38.900	-0.095	-1.258	48.88	0.427	0.006	0.708

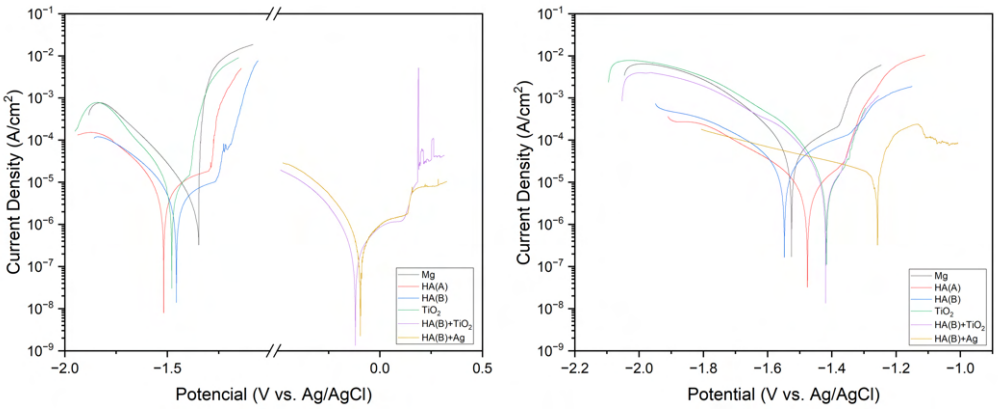

Figure 5.15: Polarisation curves (PBS pH 7.4 (left) and pH 5.5 (right)) of: Uncoated (Black); HA-coated — Protocol A (Red) and Protocol B (Blue); TiO_2-coated (Green); HA-TiO_2-coated (Purple); HA-Ag-coated (Yellow) Mg alloy AZ61.

5.6.3 Electrochemical Impedance Spectroscopy

EIS involves applying a small-amplitude sinusoidal potential perturbation (e.g., 10 mV) to the working electrode over a wide frequency range (e.g., 5 mHz to 1 MHz). The resulting current response is a sinusoidal signal of the same frequency but with a phase shift and amplitude that differ from those of the applied perturbation [78]. By analysing these differences, one can derive information about the impedance characteristics of the electrode and the electrochemical processes occurring at the surface. Figure 5.16 presents the various plots extracted from this EIS analysis (See the individual versions in Appendix A.2, Figures A.45 through A.51).

The Bode magnitude plots of the EIS spectra provide valuable insights into the protective performance of the different coatings. The Impedance Modulus (|Z|) at low frequencies is a strong indicator of protection; generally, the higher the |Z| value, the better the corrosion resistance of the coating [79]. In the neutral environment, at a lower frequency (0.1 Hz), the |Z| values increase in the following order: TiO_2-coated (3.469 kΩ.cm^2) < uncoated (5.372 kΩ.cm^2) < HA-Ag-coated (8.357 kΩ.cm^2) < HA(B)-coated (11.373 kΩ.cm^2) < HA(A)-coated (12.643 kΩ.cm^2) < HA-TiO_2-coated (49.528 Ω.cm^2).

When analysing the results in the acidic medium, the order changes to: uncoated (0.823 kΩ.cm^2) < TiO_2-coated (0.870 kΩ.cm^2) < HA(B)-coated (1.407 kΩ.cm^2) < HA-TiO_2-coated (2.000 kΩ.cm^2) < HA(A)-coated (4.206 kΩ.cm^2) < HA-Ag-coated (4.265 kΩ.cm^2). These results suggest that the uncoated and TiO_2-coated samples offer the least protection, while the combined coatings (HA-TiO_2 and HA-Ag) exhibit good corrosion resistance, with HA-Ag showing strong performance in both solutions. The HA coatings provide a good middle ground, with HA(A) standing out in the acidic environment.

In the Bode phase plots, in PBS at pH 7.4, the uncoated, TiO_2-coated, and HA(B)-coated samples exhibited a single time constant in the medium frequency region, which typically corresponds to the double-layer capacitance and charge transfer resistance during the corrosion process. In contrast, the other three samples displayed two distinct time

constants: one at high frequencies and another at medium frequencies. The high-frequency time constant is generally associated with the barrier effect created by a uniform and less porous coating, indicating stronger corrosion resistance. The presence of both high- and medium-frequency time constants suggests that these coatings offer better overall protection [80]. In PBS at pH 5.5, only the double coatings exhibit two distinct time constants.

The electrochemical impedance behaviour of the uncoated and coated samples is also represented by Nyquist plots. A larger diameter of the capacitive loop in the Nyquist plot typically indicates higher impedance, correlating with greater corrosion resistance [58]. In both solutions, the coated samples — except for the TiO_2-coated one — exhibit significantly larger impedance values across the frequency range compared to the uncoated sample. This suggests that the coatings act as barriers, effectively reducing ion diffusion and slowing the corrosion process. In particular, composite coatings show even larger capacitive loop diameters (HA-TiO_2 in pH 7.4 and HA-Ag in pH 5.5) than the single coatings, indicating enhanced protection against corrosion.

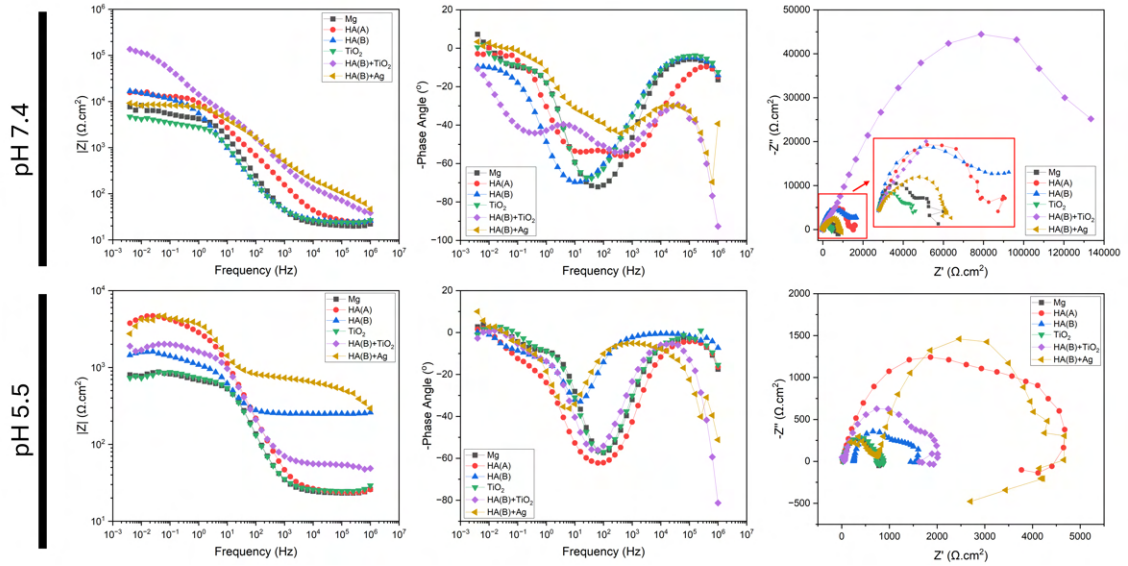

Figure 5.16: EIS (Bode and Nyquist) curves of: Uncoated (Black); HA-coated — Protocol A (Red) and Protocol B (Blue); TiO_2-coated (Green); HA-TiO_2-coated (Purple); HA-Ag-coated (Yellow) Mg alloy AZ61.

5.7 *In vitro* Degradation Tests

In this test, the *in vitro* degradation behaviour of uncoated, HA-coated, and HA-Ag-coated Mg alloy AZ61 was assessed using immersion tests in PBS solutions at pH 7.4 and pH 5.5. Six samples of each type were submerged for 63 days, with three immersed in each pH condition. ML and CR were calculated from weight measurements before and after immersion, with the results summarised in Table 5.5 (See extended version in Appendix A.2, Table A.1). Additionally, a morphological and elemental analysis of the samples after

immersion was conducted (Figure 5.17). For individual analyses, see Appendix A.2 — Figures A.52 through A.57 for the morphological analysis and Table A.2 and Figures A.58 through A.63 for the elemental analysis.

Interestingly, the uncoated Mg exhibited a mass gain in neutral pH, likely due to the formation and adherence of corrosion products such as phosphates, which were not fully removed during the cleaning process. Elemental analysis confirmed the presence of P, further supporting this hypothesis, and SEM surface analysis corroborated these findings, showing needle-like deposits on the surface. However, under acidic conditions, the uncoated Mg experienced severe degradation, with the highest ML and CR recorded in the study. The SEM images showed significant pitting and cracking, highlighting the aggressive nature of corrosion in acidic environments.

The HA-coated Mg samples demonstrated significantly better corrosion resistance. While the ML was higher in the acidic solution, it remained much lower compared to the uncoated samples, indicating effective corrosion protection. SEM analysis revealed an intact coating under both pH conditions, with minimal degradation. The CR values for HA-coated samples were the lowest across both conditions, although slightly higher in the acidic medium, suggesting the coating is effective.

On the other hand, the HA-Ag-coated Mg samples exhibited higher ML and CR compared to HA-coated samples, particularly in the acidic medium, where the CR was nearly as high as that of the uncoated Mg. Although the neutral pH samples showed no visible cracks in the SEM analysis, the acidic samples exhibited surface cracking and roughening, likely contributing to the increased ML. The significant reduction in Ag content observed in the elemental analysis suggests possible Ag leaching, further enhancing the ML recorded. This finding implies that the inclusion of Ag, while intended to enhance antibacterial properties, may weaken the coating's resistance to corrosion, especially in acidic conditions.

When comparing these immersion test results to those from electrochemical tests, notable differences emerge. The electrochemical CR for uncoated Mg at pH 7.4 was significantly higher than that from immersion testing, whereas the CR at pH 5.5 was more consistent between both methods. For the HA-coated Mg, both methods yielded low CR values, though the electrochemical tests revealed a more pronounced difference between pH conditions. The HA-Ag-coated Mg, particularly at pH 7.4, exhibited a large discrepancy between the two testing methods, with the immersion test showing a much higher CR than expected based on electrochemical data, as for pH 5.5 both methods revealed a fairly high CR. These discrepancies raise questions about the reliability of immersion tests for evaluating the CR.

While immersion tests provide valuable long-term data and simulate real-world conditions, they have limitations that could lead to disparity of CR values. Incomplete removal of corrosion products and environmental variability can misrepresent the results, as seen in the case of the uncoated Mg in neutral pH. Electrochemical tests, on the other hand, offer real-time monitoring and controlled conditions, making them more reliable.

Therefore, the electrochemical tests results are likely a more accurate reflection of the true degradation behaviour of the Mg alloys and coatings in different pH environments.

In conclusion, while the HA coating provides strong corrosion protection in both neutral and acidic conditions, the addition of Ag impairs its effectiveness, particularly in acidic environments, so further optimisation is necessary.

Table 5.5: Mass Loss and Corrosion Rate values (after 63 days of immersion) from *in vitro* degradation tests

	Uncoated Mg		**HA-coated Mg**		**HA-Ag-coated Mg**	
	pH 7.4	**pH 5.5**	**pH 7.4**	**pH 5.5**	**pH 7.4**	**pH 5.5**
ML (g)	-0.0013	0.0178	0.0013	0.0016	0.0103	0.0149
CR (mm/year)	-0.0617	0.7167	0.0624	0.0721	0.4409	0.6772

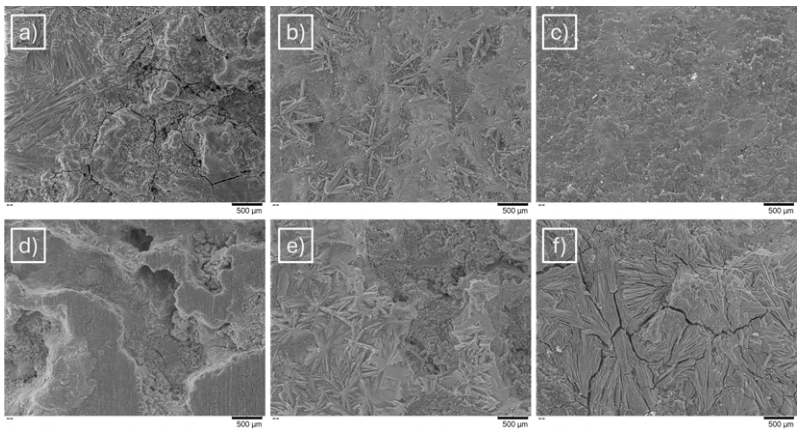

Figure 5.17: SEM of Mg alloy AZ61 after 63 days of immersion: Uncoated in pH 7.4 (a) and pH 5.5 (d); HA(B)-coated in pH 7.4 (b) and pH 5.5 (e); HA(B)-Ag-coated in pH 7.4 (c) and pH 5.5 (f).

5.8 Cytotoxicity Tests

In Figure 5.18 (See individual graphs in Appendix A.2, Figures A.64 and A.65), the cytotoxicity analysis is presented, showing high cell viability across all tested concentrations for the uncoated (102% - 103%), HA-coated (96% - 111%), TiO_2-coated (102% - 105%), and HA-TiO_2-coated (94% - 106%) Mg samples. This indicates strong cytocompatibility, as the materials do not appear to be harmful to cells. Whilst a slight reduction in viability is observed at higher concentrations, this decrease is not significant enough to consider the samples cytotoxic. According to ISO 10993-5 standards, a cell viability greater than 70% of the control group indicates that the material is non-cytotoxic [81].

However, the behaviour of the Ag-containing samples is more complex. Ag is known for its antimicrobial properties but can exhibit varying levels of citotoxicity depending on physicochemical properties such as size, shape and concentration. To investigate this, three different deposition times of 6, 30, and 45 minutes using solution A were

tested. Interestingly, HA-Ag(6), which contains the lowest Ag content, exhibited lower cell viability compared to HA-Ag(30) and HA-Ag(45). This aligns with the expectation that smaller Ag nanoparticles lead to greater cytotoxicity, suggesting that factors such as Ag distribution or release kinetics influence the cytotoxic response [82]. However, the second-highest cytotoxicity is observed in the HA-Ag(45) sample, which has the largest particles, contradicting this trend. Nevertheless, since it has the highest concentration, these results are reasonable.

The graph also presents two columns for each concentration, one representing 24 hours and the other 48 hours. It is evident that the second column (48 hours) shows an improvement in viability across all concentrations, with some increasing by nearly 30%. This suggests that the cytotoxic effects decrease over time rather than worsening. It is possible that the cells adapt to the material, or that the material stabilises, reducing its initial cytotoxic impact. The data further reveals a concentration-dependent response, where higher concentrations (50 mg/mL and 100 mg/mL) generally result in lower cell viability, indicating that cytotoxic effects become more pronounced at elevated doses. Despite this, HA-Ag(30), which exhibits some cytotoxicity at the highest concentration (69% at 24 hours; 82% at 48 hours), maintains cell viability above 90% at the remaining concentrations for both 24 and 48 hours. This underscores the potential of HA-Ag(30) to strike a balance between antimicrobial efficacy and cytocompatibility.

Based on the cytotoxicity results, it can be concluded that the majority of the tested materials do not release toxic substances into the surrounding environment and exhibit minimal adverse effects on cell viability, indicating a potential for biocompatibility. However, additional tests, including *in vivo* studies, are required to confirm complete biocompatibility.

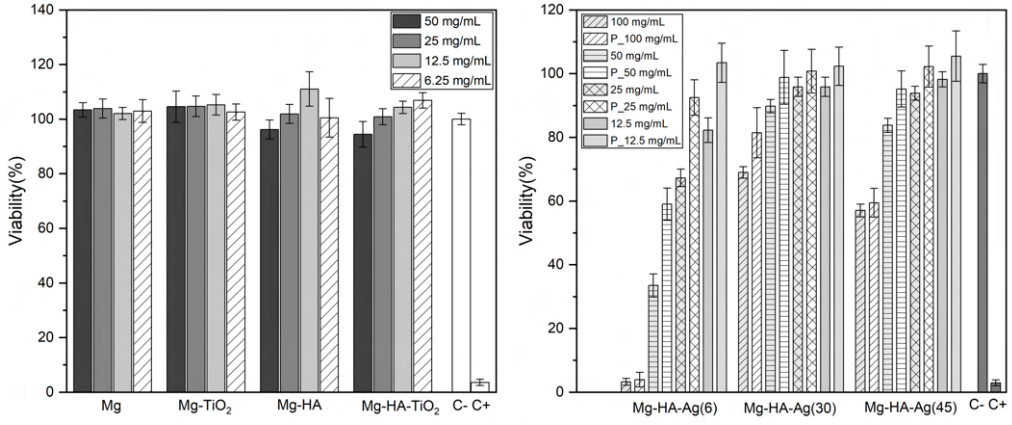

Figure 5.18: Cell viability of Mg alloy AZ61 samples: (Left) Uncoated, HA(B), TiO_2, and HA-TiO_2-coated samples after 24 hours. (Right) HA-Ag-coated samples (coated for 6, 30, and 45 minutes) after 24 and 48 hours.

6

Conclusion and Future Work

In conclusion, the Mg samples were successfully produced using the WAAM technique and four different coatings were applied to their surface with the electrodeposition technique: HA, TiO_2, a combination of HA and TiO_2, and a combination of HA and Ag. The HA and TiO_2 coatings were based on prior research, while the combined coatings were developed from this foundation. Through systematic testing of various deposition protocols, optimal conditions were identified for each coating type. Protocol B proved superior for HA deposition, while the optimal HA and TiO_2 combination was achieved at 1 V for 45 minutes. For HA and Ag, the best results were obtained using a low-concentration electrolyte and a deposition time of 30 minutes.

Following optimisation, the selected coatings underwent electrochemical and degradation analyses to compare their performance and determine which coating demonstrated the best overall results. The coatings exhibited excellent corrosion resistance in neutral pH, particularly the HA-TiO_2 coating, which, with the least negative OCP, lowest I_{corr}, greatest R_p, and highest $|Z|$ at low frequencies, provided the best protection for the Mg alloy. In addition, HA-Ag also demonstrated remarkable results, confirming the effectiveness of the double coatings in this environment.

However, in acidic conditions, the conclusions were less straightforward. The HA-Ag coating exhibited the most effective corrosion resistance in two of the tests, OCP and EIS, but yielded the poorest results in the PR test. In contrast, the HA coating (Protocol A) demonstrated consistency across all three tests, achieving the best results in PR and the second-best outcome in OCP and EIS. This consistency made HA (Protocol A) the best overall option under acidic conditions, despite not excelling in individual tests as much as HA-Ag. Although the goal of improving corrosion resistance was achieved, further optimisation under acidic conditions is necessary.

Cytocompatibility testing further validated the potential of these coatings, with only the Ag-containing samples showing any signs of cytotoxicity. Nonetheless, the HA-Ag coating with a 30-minute deposition still produced promising results.

Overall, the project successfully identified the optimal coating conditions and confirmed the coatings' ability to enhance corrosion resistance and cytocompatibility of the

Mg alloy AZ61. However, further research is needed to assess the antibacterial properties of these combined coatings. Given that HA is a bioactive material with a rough surface, it could promote cell adhesion to the implant surface and support bone tissue proliferation due to its bioactivity. Therefore, in addition to antibacterial tests, it would be highly beneficial to analyse cellular proliferation and bone tissue regeneration. Furthermore, studying the relationship between the degradation rate of the implant and the rate of bone tissue regeneration could provide valuable insights into optimising the performance of these coatings in clinical applications.

These crucial steps will help ensure that the coatings not only provide superior corrosion protection but also deliver effective antimicrobial action and bioactivity, fully realising their potential for use in Mg-based temporary implants.

Bibliography

[1] J. M. Lourenço. *The NOVAthesis LaTeX Template User's Manual*. NOVA University Lisbon. 2021. URL: https://github.com/joaomlourenco/novathesis/raw/main/template.pdf (cit. on p. i).

[2] A.-M. Wu et al. "Global, regional, and national burden of bone fractures in 204 countries and territories, 1990–2019: a systematic analysis from the Global Burden of Disease Study 2019". In: *The Lancet Healthy Longevity* 2.9 (2021), e580–e592. DOI: https://doi.org/10.1016/S2666-7568(21)00172-0 (cit. on p. 1).

[3] M. Lindstrom et al. "Global burden of cardiovascular diseases and risks collaboration, 1990-2021". In: *Journal of the American College of Cardiology* 80.25 (2022), pp. 2372–2425. DOI: https://doi.org/10.1016/j.jacc.2022.11.001 (cit. on p. 1).

[4] A. Goharian and M. Abdullah. "Bioinert metals (stainless steel, titanium, cobalt chromium)". In: *Trauma plating systems* 115 (2017) (cit. on p. 1).

[5] S. Kamrani and C. Fleck. "Biodegradable magnesium alloys as temporary orthopaedic implants: a review". In: *Biometals* 32 (2019), pp. 185–193. DOI: https://doi.org/10.1007/s10534-019-00170-y (cit. on pp. 1, 2, 6, 7).

[6] H. S. Brar et al. "Magnesium as a biodegradable and bioabsorbable material for medical implants". In: *Jom* 61 (2009), pp. 31–34. DOI: https://doi.org/10.1007/s11837-009-0129-0 (cit. on pp. 2, 6, 7).

[7] A. Haider et al. "Recent advances in the synthesis, functionalization and biomedical applications of hydroxyapatite: a review". In: *Rsc Advances* 7.13 (2017), pp. 7442–7458. DOI: https://doi.org/10.1039/C6RA26124H (cit. on pp. 2, 8).

[8] S. Zaman et al. "Overview of hydroxyapatite; composition, structure, synthesis methods and its biomedical uses". In: *Biomedical Letters* 6.1 (2020), pp. 84–99 (cit. on pp. 2, 7, 8).

[9] D. Zhang et al. "Advances in antibacterial functionalized coatings on Mg and its alloys for medical use—A review". In: *Coatings* 10.9 (2020), p. 828. DOI: https://doi.org/10.3390/coatings10090828 (cit. on pp. 2, 9).

[10] Z. Lin, X. Sun, and H. Yang. "The role of antibacterial metallic elements in simultaneously improving the corrosion resistance and antibacterial activity of magnesium alloys". In: *Materials & Design* 198 (2021), p. 109350. DOI: https://doi.org/10.1016/j.matdes.2020.109350 (cit. on pp. 2, 9).

[11] Y. Shao et al. "Advance in antibacterial magnesium alloys and surface coatings on magnesium alloys: a review". In: *Acta Metallurgica Sinica (English Letters)* 33 (2020), pp. 615–629. DOI: https://doi.org/10.1007/s40195-020-01044-w (cit. on pp. 2, 6, 10).

[12] R. Allavikutty et al. "Additive manufacturing of Mg alloys for biomedical applications: Current status and challenges". In: *Current Opinion in Biomedical Engineering* 18 (2021), p. 100276. DOI: https://doi.org/10.1016/j.cobme.2021.100276 (cit. on p. 2).

[13] G. Rasiya, A. Shukla, and K. Saran. "Additive manufacturing-a review". In: *Materials Today: Proceedings* 47 (2021), pp. 6896–6901. DOI: https://doi.org/10.1016/j.matpr.2021.05.181 (cit. on p. 5).

[14] M. Salmi. "Additive manufacturing processes in medical applications". In: *Materials* 14.1 (2021), p. 191. DOI: https://doi.org/10.3390/ma14010191 (cit. on p. 5).

[15] J. Z. Li et al. "Review of wire arc additive manufacturing for 3D metal printing". In: *International Journal of Automation Technology* 13.3 (2019), pp. 346–353. DOI: https://doi.org/10.20965/ijat.2019.p0346 (cit. on p. 5).

[16] R. Karunakaran et al. "Additive manufacturing of magnesium alloys". In: *Bioactive materials* 5.1 (2020), pp. 44–54. DOI: https://doi.org/10.1016/j.bioactmat.2019.12.004 (cit. on p. 5).

[17] T. A. Rodrigues et al. "Current status and perspectives on wire and arc additive manufacturing (WAAM)". In: *Materials* 12.7 (2019), p. 1121. DOI: https://doi.org/10.3390/ma12071121 (cit. on p. 5).

[18] S. S. Sharifi et al. "Selection of Parameters for Optimized WAAM Structures for Civil Engineering Applications". In: *Materials* 16.13 (2023), p. 4862. DOI: https://doi.org/10.3390/ma16134862 (cit. on p. 6).

[19] W. Jahnen-Dechent and M. Ketteler. "Magnesium basics". In: *Clinical kidney journal* 5.Suppl_1 (2012), pp. i3–i14. DOI: https://doi.org/10.1093/ndtplus/sfr163 (cit. on p. 6).

[20] C. Niranjan et al. "Magnesium alloys as extremely promising alternatives for temporary orthopedic implants–A review". In: *Journal of Magnesium and Alloys* (2023). DOI: https://doi.org/10.1016/j.jma.2023.08.002 (cit. on p. 6).

[21] W.-D. Mueller, M. L. Nascimento, and M. F. L. De Mele. "Critical discussion of the results from different corrosion studies of Mg and Mg alloys for biomaterial applications". In: *Acta biomaterialia* 6.5 (2010), pp. 1749–1755. DOI: https://doi.org/10.1016/j.actbio.2009.12.048 (cit. on pp. 6, 7).

[22] A. A. Pasa and M. L. Munford. "Encyclopedia of Chemical Processing". In: ed. by S. Lee. Taylor & Francis, 2006. Chap. Electrodeposition, pp. 821–832 (cit. on p. 7).

[23] A. Tarditi, M. Bosko, and L. Cornaglia. "Electroless plating of Pd binary and ternary alloys and surface characteristics for application in hydrogen separation". In: (2017) (cit. on pp. 7, 8).

[24] D. Gomes et al. "A brief review on hydroxyapatite production and use in biomedicine". In: *Cerâmica* 65.374 (2019), pp. 282–302. DOI: https://doi.org/10.1590/0366-69132019653742706 (cit. on p. 8).

[25] J. Chen et al. "Recent advances on development of hydroxyapatite coating on biodegradable magnesium alloys: a review". In: *Materials* 14.19 (2021), p. 5550. DOI: https://doi.org/10.3390/ma14195550 (cit. on p. 8).

[26] M. Jamesh, S. Kumar, and T. Sankara Narayanan. "Electrodeposition of hydroxyapatite coating on magnesium for biomedical applications". In: *Journal of Coatings Technology and Research* 9 (2012), pp. 495–502. DOI: https://doi.org/10.1007/s11998-011-9382-6 (cit. on pp. 8, 12, 24).

[27] Z. Guo et al. "Advances and challenges in metallic nanomaterial synthesis and antibacterial applications". In: *Journal of Materials Chemistry B* 8.22 (2020), pp. 4764–4777. DOI: https://doi.org/10.1039/D0TB00099J (cit. on p. 9).

[28] R. Rawashdeh and Y. Haik. "Antibacterial mechanisms of metallic nanoparticles: a review". In: *Dynamic biochemistry, process biotechnology and molecular biology* 3.2 (2009), pp. 12–20 (cit. on p. 9).

[29] F. Amaro et al. "Metallic nanoparticles—friends or foes in the battle against antibiotic-resistant bacteria?" In: *Microorganisms* 9.2 (2021), p. 364. DOI: https://doi.org/10.3390/microorganisms9020364 (cit. on p. 9).

[30] J. M. V. Makabenta et al. "Nanomaterial-based therapeutics for antibiotic-resistant bacterial infections". In: *Nature Reviews Microbiology* 19.1 (2021), pp. 23–36. DOI: https://doi.org/10.1038/s41579-020-0420-1 (cit. on p. 9).

[31] G. V. Vimbela et al. "Antibacterial properties and toxicity from metallic nanomaterials". In: *International journal of nanomedicine* (2017), pp. 3941–3965. DOI: https://doi.org/10.2147/IJN.S134526 (cit. on p. 10).

[32] H. Haugen and S. Lyngstadaas. "Antibacterial effects of titanium dioxide in wounds". In: *Wound healing biomaterials*. Elsevier, 2016, pp. 439–450. DOI: https://doi.org/10.1016/B978-1-78242-456-7.00021-0 (cit. on p. 10).

[33] M. Azizi-Lalabadi et al. "Antimicrobial activity of Titanium dioxide and Zinc oxide nanoparticles supported in 4A zeolite and evaluation the morphological characteristic". In: *Scientific reports* 9.1 (2019), p. 17439. DOI: https://doi.org/10.1038/s41598-019-54025-0 (cit. on p. 10).

[34] A. Shubhasri et al. "Fabrication of biogenic titanium nanoparticles and investigating their biological properties for dental applications". In: *Cureus* 15.8 (2023). DOI: https://doi.org/10.7759%2Fcureus.44209 (cit. on p. 10).

[35] J. Guo et al. "Wire arc additive manufacturing of AZ31 magnesium alloy: Grain refinement by adjusting pulse frequency". In: *Materials* 9.10 (2016), p. 823. DOI: https://doi.org/10.3390/ma9100823 (cit. on p. 11).

[36] H. Takagi et al. "Material-property evaluation of magnesium alloys fabricated using wire-and-arc-based additive manufacturing". In: *Additive Manufacturing* 24 (2018), pp. 498–507. DOI: https://doi.org/10.1016/j.addma.2018.10.026 (cit. on p. 11).

[37] T. Ying et al. "Effect of fabrication parameters on the microstructure and mechanical properties of wire arc additive manufactured AZ61 alloy". In: *Materials Letters* 307 (2022), p. 131014. DOI: https://doi.org/10.1016/j.matlet.2021.131014 (cit. on p. 11).

[38] Y. Guo et al. "Microstructure and mechanical properties of wire arc additively manufactured AZ80M magnesium alloy". In: *Materials Letters* 247 (2019), pp. 4–6. DOI: https://doi.org/10.1016/j.matlet.2019.03.063 (cit. on p. 11).

[39] Y. Guo et al. "Effect of heat treatment on the microstructure and mechanical properties of AZ80M magnesium alloy fabricated by wire arc additive manufacturing". In: *Journal of magnesium and alloys* 10.7 (2022), pp. 1930–1940. DOI: https://doi.org/10.1016/j.jma.2021.04.006 (cit. on p. 11).

[40] T. Klein et al. "Microstructure formation and mechanical properties of a wire-arc additive manufactured magnesium alloy". In: *Jom* 73 (2021), pp. 1126–1134. DOI: https://doi.org/10.1007/s11837-021-04567-4 (cit. on p. 11).

[41] P. Wang et al. "Wire-arc additive manufacturing of AZ31 magnesium alloy fabricated by cold metal transfer heat source: Processing, microstructure, and mechanical behavior". In: *Journal of Materials Processing Technology* 288 (2021), p. 116895. DOI: https://doi.org/10.1016/j.jmatprotec.2020.116895 (cit. on p. 12).

[42] C. Yin et al. "Microstructure and mechanical properties of AZ91 magnesium alloy fabricated by multi-layer and multi-pass CMT based WAAM technique". In: *Results in Engineering* 18 (2023), p. 101065. DOI: https://doi.org/10.1016/j.rineng.2023.101065 (cit. on p. 12).

[43] Y. Song, D. Shan, and E. Han. "Electrodeposition of hydroxyapatite coating on AZ91D magnesium alloy for biomaterial application". In: *Materials letters* 62.17-18 (2008), pp. 3276–3279. DOI: https://doi.org/10.1016/j.matlet.2008.02.048 (cit. on pp. 12, 23).

[44] M. Rahman, Y. Li, and C. Wen. "Realization and characterization of double-layer Ca-P coating on WE43 Mg alloy for biomedical applications". In: *Surface and Coatings Technology* 398 (2020), p. 126091. DOI: https://doi.org/10.1016/j.surfcoat.2020.126091 (cit. on p. 12).

[45] I. Š. Rončević, Z. Grubač, and M. Metikoš-Huković. "Electrodeposition of hydroxyapatite coating on AZ91D alloy for biodegradable implant application". In: *International Journal of Electrochemical Science* 9.11 (2014), pp. 5907–5923. DOI: https://doi.org/10.1016/S1452-3981(23)10858-3 (cit. on pp. 12, 17, 23).

[46] S. Salman, K. Kuroda, and M. Okido. "Preparation and characterization of hydroxyapatite coating on AZ31 Mg alloy for implant applications". In: *Bioinorganic chemistry and applications* 2013.1 (2013), p. 175756. DOI: https://doi.org/10.1155/2013/175756 (cit. on p. 12).

[47] M. Uddin, C. Hall, and V. Santos. "Fabrication, characterisation and corrosion of HA coated AZ31B Mg implant material: Effect of electrodeposition current density". In: *Surface and Coatings Technology* 385 (2020), p. 125363. DOI: https://doi.org/10.1016/j.surfcoat.2020.125363 (cit. on p. 12).

[48] P. Amaravathy et al. "Bioactive HA/TiO2 coating on magnesium alloy for biomedical applications". In: *Ceramics international* 40.5 (2014), pp. 6617–6630. DOI: https://doi.org/10.1016/j.ceramint.2013.11.119 (cit. on pp. 13, 26, 28, 29).

[49] Y. Guo et al. "Hydroxyapatite/titania composite coatings on biodegradable magnesium alloy for enhanced corrosion resistance, cytocompatibility and antibacterial properties". In: *Journal of The Electrochemical Society* 165.14 (2018), p. C962. DOI: 10.1149/2.1171814jes (cit. on p. 13).

[50] M. Amirnejad, A. Afshar, and S. Salehi. "The effect of titanium dioxide (TiO2) nanoparticles on hydroxyapatite (HA)/TiO 2 composite coating fabricated by electrophoretic deposition (EPD)". In: *Journal of Materials Engineering and Performance* 27 (2018), pp. 2338–2344. DOI: https://doi.org/10.1007/s11665-018-3342-6 (cit. on p. 13).

[51] C. Fu et al. "Antimicrobial silver-hydroxyapatite composite coatings through two-stage electrochemical synthesis". In: *Surface and Coatings Technology* 301 (2016), pp. 13–19. DOI: https://doi.org/10.1016/j.surfcoat.2016.03.010 (cit. on pp. 13, 18).

[52] M. Mirzaee, M. Vaezi, and Y. Palizdar. "Synthesis and characterization of silver doped hydroxyapatite nanocomposite coatings and evaluation of their antibacterial and corrosion resistance properties in simulated body fluid". In: *Materials Science and Engineering: C* 69 (2016), pp. 675–684. DOI: https://doi.org/10.1016/j.msec.2016.07.057 (cit. on pp. 13, 18, 32).

[53] T. Mokabber et al. "Antimicrobial electrodeposited silver-containing calcium phosphate coatings". In: *ACS applied materials & interfaces* 12.5 (2020), pp. 5531–5541. DOI: https://doi.org/10.1021/acsami.9b20158 (cit. on pp. 13, 18).

[54] X. Lu et al. "Nano-Ag-loaded hydroxyapatite coatings on titanium surfaces by electrochemical deposition". In: *Journal of the Royal Society Interface* 8.57 (2011), pp. 529–539. DOI: https://doi.org/10.1098/rsif.2010.0366 (cit. on p. 13).

[55] J. L. F. S. M. Ribeiro. "Development of resorbable metal-based biomedical implants". MA thesis. School of Science and Technology, NOVA University of Lisbon, 2022 (cit. on pp. 15, 17, 23).

[56] M. B. Kannan and L. Orr. "In vitro mechanical integrity of hydroxyapatite coated magnesium alloy". In: *Biomedical Materials* 6.4 (2011), p. 045003. DOI: https://dx.doi.org/10.1088/1748-6041/6/4/045003 (cit. on p. 17).

[57] B. M. P. Passarinho. "Surface Functionalization of Resorbable Biomedical Implants with Metallic Oxides". MA thesis. School of Science and Technology, NOVA University of Lisbon, 2024 (cit. on pp. 17, 25).

[58] X. Pang and I. Zhitomirsky. "Electrodeposition of hydroxyapatite–silver–chitosan nanocomposite coatings". In: *Surface and Coatings Technology* 202.16 (2008), pp. 3815–3821. DOI: https://doi.org/10.1016/j.surfcoat.2008.01.022 (cit. on pp. 18, 37).

[59] Y. Ouyang et al. "Electrodeposition of F-doped hydroxyapatite-TiO2 coating on AZ31 magnesium alloy for enhancing corrosion protection and biocompatibility". In: *Journal of Materials Science* 57.36 (2022), pp. 17188–17202. DOI: https://doi.org/10.1007/s10853-022-07732-5 (cit. on p. 20).

[60] Z. Zhang et al. "Microstructure and mechanical properties of weaving wire and arc additive manufactured AZ91 magnesium alloy based on cold metal transfer technique". In: *Materials* 16.11 (2023), p. 4047. DOI: https://doi.org/10.3390/ma16114047 (cit. on p. 21).

[61] X. Yang et al. "Microstructure and mechanical properties of wire and arc additive manufactured AZ31 magnesium alloy using cold metal transfer process". In: *Materials Science and Engineering: A* 774 (2020), p. 138942. DOI: https://doi.org/10.1016/j.msea.2020.138942 (cit. on p. 21).

[62] M. Assadian et al. "Topography, wetting, and corrosion responses of electrodeposited hydroxyapatite and fluoridated hydroxyapatite on magnesium". In: *Bio-Medical Materials and Engineering* 27.2-3 (2016), pp. 287–303. DOI: 10.3233/BME-161585 (cit. on pp. 22, 24).

[63] V. Uskoković and D. P. Uskoković. "Nanosized hydroxyapatite and other calcium phosphates: chemistry of formation and application as drug and gene delivery agents". In: *Journal of biomedical materials research Part B: Applied biomaterials* 96.1 (2011), pp. 152–191. DOI: https://doi.org/10.1002/jbm.b.31746 (cit. on pp. 23, 28, 31).

[64] L. Gritsch et al. "Chitosan/hydroxyapatite composite bone tissue engineering scaffolds with dual and decoupled therapeutic ion delivery: Copper and strontium". In: *Journal of Materials Chemistry B* 7.40 (2019), pp. 6109–6124. DOI: https://doi.org/10.1039/C9TB00897G (cit. on p. 24).

[65] M. Manoj et al. "Core–shell hydroxyapatite/Mg nanostructures: surfactant free facile synthesis, characterization and their in vitro cell viability studies against leukaemia cancer cells (K562)". In: *RSC Advances* 5.60 (2015), pp. 48705–48711. DOI: https://doi.org/10.1039/C5RA04663G (cit. on p. 24).

[66] P. Rajesh et al. "Laser surface modification of titanium substrate for pulsed laser deposition of highly adherent hydroxyapatite". In: *Journal of Materials Science: Materials in Medicine* 22 (2011), pp. 1671–1679. DOI: https://doi.org/10.1007/s10856-011-4342-3 (cit. on p. 24).

[67] H.-J. An et al. "Cationic surfactant promoted reductive electrodeposition of nanocrystalline anatase TiO2 for application to dye-sensitized solar cells". In: *Electrochimica Acta* 50.13 (2005), pp. 2713–2718. DOI: https://doi.org/10.1016/j.electacta.2004.11.017 (cit. on p. 25).

[68] Y. Sun et al. "Influence of annealing temperature of TiO2 nanotubes via hydrotermal method on Ti foil for photocatalytic degradation". In: *Digest Journal of Nanomaterials & Biostructures (DJNB)* 14.2 (2019) (cit. on p. 25).

[69] A. M. Peiró et al. "Electrochemically assisted deposition of titanium dioxide on aluminium cathodes". In: *Journal of Materials Chemistry* 12.9 (2002), pp. 2769–2773. DOI: https://doi.org/10.1039/B203922B (cit. on p. 26).

[70] X. Tang et al. "Ultraviolet irradiation assisted liquid phase deposited titanium dioxide (TiO2)-incorporated into phytic acid coating on magnesium for slowing-down biodegradation and improving osteo-compatibility". In: *Materials Science and Engineering: C* 108 (2020), p. 110487. DOI: https://doi.org/10.1016/j.msec.2019.110487 (cit. on pp. 26, 28).

[71] P. Amaravathy et al. "Evaluation of in vitro bioactivity and MG63 Oesteoblast cell response for TiO 2 coated magnesium alloys". In: *Journal of sol-gel science and technology* 64 (2012), pp. 694–703. DOI: https://doi.org/10.1007/s10971-012-2904-6 (cit. on p. 26).

[72] Y. Chen et al. "Sandwiched polydopamine (PDA) layer for titanium dioxide (TiO2) coating on magnesium to enhance corrosion protection". In: *Corrosion Science* 96 (2015), pp. 67–73. DOI: https://doi.org/10.1016/j.corsci.2015.03.020 (cit. on p. 26).

[73] S. S. R. Albeladi, M. A. Malik, and S. A. Al-thabaiti. "Facile biofabrication of silver nanoparticles using Salvia officinalis leaf extract and its catalytic activity towards Congo red dye degradation". In: *Journal of Materials Research and Technology* 9.5 (2020), pp. 10031–10044. DOI: https://doi.org/10.1016/j.jmrt.2020.06.074 (cit. on p. 31).

[74] K. Fatemeh, M. Mohammad Javad, and K. Samaneh. "The effect of silver nanoparticles on composite shear bond strength to dentin with different adhesion protocols". In: *Journal of applied oral science* 25.4 (2017), pp. 367–373. DOI: https://doi.org/10.1590/1678-7757-2016-0391 (cit. on p. 31).

[75] L. Jianwei et al. "Effect of grain refinement induced by wire and arc additive manufacture (WAAM) on the corrosion behaviors of AZ31 magnesium alloy in NaCl solution". In: *Journal of Magnesium and Alloys* 11.1 (2023), pp. 217–229. DOI: https://doi.org/10.1016/j.jma.2021.04.007 (cit. on pp. 33, 35).

[76] A. Atrens et al. "Understanding Mg corrosion in the body for biodegradable medical implants". In: *Scripta Materialia* 154 (2018), pp. 92–100. DOI: https://doi.org/10.1016/j.scriptamat.2018.05.021 (cit. on p. 34).

[77] M. Rashad et al. "Corrosion behavior of magnesium-graphene composites in sodium chloride solutions". In: *Journal of magnesium and alloys* 5.3 (2017), pp. 271–276. DOI: https://doi.org/10.1016/j.jma.2017.06.003 (cit. on p. 35).

[78] S. Feliu Jr. "Electrochemical impedance spectroscopy for the measurement of the corrosion rate of magnesium alloys: Brief review and challenges". In: *Metals* 10.6 (2020), p. 775 (cit. on p. 36).

[79] H. Bakhsheshi-Rad et al. "In vitro degradation behavior, antibacterial activity and cytotoxicity of TiO2-MAO/ZnHA composite coating on Mg alloy for orthopedic implants". In: *Surface and Coatings Technology* 334 (2018), pp. 450–460. DOI: https://doi.org/10.1016/j.surfcoat.2017.11.027 (cit. on p. 36).

[80] J. Jayaraj et al. "Composite magnesium phosphate coatings for improved corrosion resistance of magnesium AZ31 alloy". In: *Corrosion Science* 113 (2016), pp. 104–115. DOI: https://doi.org/10.1016/j.corsci.2016.10.010 (cit. on p. 37).

[81] International Organization for Standardization. *ISO 10993-5: Biological Evaluation of Medical Devices — Part 5: Tests for In Vitro Cytotoxicity*. https://www.iso.org/standard/36406.html. Accessed: 2024-07-28. 2009 (cit. on p. 39).

[82] M. Akter et al. "A systematic review on silver nanoparticles-induced cytotoxicity: Physicochemical properties and perspectives". In: *Journal of advanced research* 9 (2018), pp. 1–16. DOI: https://doi.org/10.1016/j.jare.2017.10.008 (cit. on p. 40).

A

Appendix

A.1 Materials and Methods: Complementary Figures and Images

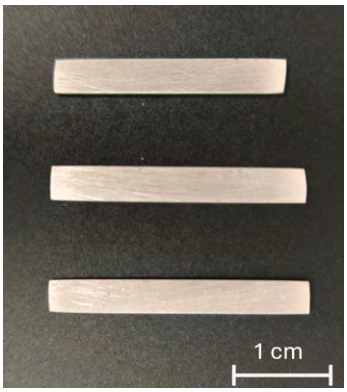

Figure A.1: Mg alloy AZ61 samples used in the study after being cut from the WAAM-produced wall, polished and cleaned.

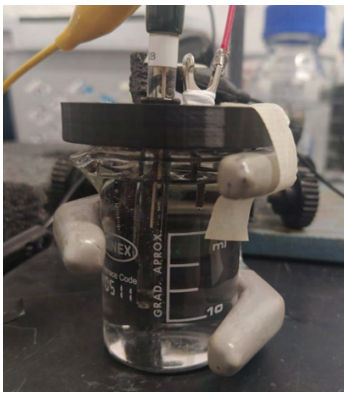

Figure A.2: Three-electrode setup for electrochemical tests. Working electrode: Mg sample; Counter electrode: graphite rod; Reference electrode: Ag/AgCl.

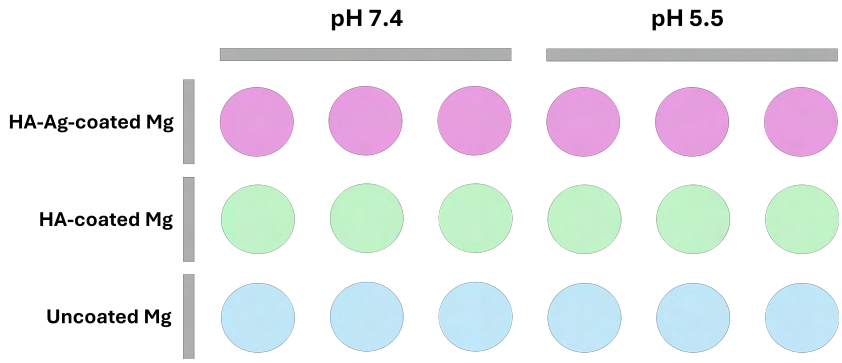

Figure A.3: Schematic representation of the setup used for the *in vitro* degradation tests.

A.2 Results and Discussion: Complementary Figures and Graphs

A.2.1 Morphological analysis

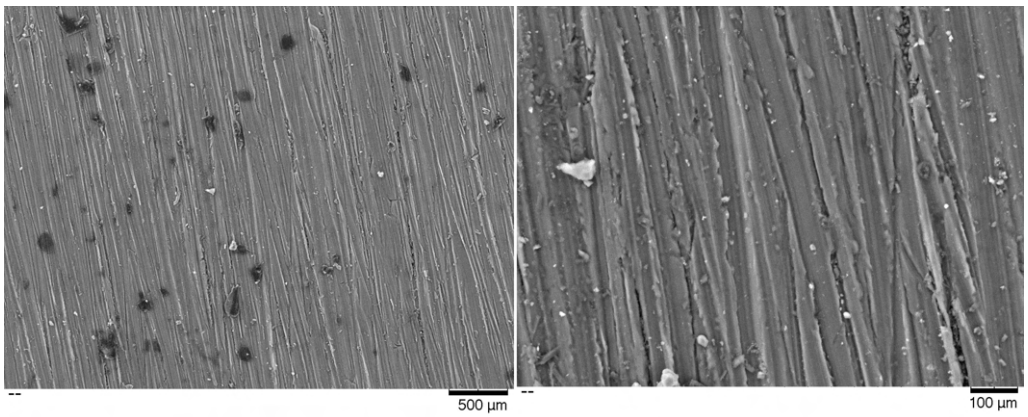

Figure A.4: SEM of the WAAM-printed Mg alloy AZ61: wide view (left) and zoomed view (right).

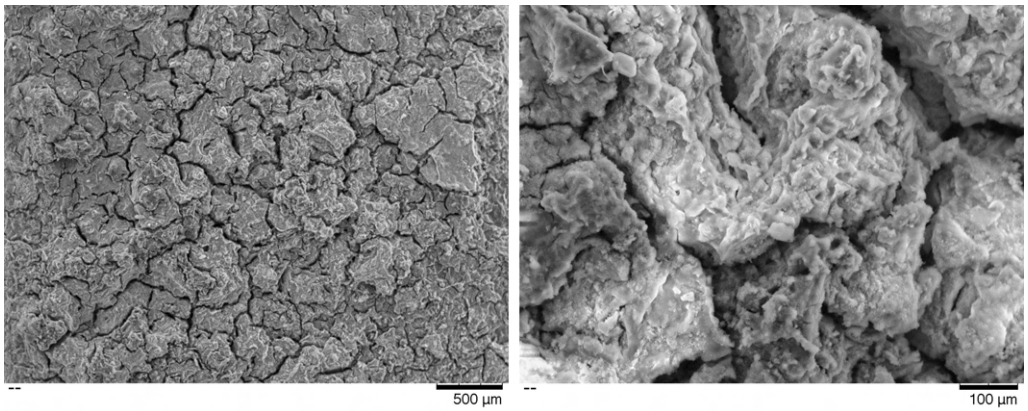

Figure A.5: SEM of HA-coated (Protocol A) Mg alloy AZ61 sample: wide view (left) and zoomed view (right).

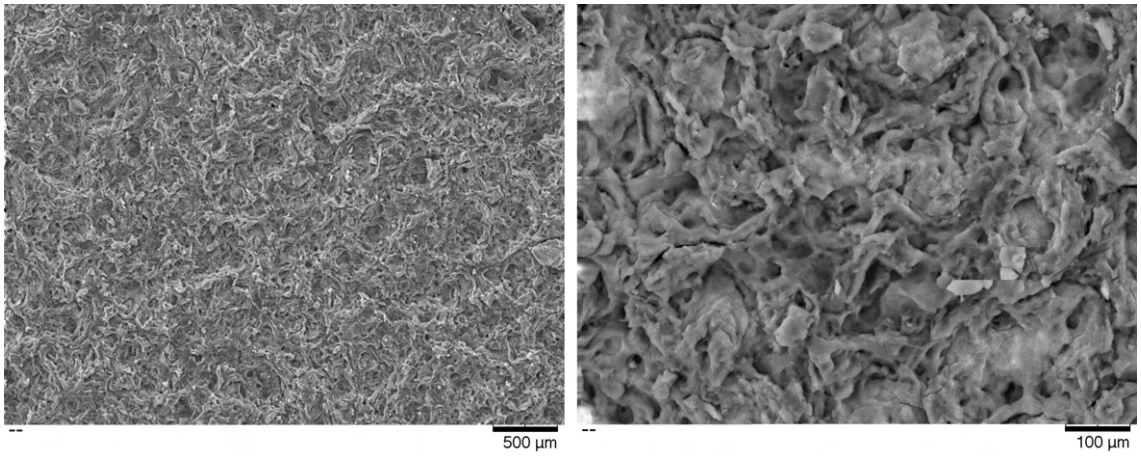

Figure A.6: SEM of HA-coated (Protocol B) Mg alloy AZ61 sample: wide view (left) and zoomed view (right).

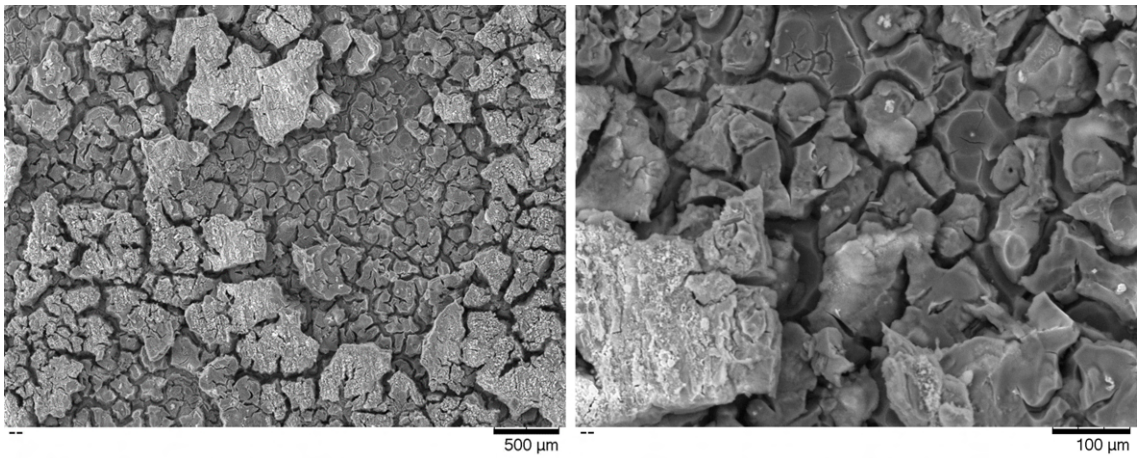

Figure A.7: SEM of TiO_2-coated Mg alloy AZ61: wide view (left) and zoomed view (right).

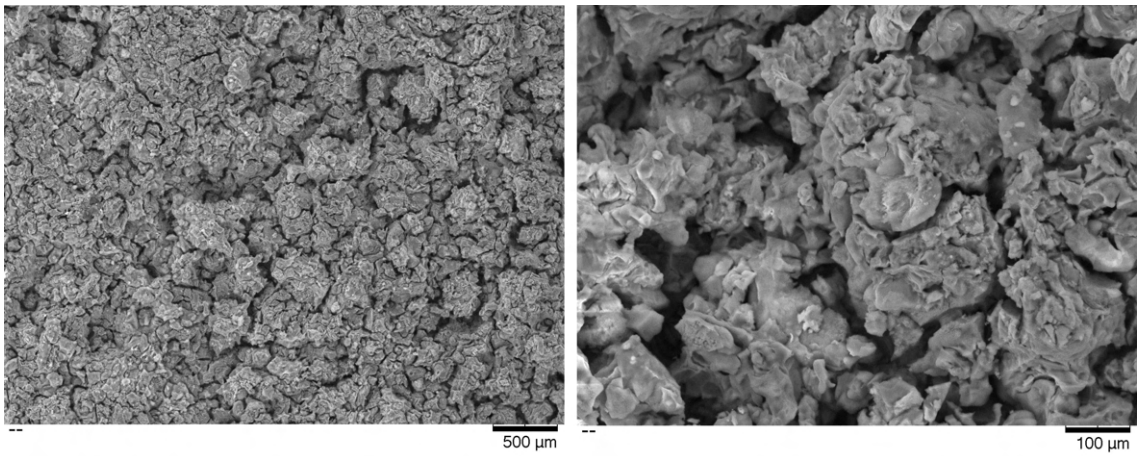

Figure A.8: SEM of HA-TiO_2-coated Mg alloy AZ61 (1 V for 45 minutes): wide view (left) and zoomed view (right).

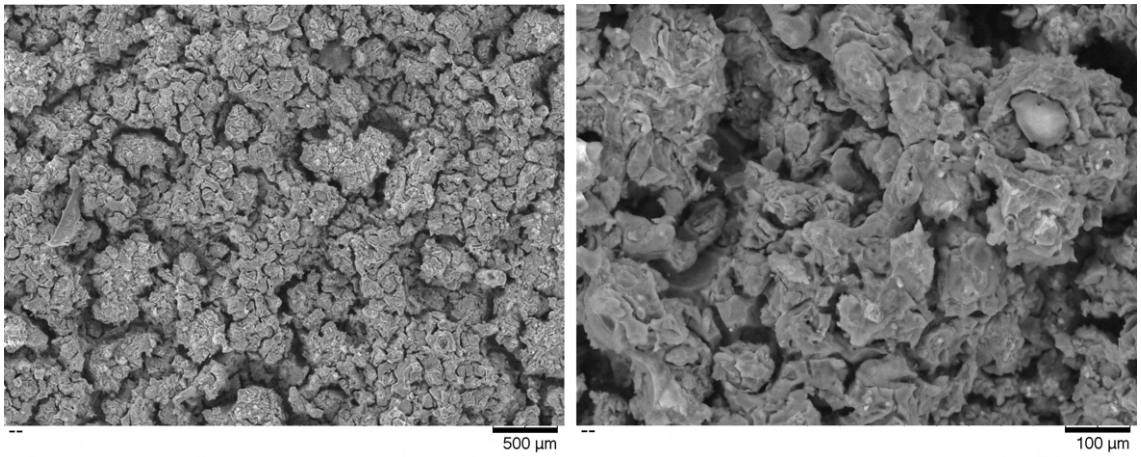

Figure A.9: SEM of HA-TiO_2-coated Mg alloy AZ61 (1 V for 60 minutes): wide view (left) and zoomed view (right).

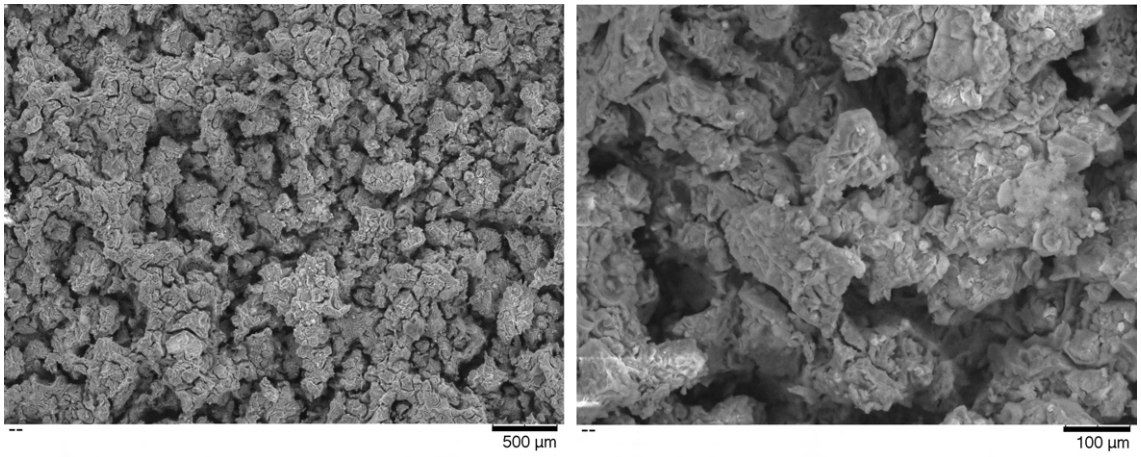

Figure A.10: SEM of HA-TiO_2-coated Mg alloy AZ61 (1.5 V for 45 minutes): wide view (left) and zoomed view (right).

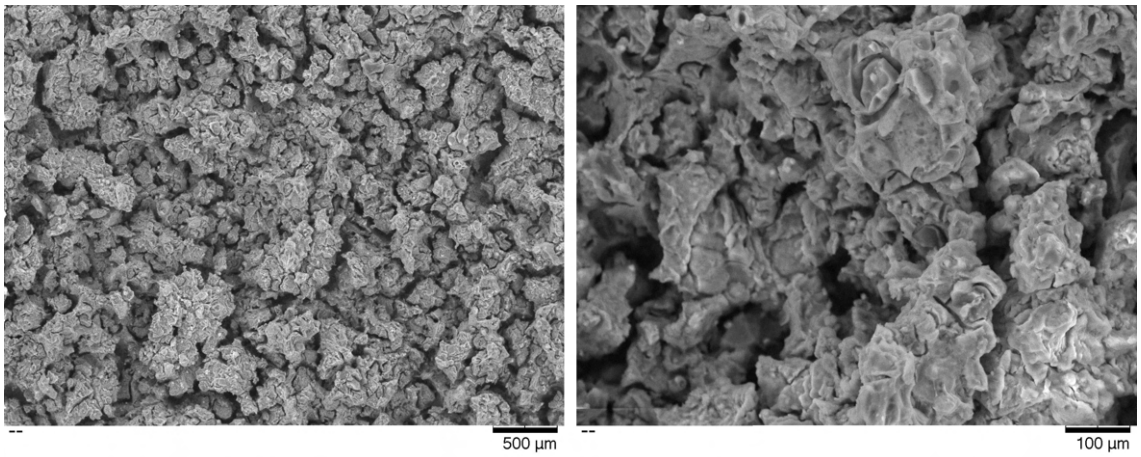

Figure A.11: SEM of HA-TiO_2-coated Mg alloy AZ61 (1.5 V for 60 minutes): wide view (left) and zoomed view (right).

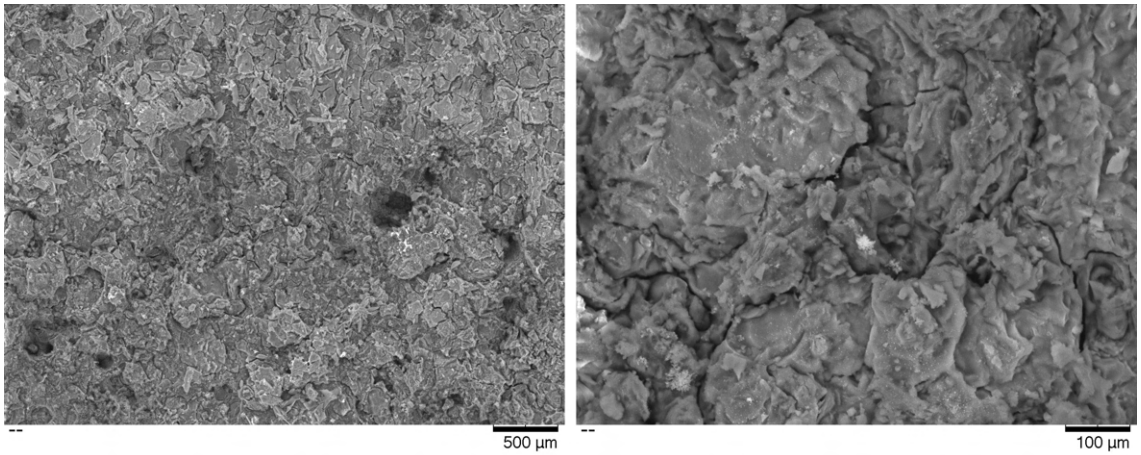

Figure A.12: SEM of HA-Ag-coated Mg alloy AZ61 (Low-concentration electrolyte for 6 minutes): wide view (left) and zoomed view (right).

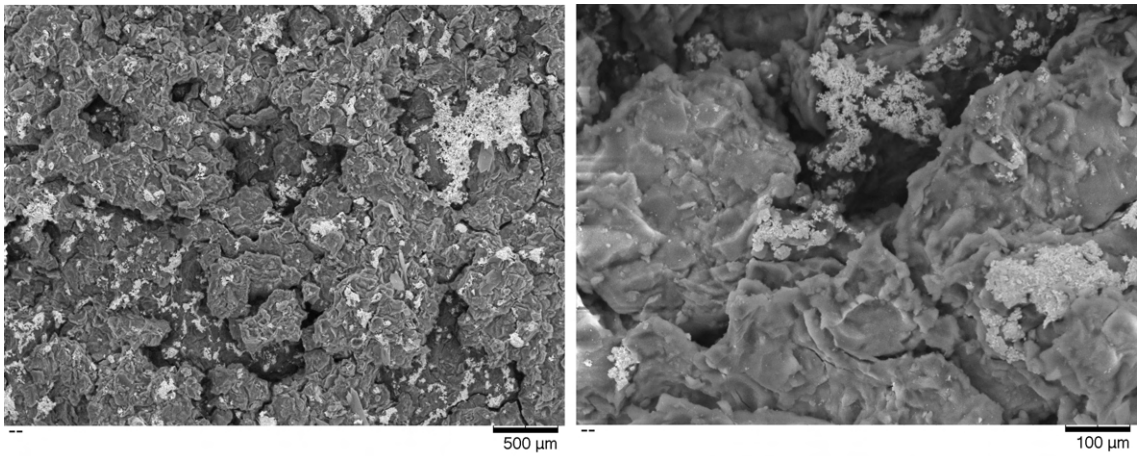

Figure A.13: SEM of HA-Ag-coated Mg alloy AZ61 (Low-concentration electrolyte for 30 minutes): wide view (left) and zoomed view (right).

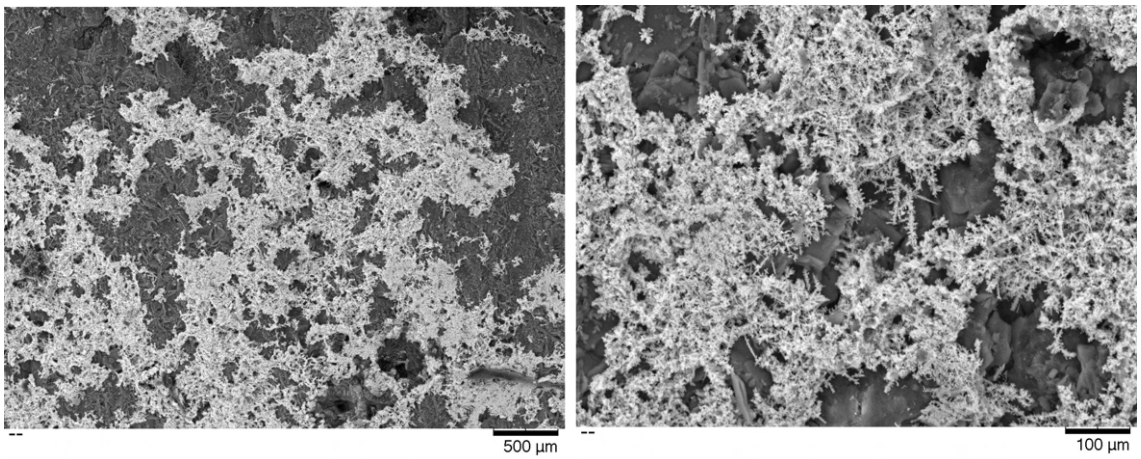

Figure A.14: SEM of HA-Ag-coated Mg alloy AZ61 (Low-concentration electrolyte for 45 minutes): wide view (left) and zoomed view (right).

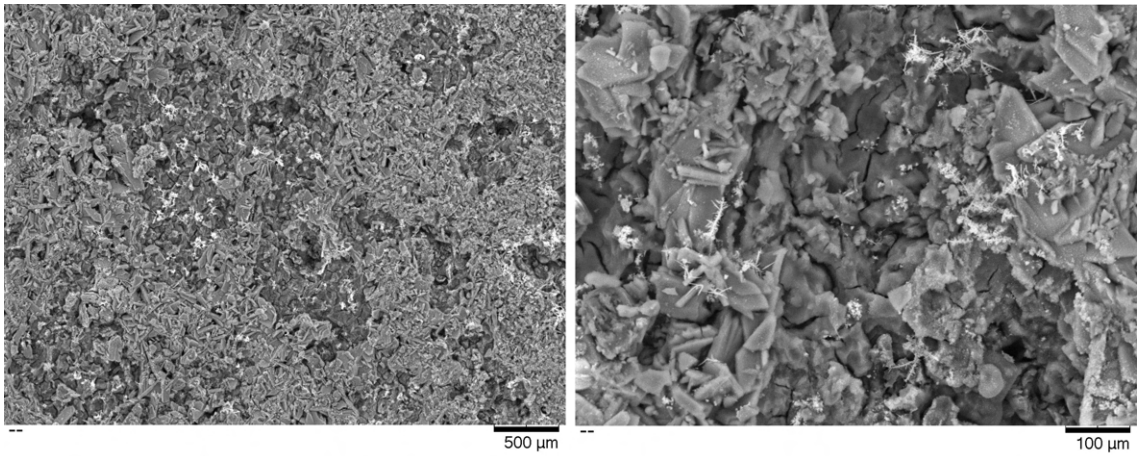

Figure A.15: SEM of HA-Ag-coated Mg alloy AZ61 (High-concentration electrolyte for 6 minutes): wide view (left) and zoomed view (right).

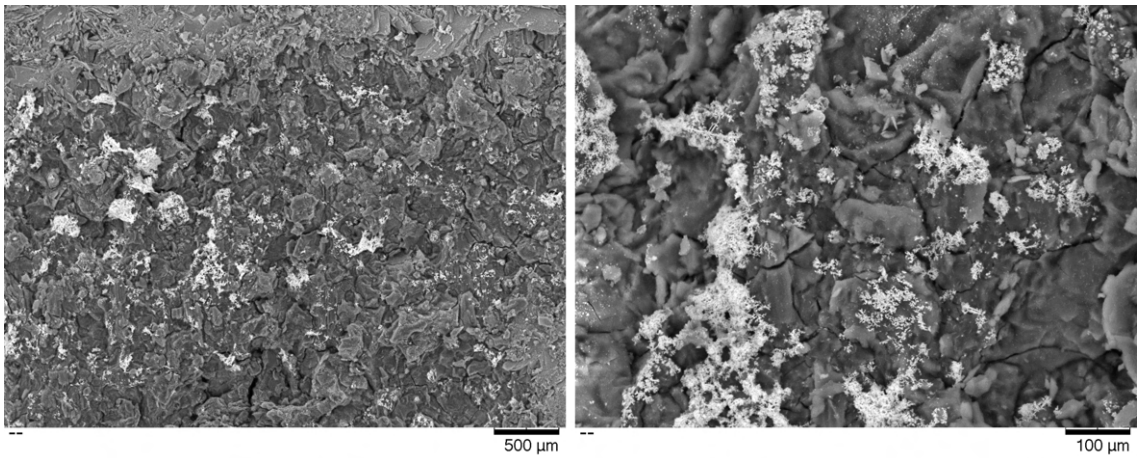

Figure A.16: SEM of HA-Ag-coated Mg alloy AZ61 (High-concentration electrolyte for 20 minutes): wide view (left) and zoomed view (right).

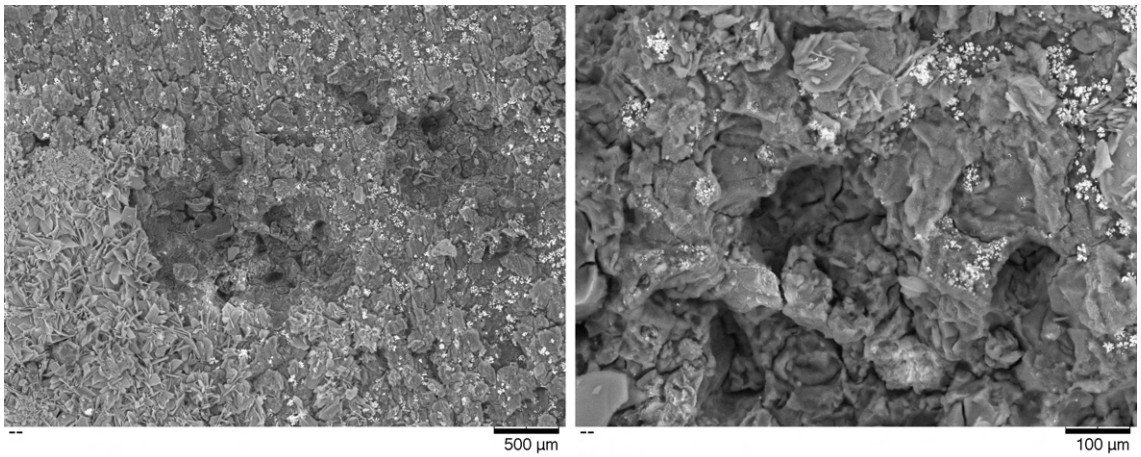

Figure A.17: SEM of HA-Ag-coated Mg alloy AZ61 (High-concentration electrolyte for 45 minutes): wide view (left) and zoomed view (right).

A.2.2 Elemental analysis

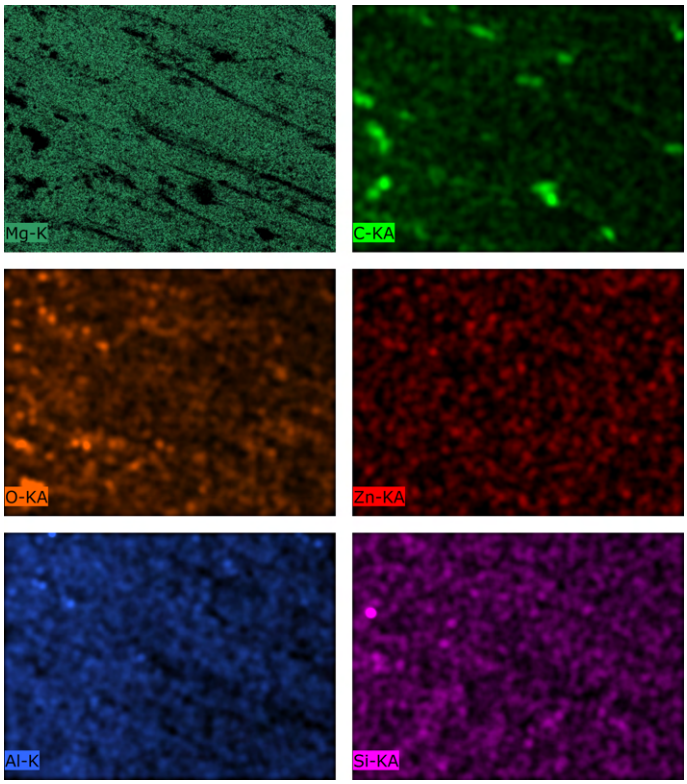

Figure A.18: EDS map of the WAAM-printed Mg alloy AZ61.

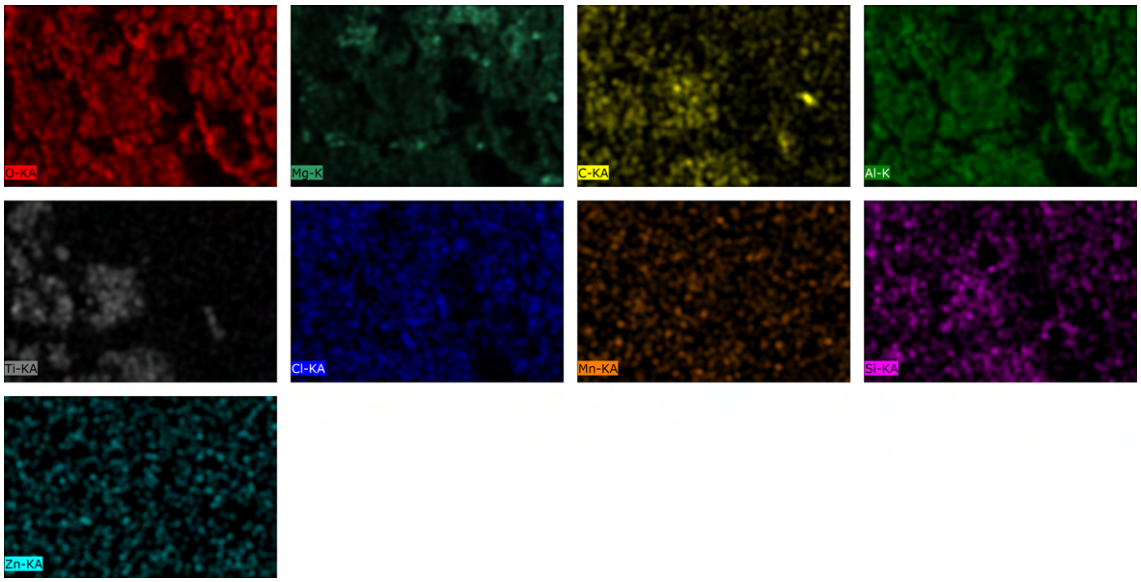

Figure A.19: EDS map of TiO_2-coated Mg alloy AZ61.

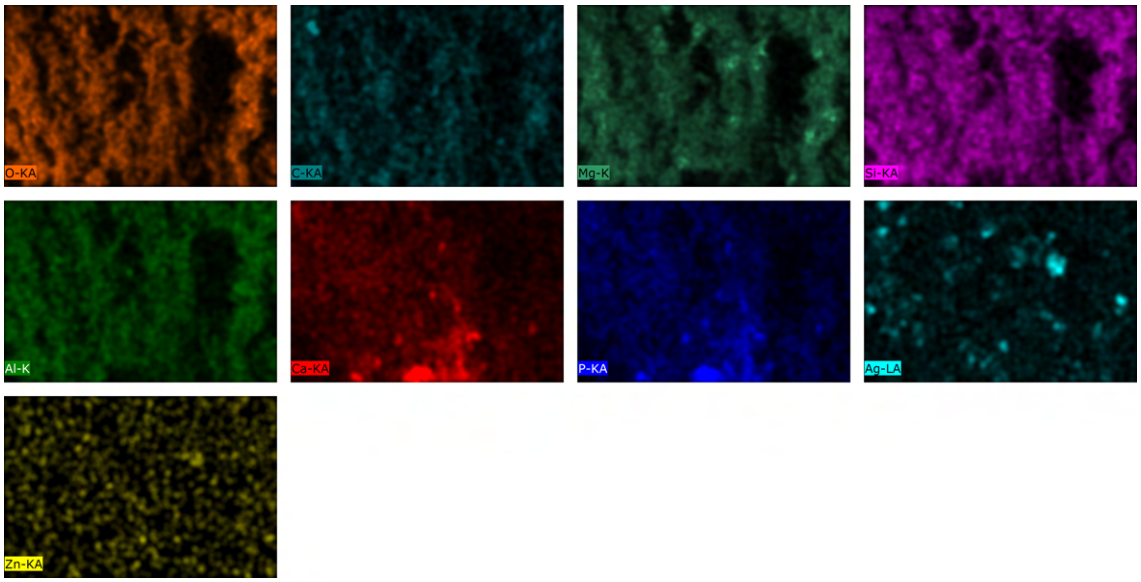

Figure A.20: EDS map of HA-Ag-coated Mg alloy AZ61 (Low-concentration electrolyte for 6 minutes).

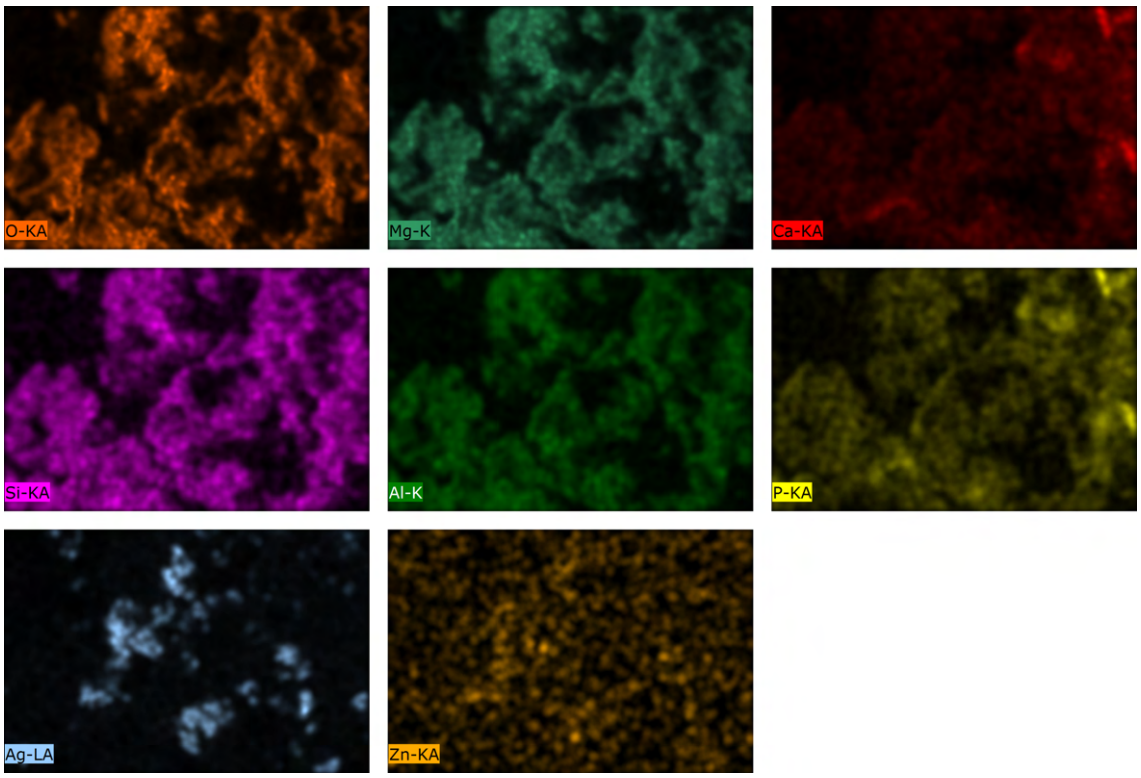

Figure A.21: EDS map of HA-Ag-coated Mg alloy AZ61 (Low-concentration electrolyte for 30 minutes).

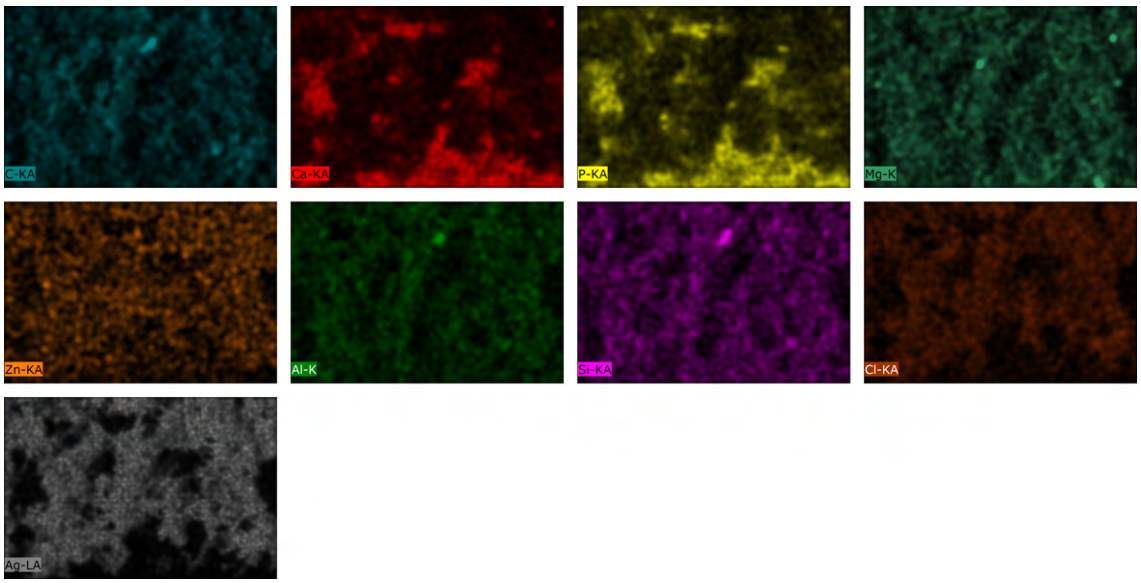

Figure A.22: EDS map of HA-Ag-coated Mg alloy AZ61 (Low-concentration electrolyte for 45 minutes).

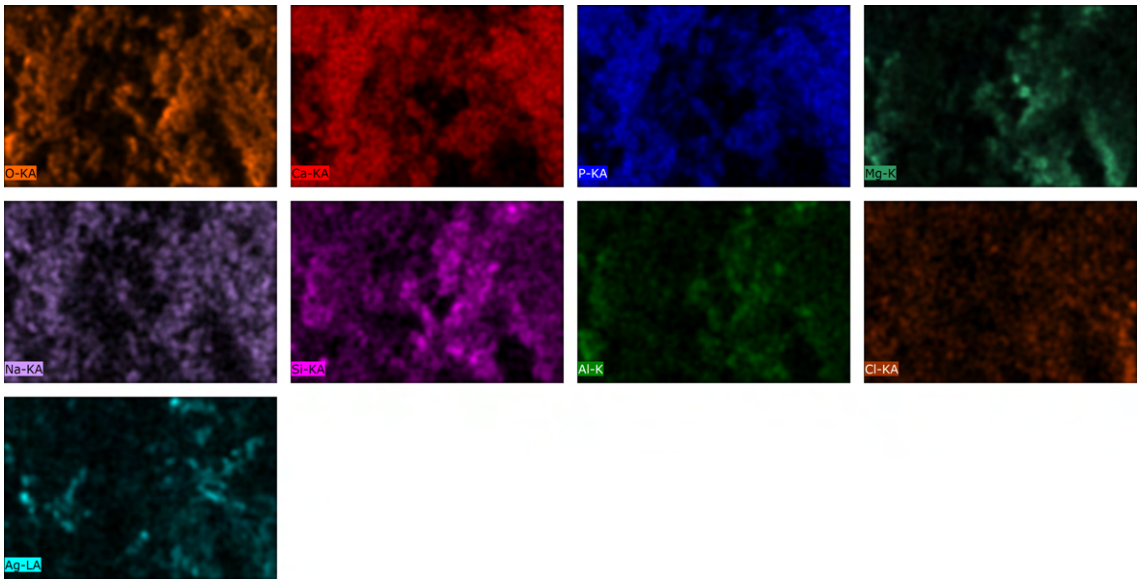

Figure A.23: EDS map of HA-Ag-coated Mg alloy AZ61 (High-concentration electrolyte for 6 minutes).

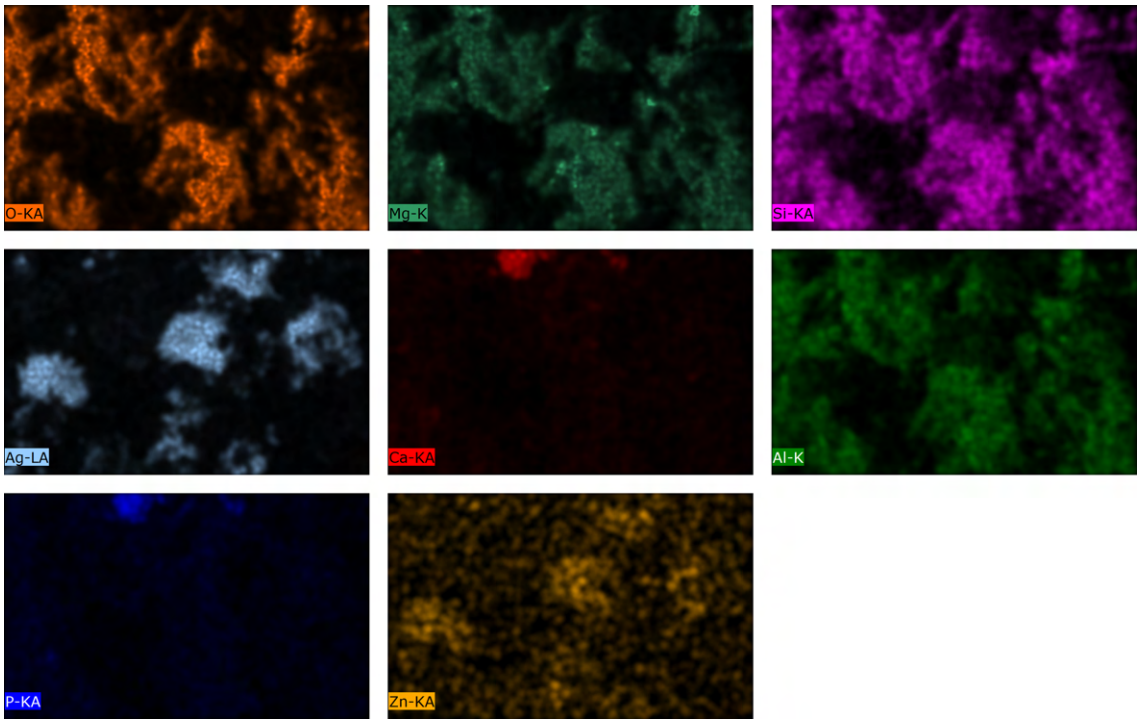

Figure A.24: EDS map of HA-Ag-coated Mg alloy AZ61 (High-concentration electrolyte for 20 minutes).

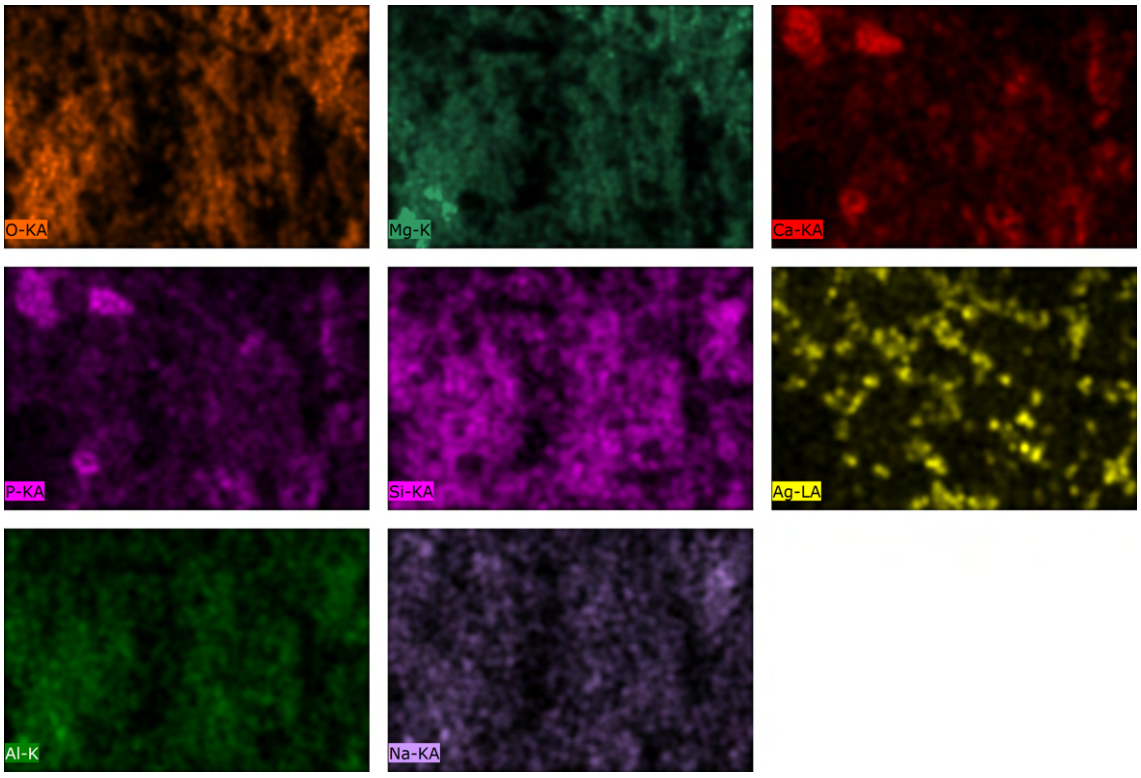

Figure A.25: EDS map of HA-Ag-coated Mg alloy AZ61 (High-concentration electrolyte for 45 minutes).

A.2.3 Structural analysis

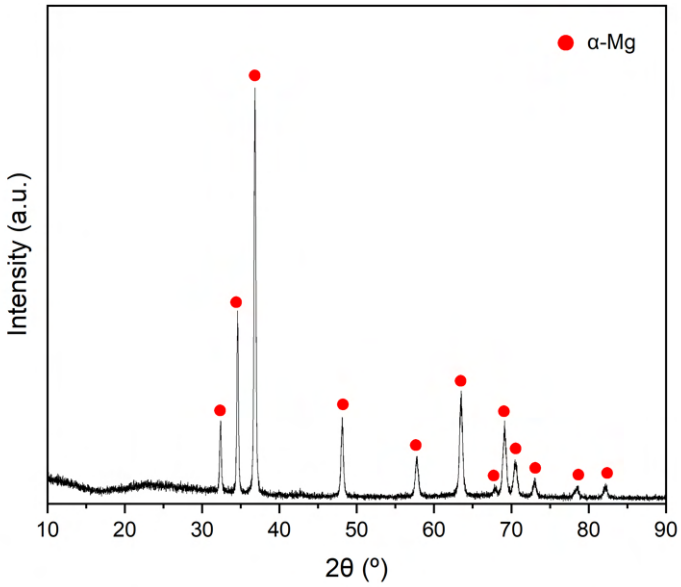

Figure A.26: XRD Analysis of WAAM-printed Mg alloy AZ61.

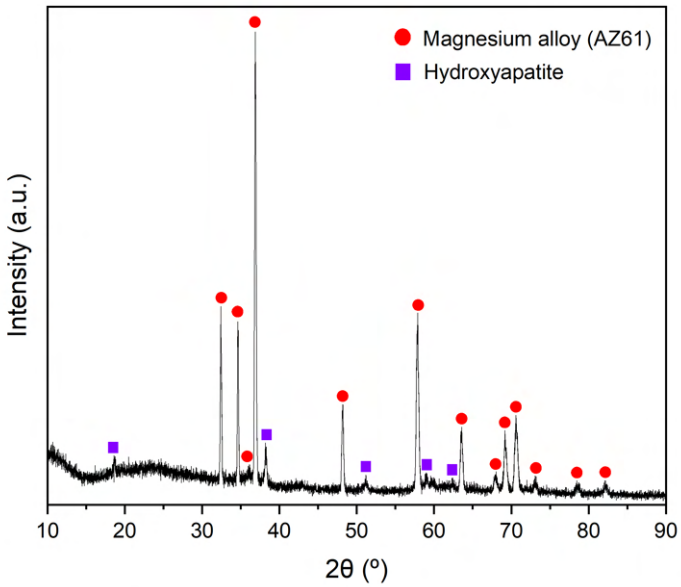

Figure A.27: XRD Analysis of HA-coated (Protocol A) Mg alloy AZ61.

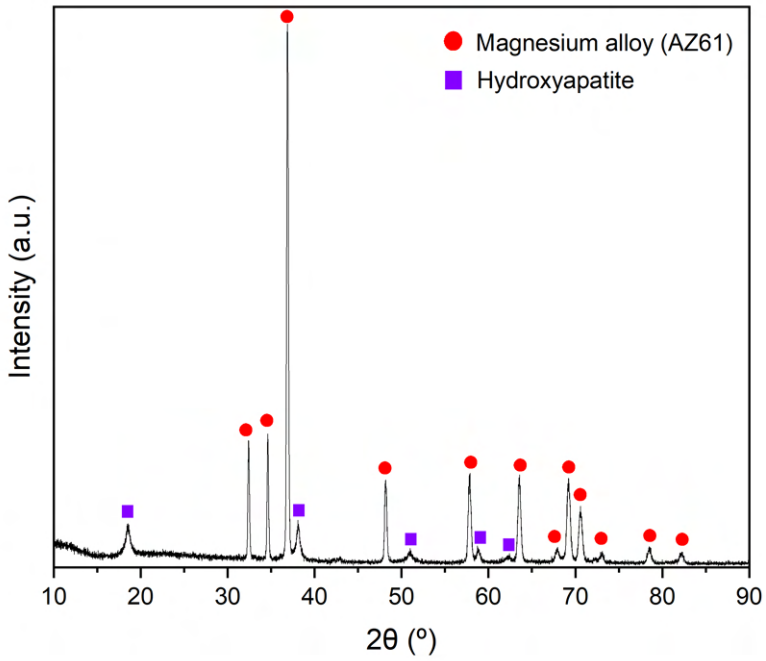

Figure A.28: XRD Analysis of HA-coated (Protocol B) Mg alloy AZ61.

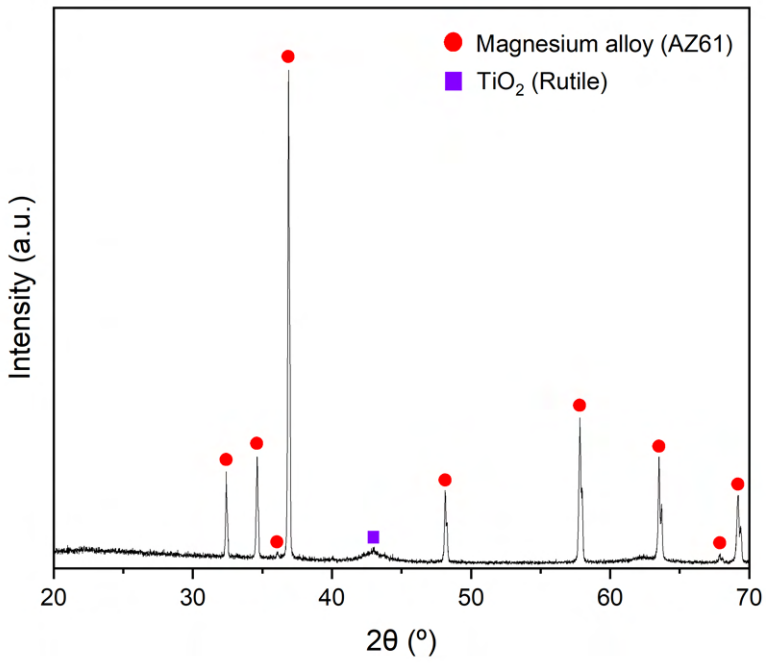

Figure A.29: XRD Analysis of TiO_2-coated Mg alloy AZ61.

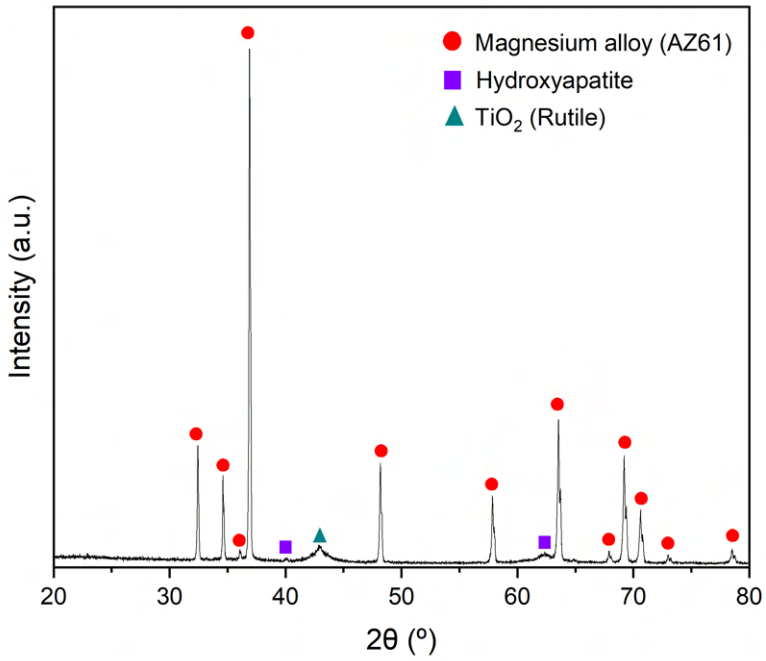

Figure A.30: XRD Analysis of HA-TiO_2-coated Mg alloy AZ61 (1 V for 45 minutes).

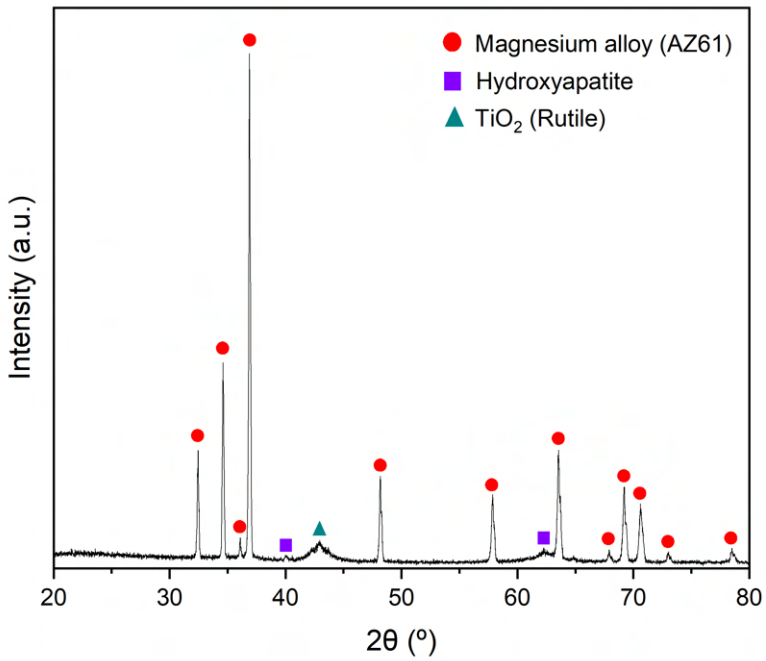

Figure A.31: XRD Analysis of HA-TiO_2-coated Mg alloy AZ61 (1 V for 60 minutes).

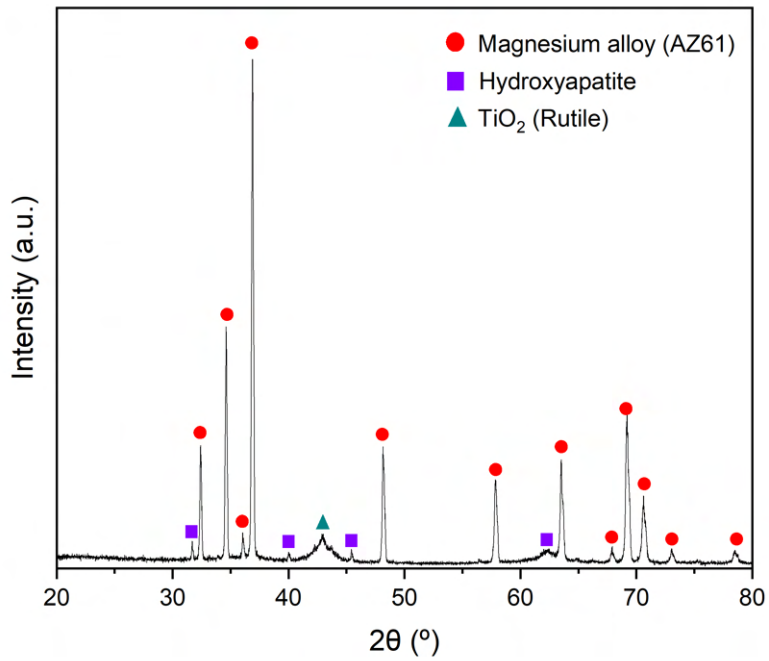

Figure A.32: XRD Analysis of HA-TiO_2-coated Mg alloy AZ61 (1.5 V for 45 minutes).

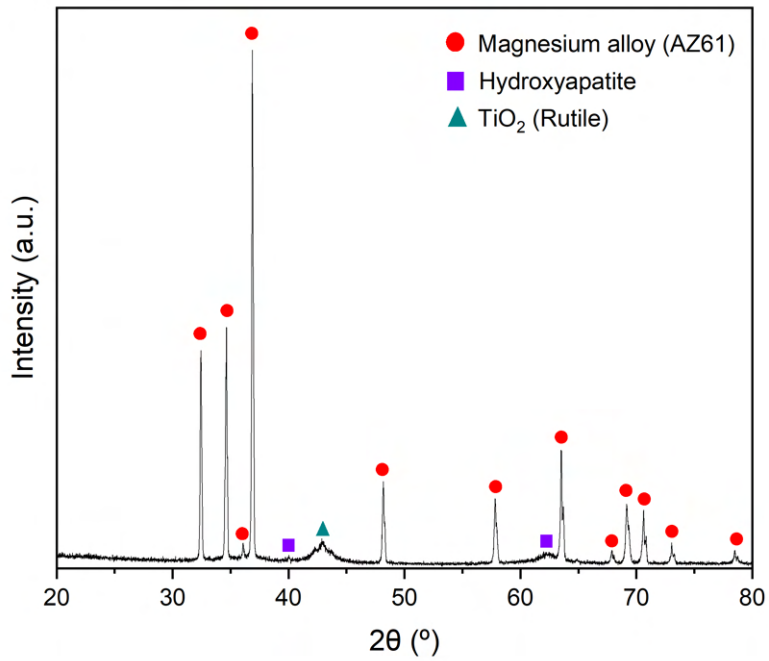

Figure A.33: XRD Analysis of HA-TiO_2-coated Mg alloy AZ61 (1.5 V for 60 minutes).

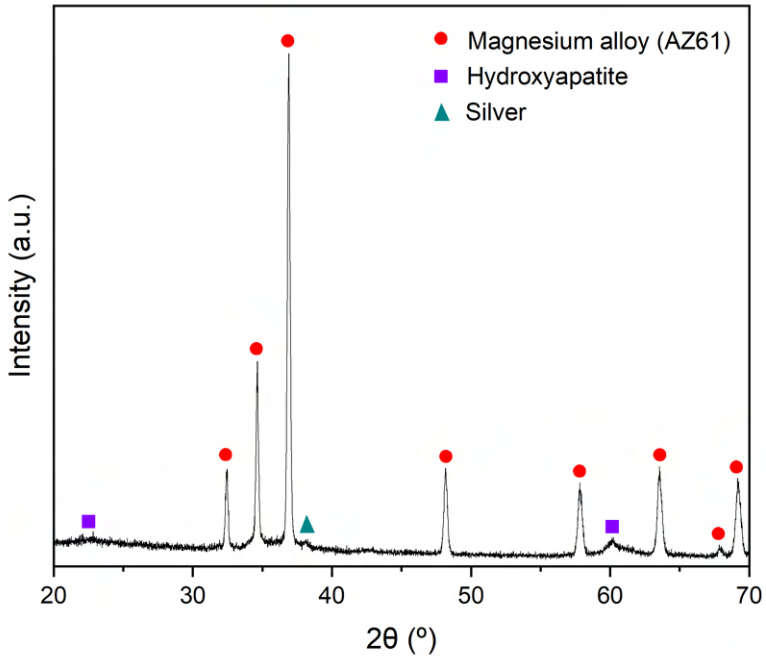

Figure A.34: XRD Analysis of HA-Ag-coated Mg alloy AZ61 (Low-concentration electrolyte for 6 minutes).

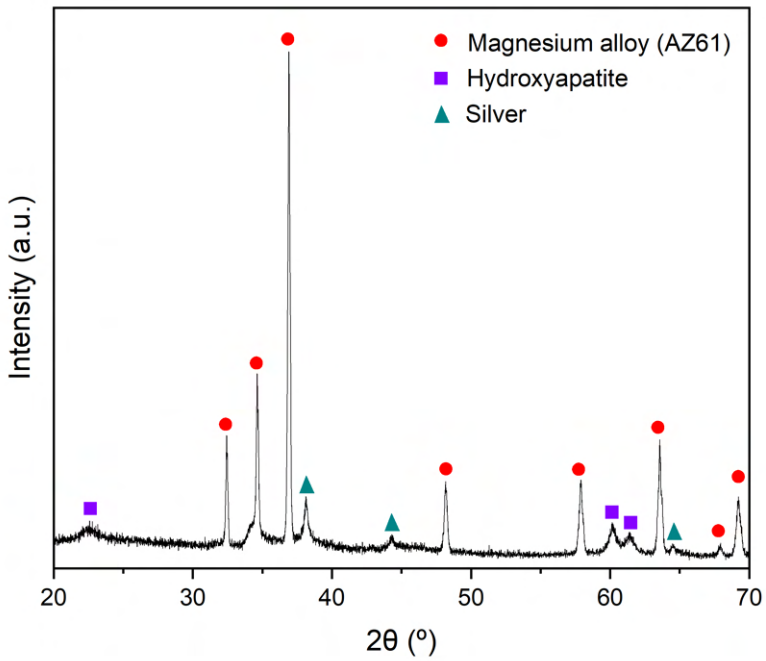

Figure A.35: XRD Analysis of HA-Ag-coated Mg alloy AZ61 (Low-concentration electrolyte for 30 minutes).

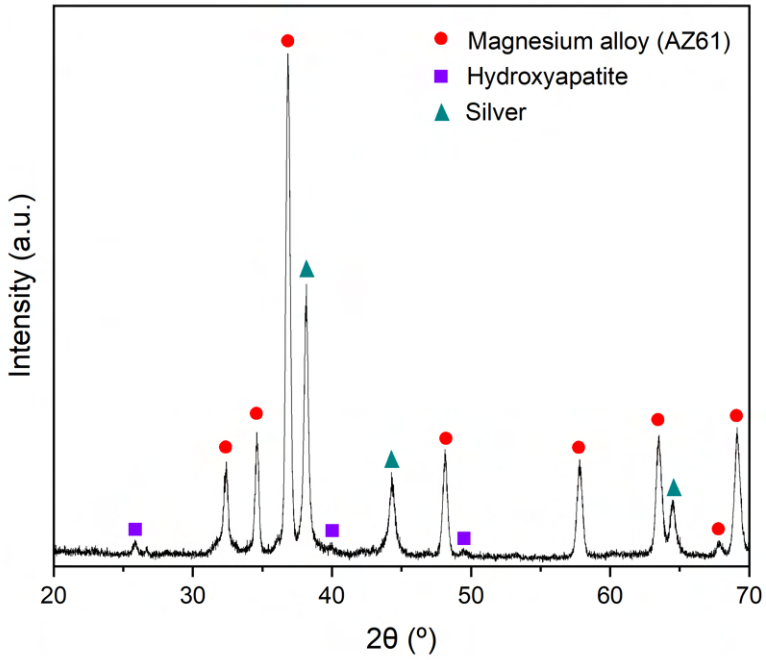

Figure A.36: XRD Analysis of HA-Ag-coated Mg alloy AZ61 (Low-concentration electrolyte for 45 minutes).

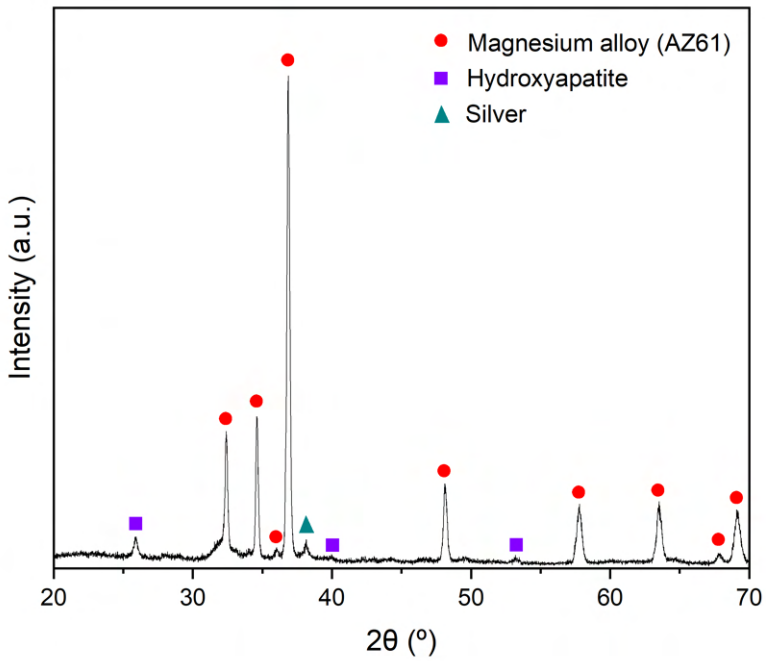

Figure A.37: XRD Analysis of HA-Ag-coated Mg alloy AZ61 (High-concentration electrolyte for 6 minutes).

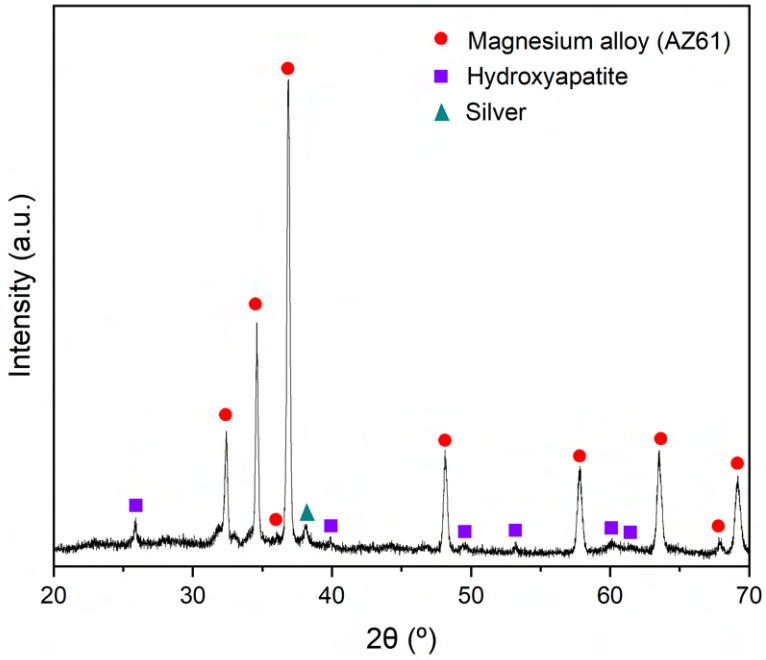

Figure A.38: XRD Analysis of HA-Ag-coated Mg alloy AZ61 (High-concentration electrolyte for 20 minutes).

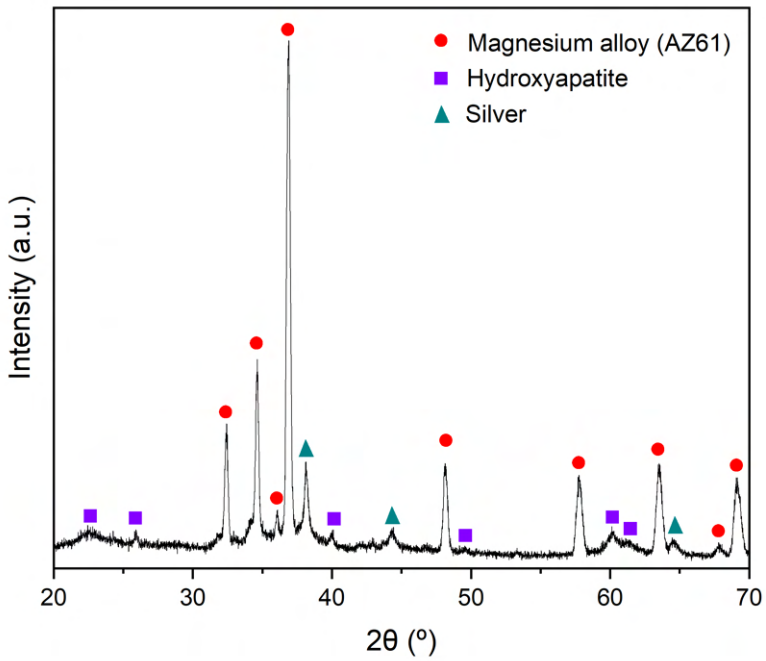

Figure A.39: XRD Analysis of HA-Ag-coated Mg alloy AZ61 (High-concentration electrolyte for 45 minutes).

A.2.4 Electrochemical Tests

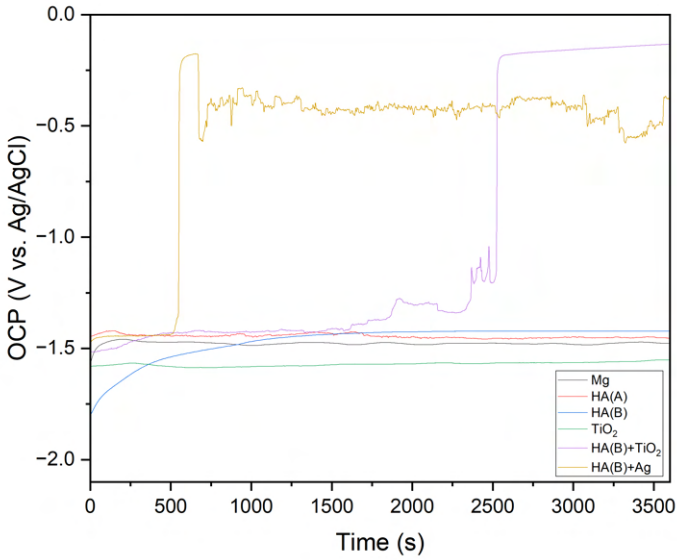

Figure A.40: OCP (PBS pH 7.4) of: Uncoated (Black); HA-coated - Protocol A (Red) and Protocol B (Blue); TiO_2-coated (Green); HA-TiO_2-coated (Purple); HA-Ag-coated (Yellow) Mg alloy AZ61.

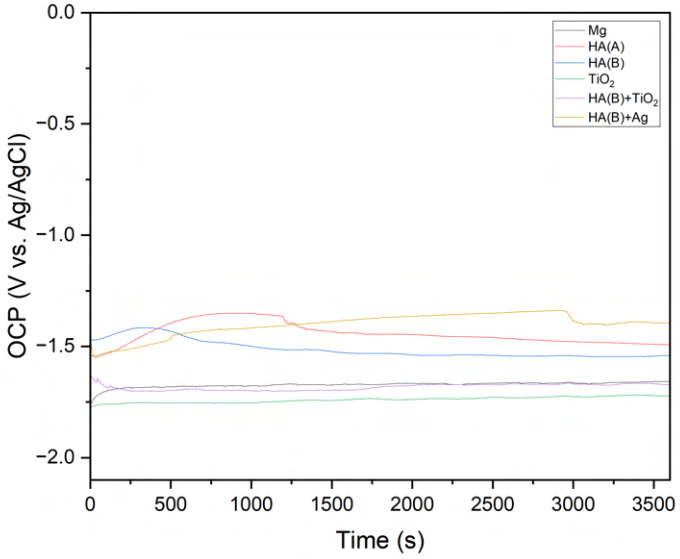

Figure A.41: OCP (PBS pH 5.5) of: Uncoated (Black); HA-coated - Protocol A (Red) and Protocol B (Blue); TiO_2-coated (Green); HA-TiO_2-coated (Purple); HA-Ag-coated (Yellow) Mg alloy AZ61.

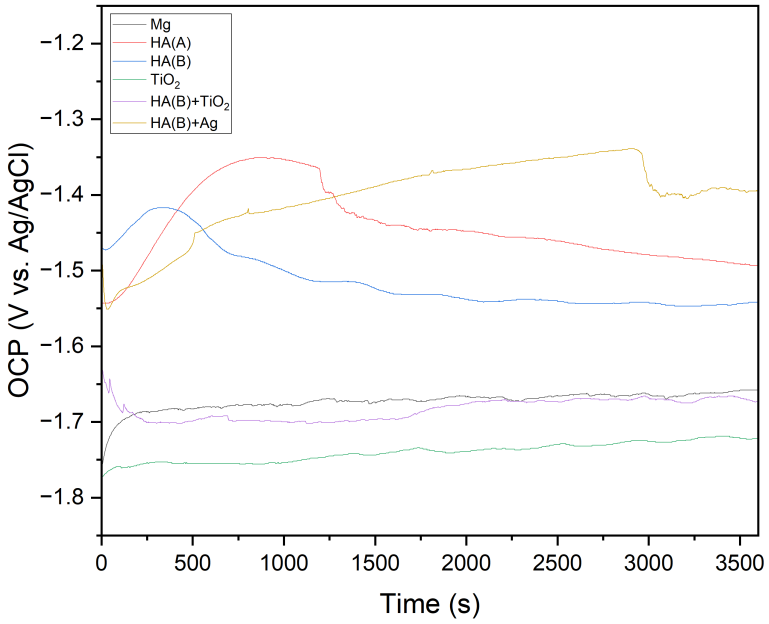

Figure A.42: OCP (PBS pH 5.5) of: Uncoated (Black); HA-coated - Protocol A (Red) and Protocol B (Blue); TiO_2-coated (Green); HA-TiO_2-coated (Purple); HA-Ag-coated (Yellow) Mg alloy AZ61.

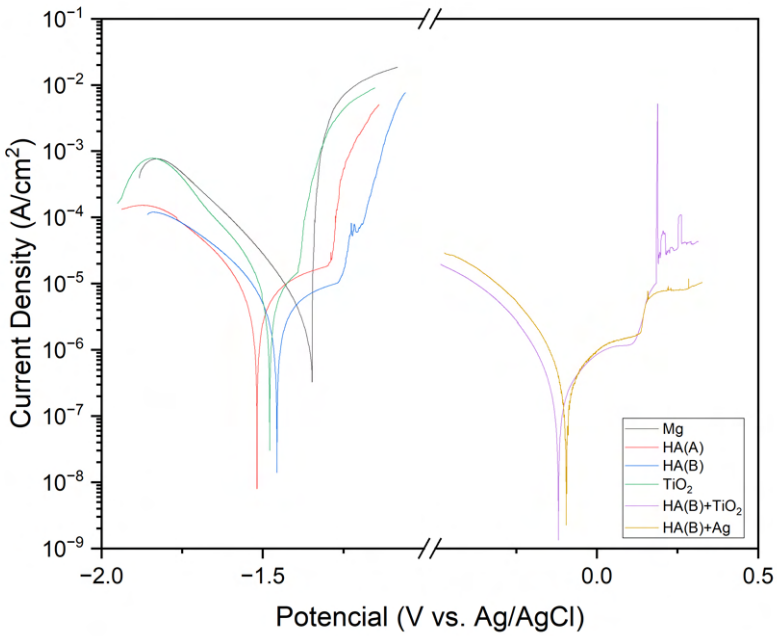

Figure A.43: Polarisation curves (PBS pH 7.4) of: Uncoated (Black); HA-coated - Protocol A (Red) and Protocol B (Blue); TiO_2-coated (Green); HA-TiO_2-coated (Purple); HA-Ag-coated (Yellow) Mg alloy AZ61.

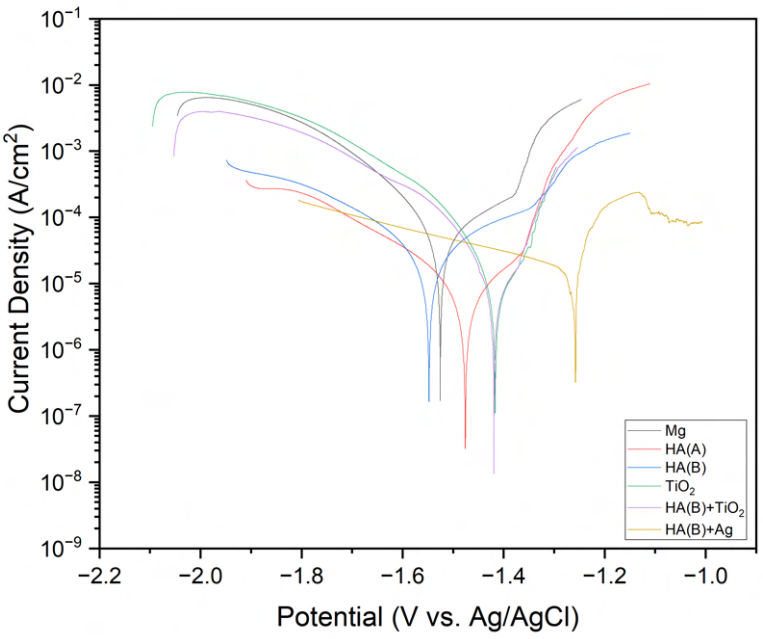

Figure A.44: Polarisation curves (PBS pH 5.5) of: Uncoated (Black); HA-coated - Protocol A (Red) and Protocol B (Blue); TiO_2-coated (Green); HA-TiO_2-coated (Purple); HA-Ag-coated (Yellow) Mg alloy AZ61.

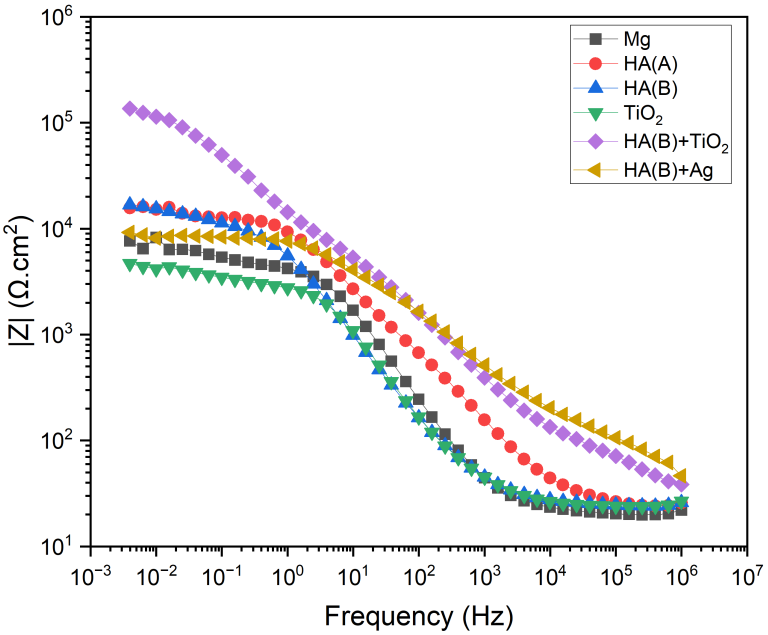

Figure A.45: Bode (Impedance) plot (PBS pH 7.4) of: Uncoated (Black); HA-coated - Protocol A (Red) and Protocol B (Blue); TiO_2-coated (Green); HA-TiO_2-coated (Purple); HA-Ag-coated (Yellow) Mg alloy AZ61.

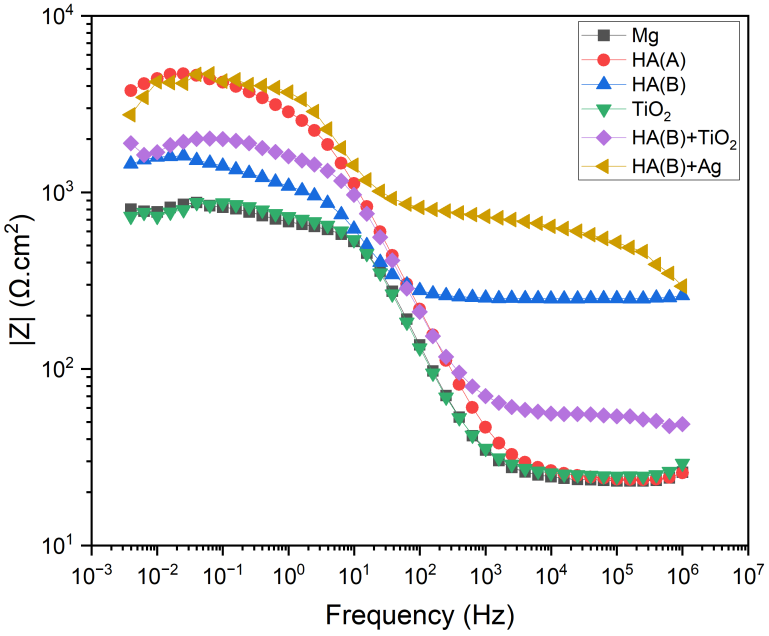

Figure A.46: Bode (Impedance) plot (PBS pH 5.5) of: Uncoated (Black); HA-coated - Protocol A (Red) and Protocol B (Blue); TiO_2-coated (Green); HA-TiO_2-coated (Purple); HA-Ag-coated (Yellow) Mg alloy AZ61.

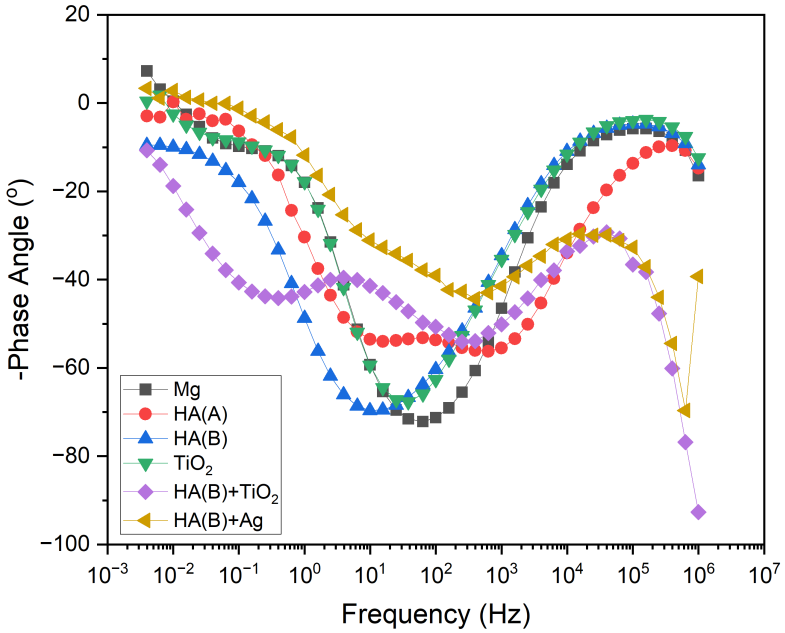

Figure A.47: Bode (Angle) plot (PBS pH 7.4) of: Uncoated (Black); HA-coated - Protocol A (Red) and Protocol B (Blue); TiO_2-coated (Green); HA-TiO_2-coated (Purple); HA-Ag-coated (Yellow) Mg alloy AZ61.

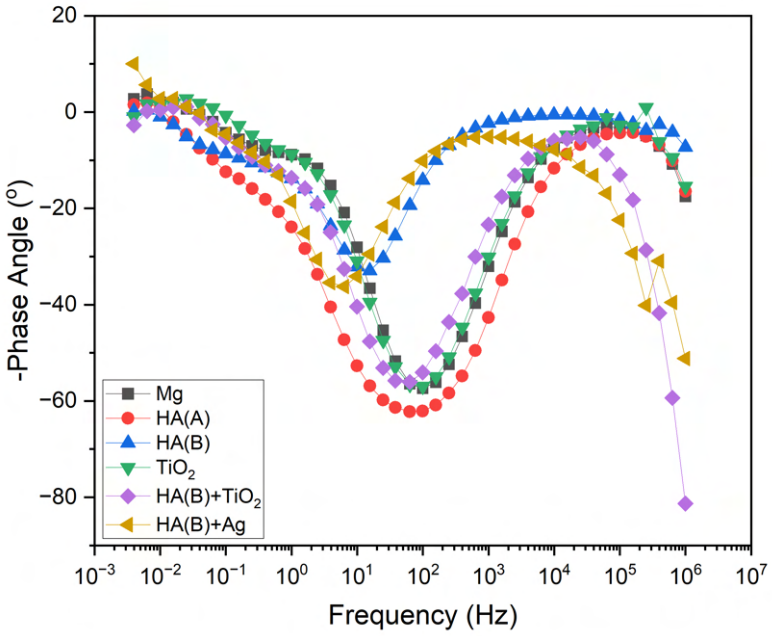

Figure A.48: Bode (Angle) plot (PBS pH 5.5) of: Uncoated (Black); HA-coated - Protocol A (Red) and Protocol B (Blue); TiO_2-coated (Green); HA-TiO_2-coated (Purple); HA-Ag-coated (Yellow) Mg alloy AZ61.

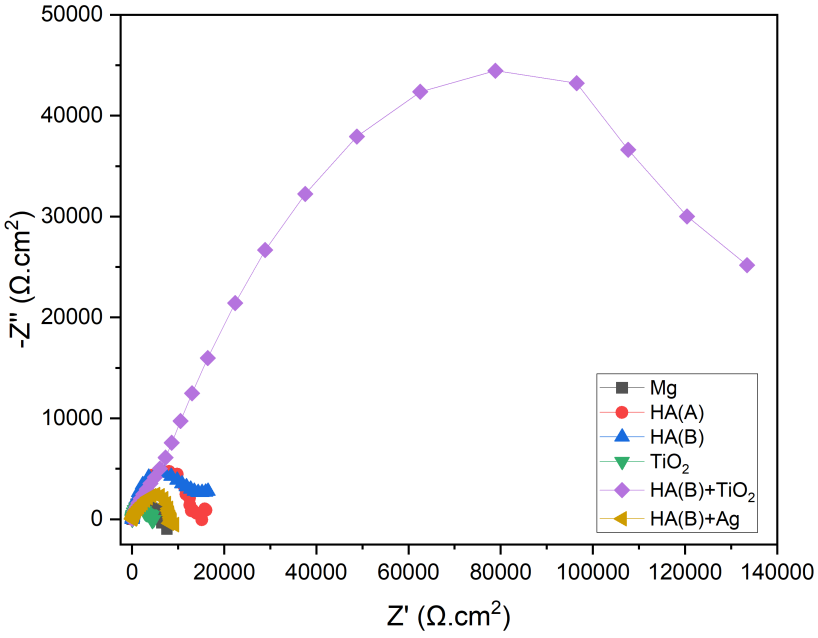

Figure A.49: Nyquist plot (PBS pH 7.4) of: Uncoated (Black); HA-coated - Protocol A (Red) and Protocol B (Blue); TiO_2-coated (Green); HA-TiO_2-coated (Purple); HA-Ag-coated (Yellow) Mg alloy AZ61.

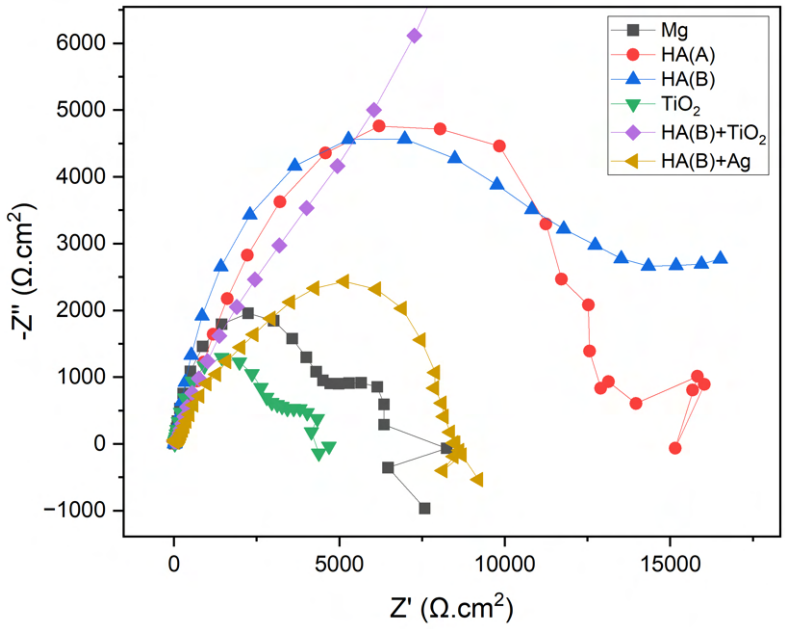

Figure A.50: Nyquist plot (PBS pH 7.4) of: Uncoated (Black); HA-coated - Protocol A (Red) and Protocol B (Blue); TiO_2-coated (Green); HA-TiO_2-coated (Purple); HA-Ag-coated (Yellow) Mg alloy AZ61. Zoomed view.

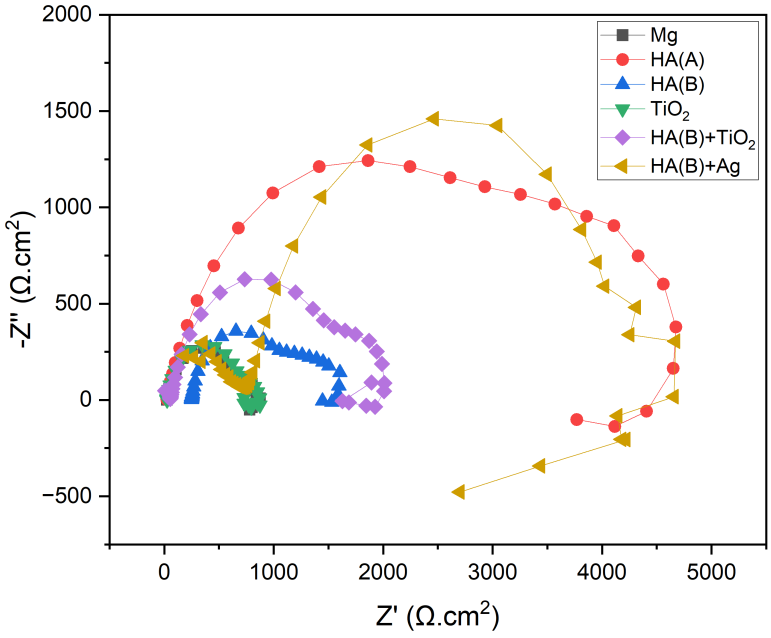

Figure A.51: Nyquist plot (PBS pH 5.5) of: Uncoated (Black); HA-coated - Protocol A (Red) and Protocol B (Blue); TiO_2-coated (Green); HA-TiO_2-coated (Purple); HA-Ag-coated (Yellow) Mg alloy AZ61.

A.2.5 Degradation Tests

Table A.1: Mass Loss and Corrosion Rate for the eighteen different samples after 63 days of immersion

Sample	Mass Loss (g)	Corrosion Rate (mm/y)
HA-Ag-coated - pH 7.4	0.0054	0.2351
HA-Ag-coated - pH 7.4	0.0102	0.4492
HA-Ag-coated - pH 7.4	0.0153	0.6385
HA-Ag-coated - pH 5.5	0.0069	0.3166
HA-Ag-coated - pH 5.5	0.0129	0.6035
HA-Ag-coated - pH 5.5	0.0250	1.1113
HA-coated - pH 7.4	0.0016	0.0789
HA-coated - pH 7.4	0.0009	0.0405
HA-coated - pH 7.4	0.0014	0.0678
HA-coated - pH 5.5	0.0012	0.0586
HA-coated - pH 5.5	0.0012	0.0546
HA-coated - pH 5.5	0.0023	0.1032
Uncoated - pH 7.4	-0.0026	-0.1233
Uncoated - pH 7.4	-0.0007	-0.0314
Uncoated - pH 7.4	-0.0007	-0.0304
Uncoated - pH 5.5	0.0050	0.2453
Uncoated - pH 5.5	0.0043	0.1692
Uncoated - pH 5.5	0.0440	1.7356

Table A.2: Elemental composition of one representative sample from each group after 63 days of immersion (in %)

Sample	O	Mg	C	P	Al	Ca	Na	Si	Ag	K
Uncoated pH 7.4	70.54	15.99	8.29	4.93	-	-	-	-	-	-
Uncoated pH 5.5	68.65	20.74	7.26	1.42	1.85	-	-	-	-	-
HA-coated pH 7.4	70.71	6.08	-	9.26	-	9.74	2.51	-	-	-
HA-coated pH 5.5	73.56	11.80	-	6.07	-	6.84	1.07	-	-	-
HA-Ag-coated pH 7.4	71.93	13.34	-	3.59	2.45	4.62	-	3.00	0.32	-
HA-Ag-coated pH 5.5	69.09	12.48	-	6.72	-	-	4.82	-	0.07	3.17

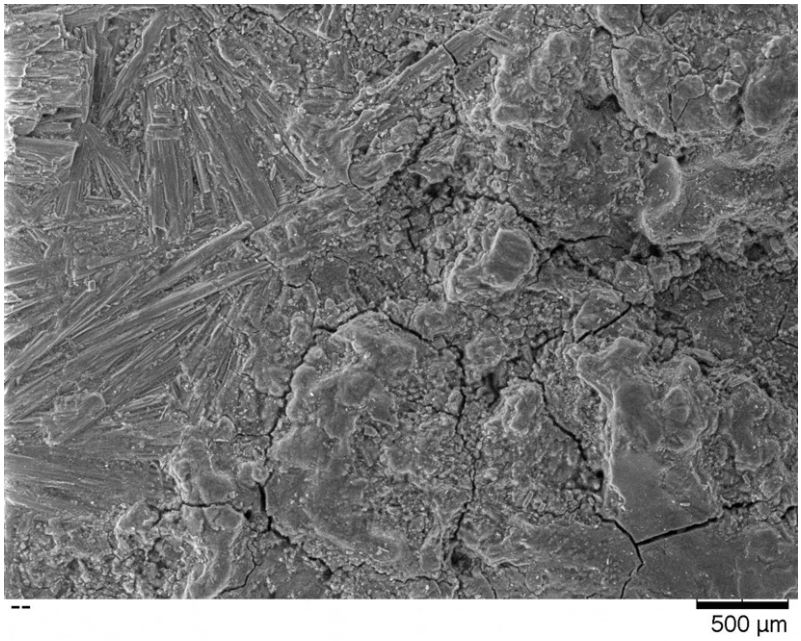

Figure A.52: SEM of Uncoated Mg alloy AZ61 after 63 days of immersion in PBS at pH 7.4.

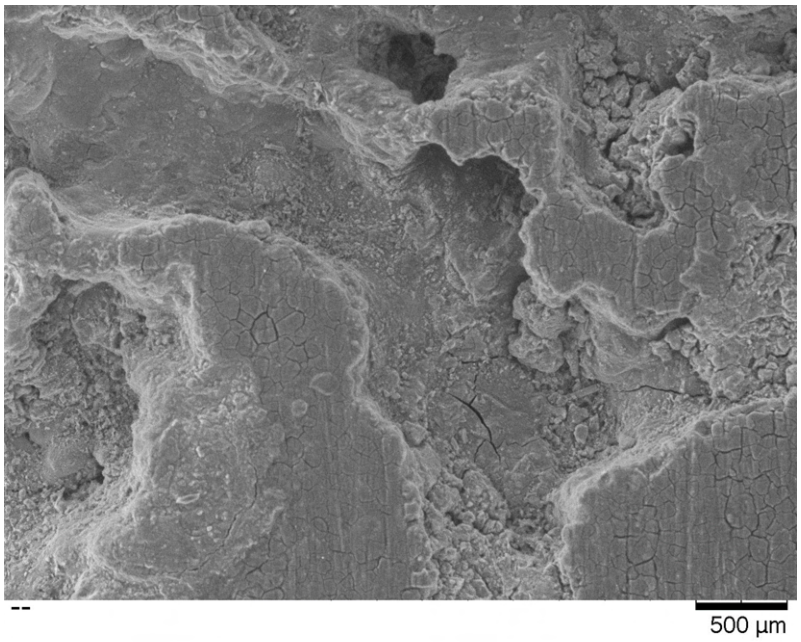

Figure A.53: SEM of Uncoated Mg alloy AZ61 after 63 days of immersion in PBS at pH 5.5.

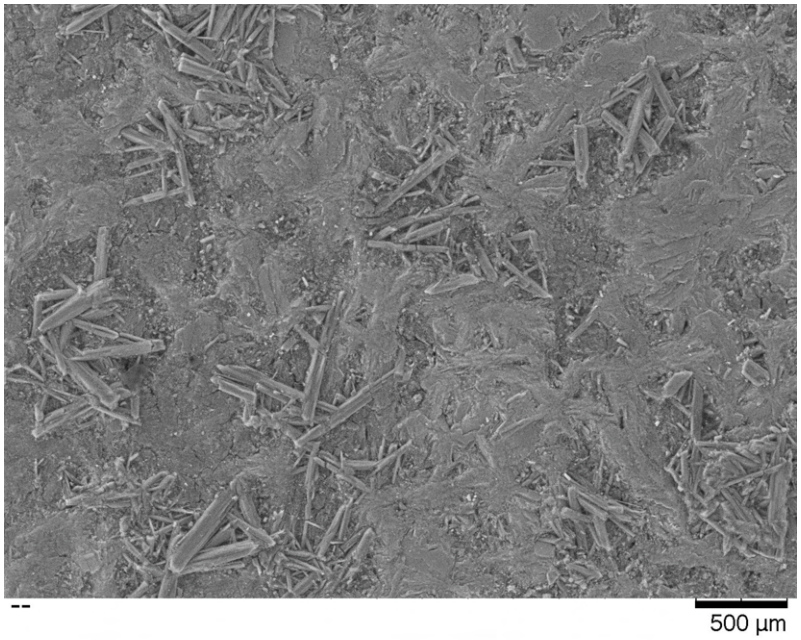

Figure A.54: SEM of HA-coated Mg alloy AZ61 after 63 days of immersion in PBS at pH 7.4.

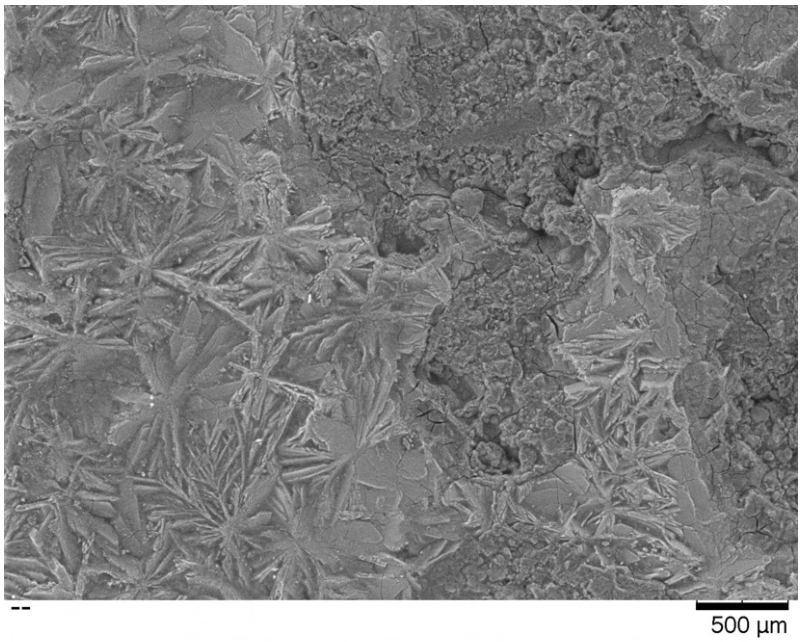

Figure A.55: SEM of HA-coated Mg alloy AZ61 after 63 days of immersion in PBS at pH 5.5.

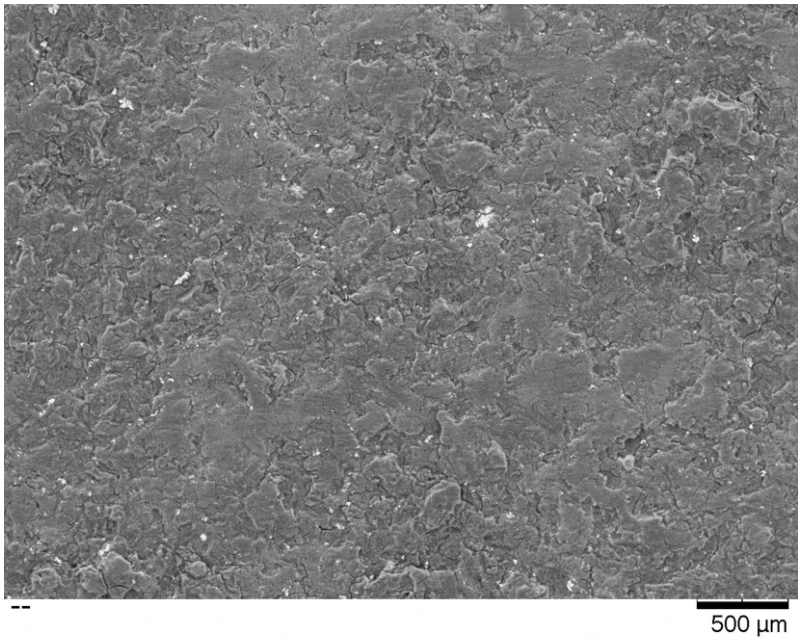

Figure A.56: SEM of HA-Ag-coated Mg alloy AZ61 after 63 days of immersion in PBS at pH 7.4.

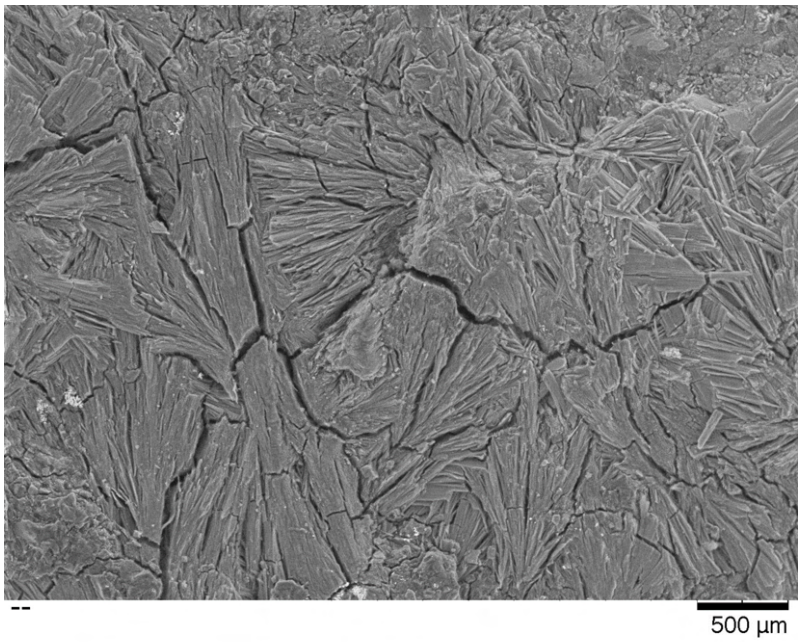

Figure A.57: SEM of HA-Ag-coated Mg alloy AZ61 after 63 days of immersion in PBS at pH 5.5.

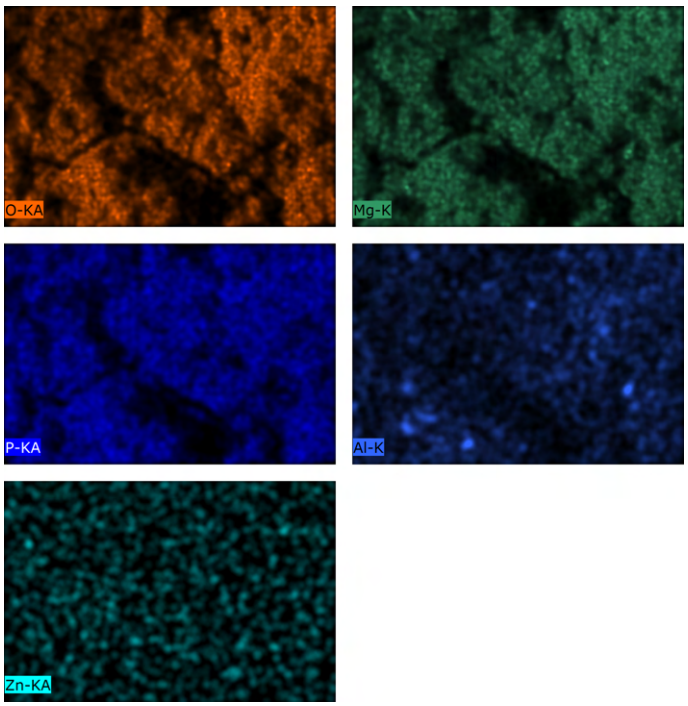

Figure A.58: EDS map of Uncoated Mg alloy AZ61 after 63 days of immersion in PBS at pH 7.4.

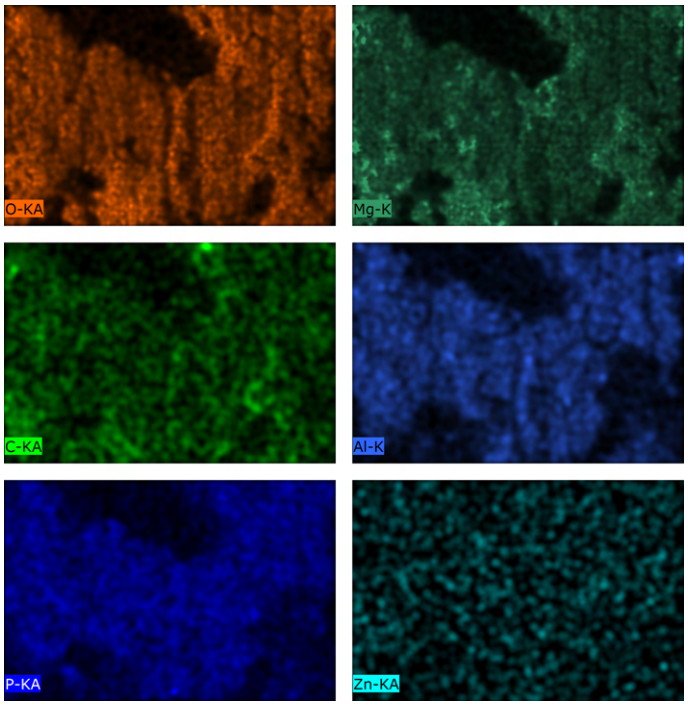

Figure A.59: EDS map of Uncoated Mg alloy AZ61 after 63 days of immersion in PBS at pH 5.5.

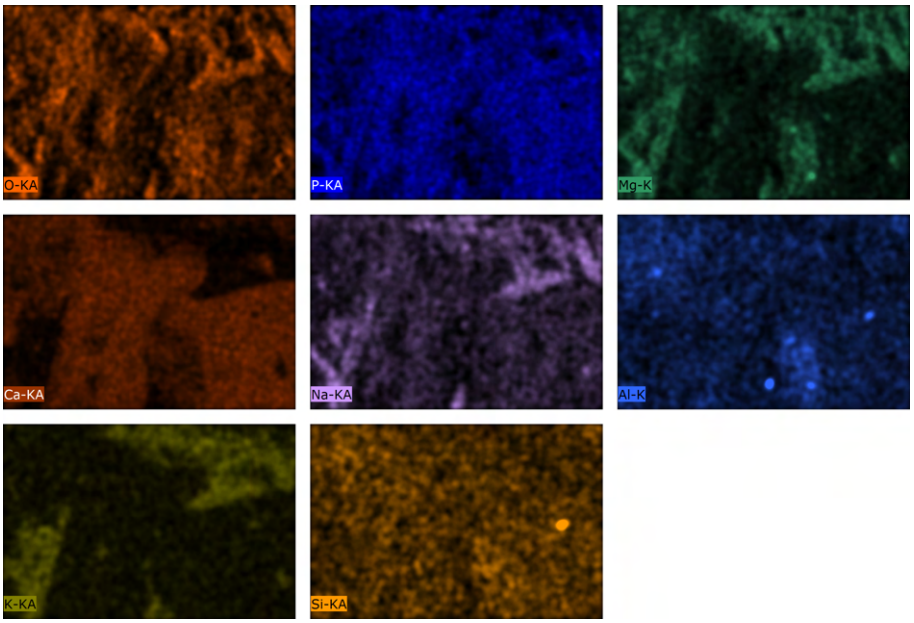

Figure A.60: EDS map of HA-coated Mg alloy AZ61 after 63 days of immersion in PBS at pH 7.4.

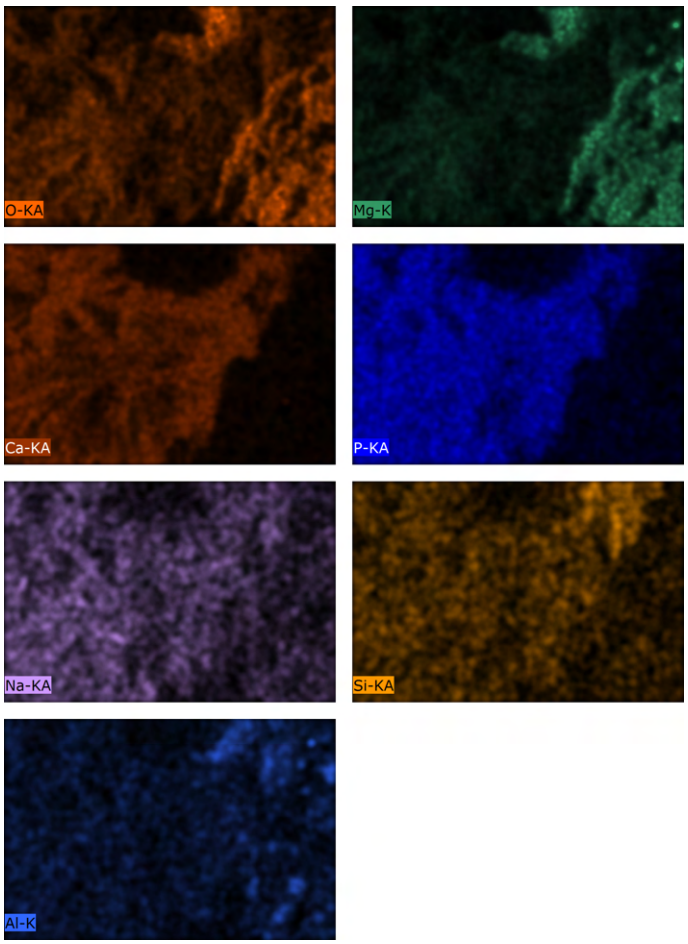

Figure A.61: EDS map of HA-coated Mg alloy AZ61 after 63 days of immersion in PBS at pH 5.5.

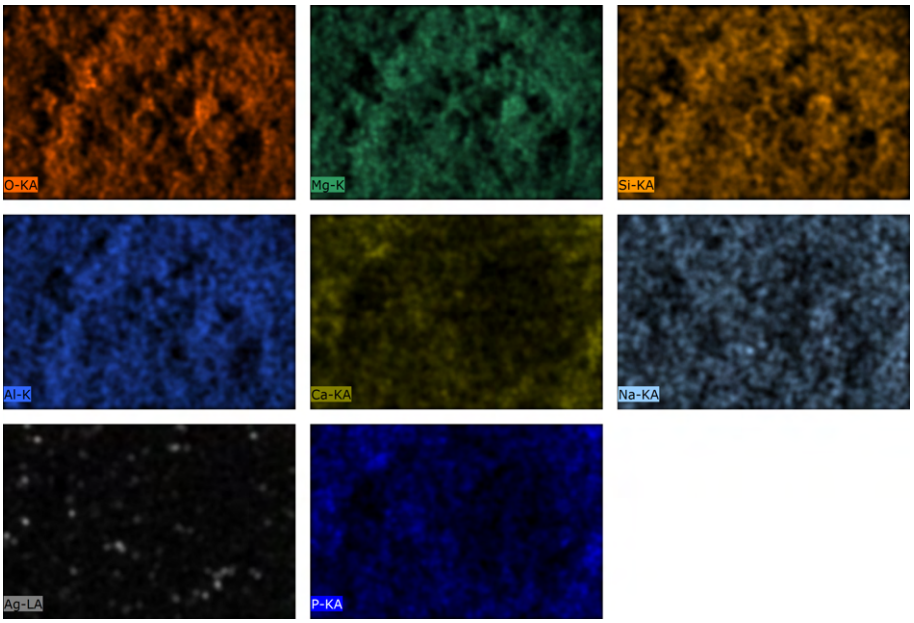

Figure A.62: EDS map of HA-Ag-coated Mg alloy AZ61 after 63 days of immersion in PBS at pH 7.4.

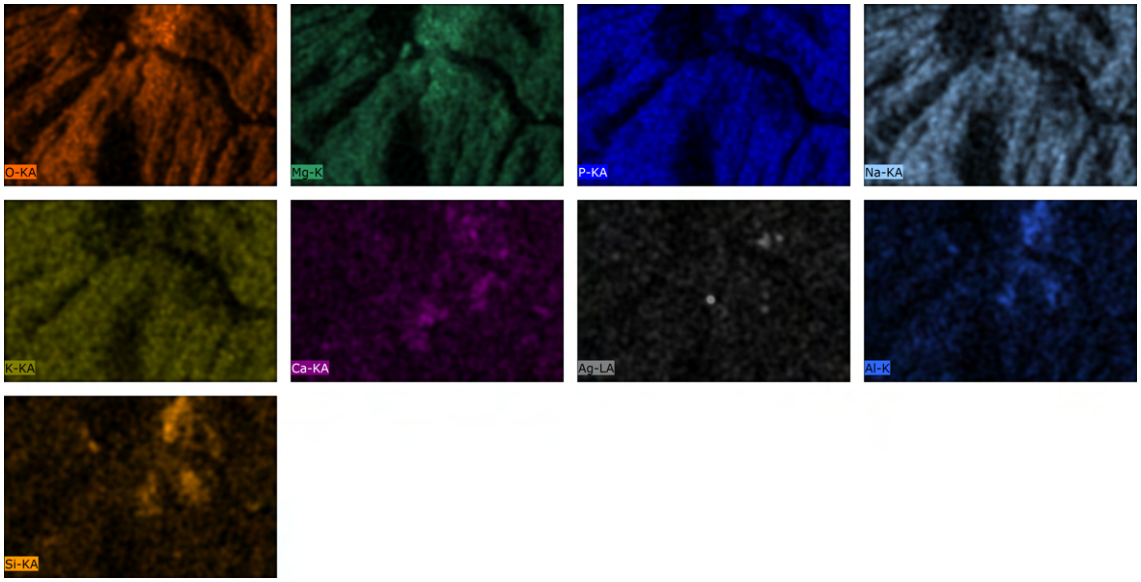

Figure A.63: EDS map of HA-Ag-coated Mg alloy AZ61 after 63 days of immersion in PBS at pH 5.5.

A.2.6 Cytotoxicity Tests

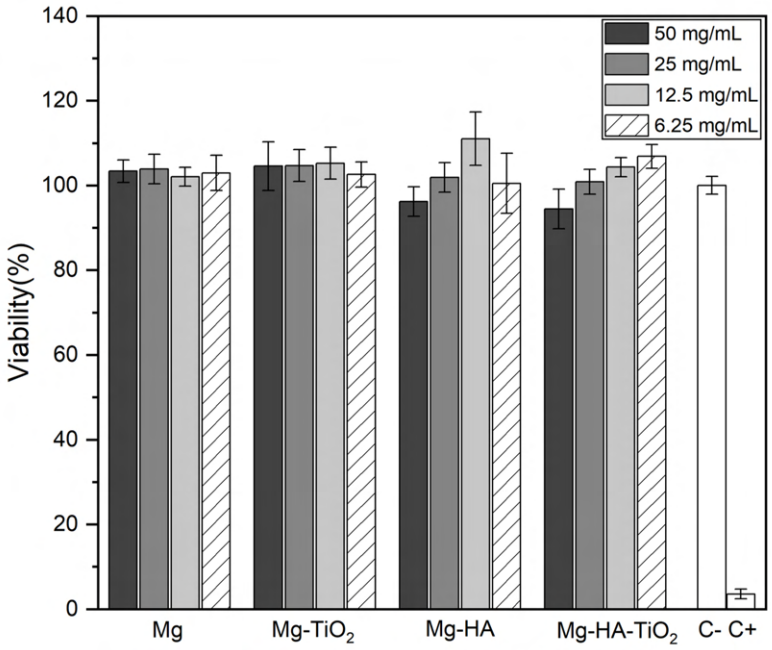

Figure A.64: Cell viability of Mg alloy AZ61 samples: Uncoated, HA(B), TiO_2, and HA-TiO_2-coated samples after 24 hours.

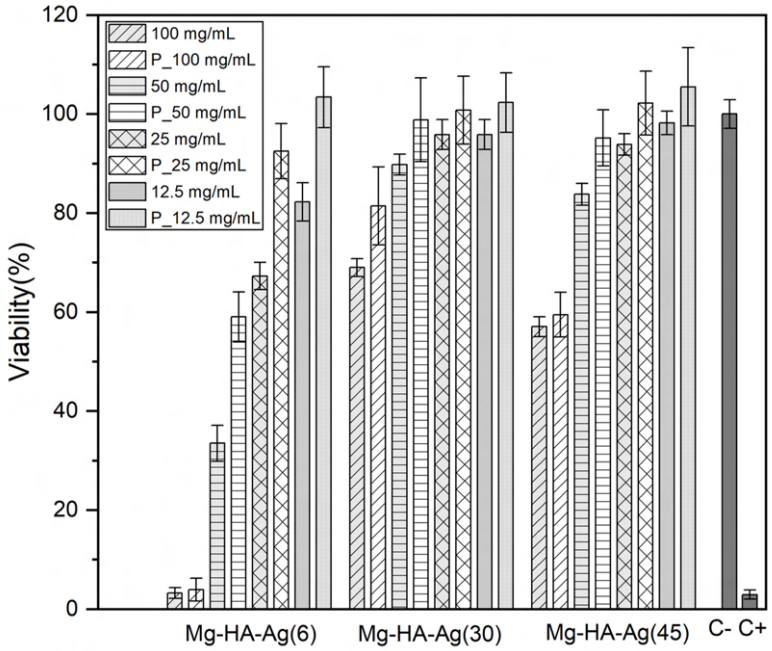

Figure A.65: Cell viability of Mg alloy AZ61 samples: HA-Ag-coated samples (coated for 6, 30, and 45 minutes) after 24 and 48 hours.